Conceptual Framework and Physical Implementation of a Systematic Design Strategy for Tissue-Engineered Devices

Thesis by

Janna C. Nawroth

In Partial Fulfillment of the Requirements

for the Degree of

Doctor of Philosophy

California Institute of Technology

Pasadena, California

2013

(Defended December 4, 2012)

© 2013

Janna C. Nawroth

All Rights Reserved

Acknowledgments

Foremost, I would like to thank my family and friends who have provided support and encouragement during good and bad times. I am particularly grateful to my mother who, along with my aunts and other close relatives, has laid the foundation for my passion for science and the confidence to persue an academic career. My dear friend and colleague Kamila Naxerova deserves particular gratefulness for her effective mix of endless patience and tough love that has carried me through more than one icy Boston winter full of frustration and failed experiments.

My advisor Professor John Dabiri has offered me his continuous support and advice. His creativity, focus, and enthusiasm have been a great source of inspiration and encouragement. Through his example and guidance I have developed the confidence and humility needed to form a broader perspective on science that goes beyond the boundaries of classical disciplines and yet remain focused on concrete projects and tangible progress.

I also would like to express my gratitude to my other mentors on this project, Professors Kevin Kit Parker, Bruce Hay, Paul Sternberg, Scott Fraser, Mory Gharib, and Michael Dickinson.

I am especially thankful for the multitude of advisors, colleagues, friends, and collaborators that have helped to enhance my scientific education, research, and quality of life, including Drs.Gordon Shepherd, James Mazer, David Willhite, Sally Kim, Kiersten Darrow, Eva Kanso, Rainer Friedrich, Kelly Sutherland, Matthias Kinzell, Megan McCain, Adam Feinberg, Patrick Alford, Crystal Ripplinger, Kakani K.Young; Mmes.Abigail

Green, Esperanza Linares, and Yun Elisabeth Wang; Messrs.Josua Goss, Robert Whittlesey, Steve Spina; and the New England Aquarium in Boston, MA, and the Cabrillo Aquarium in San Pedro, CA.

Abstract

Tissue-engineered and biologically inspired devices promise to advance medical implants, robotic devices and diagnostic tools. Ideally, biohybrid constructs combine the versatility and fine control of traditional building substrates with dynamic properties of living tissues including sensory modalities and mechanisms of repair, plasticity and self-organization. These dynamic properties also complicate the design process as they arise from, and act upon, structure-function relationships across multiple spatiotemporal scales that need to be recapitulated in the engineered tissue. Biomimetic designs merely copying the structure of native organs and organisms, however, are likely to reflect evolutionary constraints, phenotypic variability and environmental factors rather than rendering optimal engineering solutions.

This thesis describes an alternative to biomimetic design, i.e., a systematic approach to tissue engineering based on mechanistic analysis and a focus on functional, not structural, approximation of native and engineered system. As proof of concept, the design, fabrication and evaluation of a tissue-engineered jellyfish medusa with biomimetic propulsion and feeding currents is presented with an emphasis on reasoning and strategy of the iterative design process. A range of experimental and modeling approaches accomplishes mechanistic analysis at multiple scales, control of individual and emergent cell behavior, and quantitative testing of functional performance. The main achievement of this thesis lies in presenting both conceptual framework and physical implementation of a systematic design strategy for muscular pumps and other bioinspired and tissue-engineered applications.

Contents

List of Figures

Chapter 1

Prologue

Why are organisms built the way they are? Historically, explanations of biological design have ranged from geometric mysticism asserting a convergence of living and inanimate matter alike toward mathematically "perfect" proportions, such as the Golden Section,[1] to the equally simplified presumption that limbs and tissues were optimized for a specific function. The contemporary perspective, shaped by insights from genetics, a growing fossil record and biomechanics, is more cautious in assigning structural or functional optimality to biological design.[2]Rather, the challenge is to untangle evolutionary constraints from functional meaning: Structures seemingly wasteful or unfavorable for the intended use, such as many human skeletal features derived from four-legged ancestors (Olshansky et al. 2001) might harbor benefits and safety factors only revealed during specific behaviors. For example, apparent material weaknesses in the mineralized clubs of predatory mantis shrimps actually constitute predetermined breaking points absorbing the shock of high velocity killing strikes (Weaver et al. 2012). Further, specific functional dedication cannot be premised as many systems serve multiple purposes, such as vertebrate skin that regulates body heat, imparts sensation, shields from mechanical impacts and provides camouflage, among others.

Given these complications, how can biological design be studied, what can be learned

[1]For an excellent review of order and shape formation in the living world, both real and imagined, turn to "Nature's patterns, a tapestry in three parts" by Phillip Ball (Ball 2001).

[2]A thorough debate on design optimization is provided by "Principles of Animal Design," a collection of essays discussing morphological, evolutionary and physiological perspectives (Weibel et al. 1998).

from it, and why would it be of benefit? Several approaches have been developed to tease out design principles and their functional relevance. Comparative biology helps reveal convergence of design, that is, the evolution of common features in unrelated species in response to common functional needs, indicating the presence of unifying design constraints. The branching patterns of circulatory systems in various animals and plants, for example, are shaped according to universal laws minimizing the cost of flow and material usage (LaBarbera 1990; Murray 1926). Other approaches include studying the impact of selective environmental variables on performance or inheritance of design features, or, conversely, the effect of manipulating an organism's design on functional performance and survival. These studies link biological structures to their use, and they indicate how specific design solutions reflect material constraints and functional compromises. Both general principles and specific solutions are of interest to biologically inspired and medical engineering disciplines; to the former they provide a source of prototypes and alternative designs for synthetic applications, to the latter they manifest the mechanisms linking cell behavior, tissue organization and emergent functions. In particular, tissue-engineering would benefit from systematic, rather than mimetic, design strategies that not only harness but take *advantage* of the particularities of living matter to generate multifunctional, resilient and adaptive tissues and extend the limitations of synthetic materials. Further, for biologists who study the connection between form and function, the major constraint is that only successful solutions have survived natural selection. Systematic engineering of biological tissues therefore provides a new tool to probe alternate and extinct evolutionary pathways, to determine the mechanisms that dictate natural structure-function relationships, and to design *de novo* structure-function relationships for engineering objectives (e.g., biomedicine and robotics).

To this end, this thesis presents an interdisciplinary approach to translating design principles from native to tissue-engineered systems, be it soft robots, organ replacements or experimental platforms. The manuscript opens with a thorough discussion of chal-

lenges and concepts of using living cells as building substrates, preparing the ground for the focus of this thesis, a proof-of-concept study in systematic tissue design.

The manuscript is composed on the basis of two peer-reviewed research and one review article in journals of experimental biology and biotechnology, all written by the thesis author. Chapter 2 discusses the challenges and benefits of developing design standards for engineered tissues, using as a specific example the proof-of-concept study summarized in chapter 3, i.e., the process of designing, building and testing a tissue-engineered jellyfish, aka 'medusoid', with biomimetic swimming and feeding function. Chapters 4 to 8 discuss the details of identifying, implementing and testing the design principles underlying swimming in native and engineered jellyfish. Chapter 4 addresses actuation and force generation in the neuromuscular system, chapter 5 covers stroke kinematic, chapters 6 and 7 identify design principles relevant for fluid dynamics, and chapter 8 closes with the analysis of functional benchmarks of native and engineered jellyfish. In summary, using the jellyfish medusa as a model system, this thesis discusses strategies and methods for the investigation and implementation of biological design principles for advancing biologically inspired and tissue-engineered applications.

Chapter 2

Design Standards for Engineered Tissues

This chapter was submitted to *Biotechnology Advances* on October 18, 2012 and is scheduled for publication in early 2013. It is reproduced as is except for minor changes to references, formatting and data presentation.

2.1 Authors

Janna C Nawroth[1] and Kevin Kit Parker[2]

2.2 Author Contributions

J. C. N. prepared the manuscript. K. K. P. advised and made final edits.

2.3 Introduction

Engineered technologies such as aircraft, bridges, and microelectronic devices are all designed and manufactured to meet specific, quantitative standards of safety and performance. These more traditional engineering projects are based on a fundamental

[1]Division of Biology, California Institute of Technology, Pasadena, California, USA
[2]Disease Biophysics Group, Wyss Institute for Biologically Inspired Engineering and School of Engineering and Applied Sciences, Harvard University, Cambridge, Massachusetts, USA

understanding of the building substrates, such as aluminum, steel, concrete, and gallium arsenide, which are then integrated into the design process. In tissue engineering, similar manufacturing standards have proven elusive, as the field to date has largely focused on feasibility experiments where the mass manufacturing of cells and tissues has not been required. However, as the field advances, the adoption of quality control procedures will be imperative to satisfy regulatory requirements and clinical use. Further, establishing a catalog of standard procedures and materials will facilitate the design of tissues and tissue-augmented devices. Formulating quality control and design standards will necessitate a materials characterization of the tissue's building substrates, the living cell and the extracellular matrix.

In the last two decades an increasing wealth of micro- and nanofabrication tools has become available for creating and customizing cell culture substrates that provide mechanical support and instruct cell differentiation and survival (Dvir et al. 2011; Gauvin et al. 2012; Hollister 2005; Kane et al. 1999; Langer and Vacanti 1993; Lutolf and Hubbell 2005). Such tools have allowed investigators to mimic cellular environments and test how the cells will respond under various conditions, not unlike the material characterization that precedes any engineering project. These technologies suggest that local control of cell behavior can be exploited to transform cells into predictable building substrates with quantitatively defined performance standards. While local control of cellular form and function is not a trivial pursuit, scaling from microenvironments to 3D-tissue, however, remains even more challenging in the view of multiscale architecture, mechanics and communication (chemical, electrical, and mechanical) that regulate, in the aggregate, global function. Take, for example, the ongoing quest of tissue-engineering functional heart valve replacements despite of more than 50 years of research and a comprehensive understanding of valve mechanics and morphology (Dasi et al. 2009; Sacks and Yoganathan 2007). Unlike mechanical and electrical engineering disciplines where components can be isolated and expected to exhibit characteristic material properties

independent of context, tissue engineering must account for particularities of a living substrate and its unique behavior within a population. This includes context-dependent gene expression and so-called emergent properties, i.e., novel characteristic exhibited at population level that cannot be easily predicted from individual components, such as self-organization and synergetic effects (Corning 2002). A purely biomimetic design strategy, i.e., blind copying of the entire system may not be possible without a fundamental law of cellular behavior and appropriate scaling laws that cover abroad range of spatial and temporal scales (Parker and Ingber 2007). The classical engineering approach provides an alternative approach that was adopted most recently to develop design standards in molecular synthetic biology (Andrianantoandro et al. 2006): Decouple the system, i.e., break down global function into smaller structural and functional entities that can be analyzed separately; use abstraction, i.e., organize the system into hierarchies that facilitate analysis and can be combined in novel ways; and implement quality control, i.e., develop definitions of standard biological components and systems.

Quality control is faced with the inherent variability of individual cell behavior due to gene expression noise and context dependence. Further, cell-to-cell and extracellular matrix interactions modulate the impact of individual cellular components within the tissue. Thus, rather than requiring identical cellular building blocks, functional test criteria should be based on statistics of cell populations, the level at which function is generated. The unreliability of individual cell function can be taken into account by establishing ranges of tolerances of population statistics permissive for adequate tissue performance. Particular opportunities and challenges are presented by the use of embryonic, adult, or induced stem cells for tissue-engineering. Controlled by a complex network of genetic and epigenetic pathways, these cells harbor the potential of both self-renewal and differentiation (Li et al. 2012), promising the advent of autologous implants for repair and restoration of impaired organ function (Jopling et al. 2011), but also bearing the risk of oncogenesis (Zhu et al. 2012). Induced pluripotent stem

cells (iPSCs), for example, have been shown to differ from embryonic stem cells in gene expression, epigenetic landscape, differentiation potential, and mutational load while the functional consequences remain unclear (Bilic and Izpisua Belmonte 2012; Yamanaka 2012). Therefore, safety criteria might have to be based on individual cell characteristics, highlighting the need for standardized procedures and quality control customized for each building material. In the following, we will discuss a framework of concepts leading towards general design standards for tissue-engineering.

In the following, I will discuss a framework of concepts leading toward design standards for engineered tissues. In order to illustrate the practical implementation of each concept, I will use as an example the process of creating a tissue-engineered jellyfish, which is summarized in chapter 3 and discussed in detail in subsequent chapter.

2.4 Engineering Algorithm: Design, Build, Test

A prerequisite to developing design standards is adopting the traditional engineering algorithm, which iterates analysis and design of key structure-function relationships, assembly of quality controlled prototypes, and performance testing using quantitative benchmarks (figure (2.1)). In a proof-of-concept study, we recently reported the reverse engineering of a *Aurelia aurita* jellyfish in the form of a biohybrid life form consisting of a synthetic polymer thin film and precisely engineered rat cardiac tissue a(Chapter 3; Nawroth et al. 2012). This model system was chosen because of the jellyfish's simple and easily accessible anatomy that, paired with well-defined propulsion and feeding functions (chapter 8; Dabiri et al. 2005), facilitated analysis, design, assembly and testing of structure-function relationships at multiple scales using quantitative metrics.

More precisely, the spatial orders of magnitudes spanned by the structural entities in native jellyfish that underlie swimming and feeding function range from nanoscale contractile fibers to macroscale flow patterns (figure 2.2, top half, yellow). Research

tools including computational modeling, imaging approaches and experimental manipulation revealed how structural entities combine and interact to form three key functional entities relevant for swimming and feeding: specific conformational change of bell shape controlled by lobed body geometry, muscle anisotropy and synchronized electrical pacing signal (figure 2.2, a), asymmetric stroke kinematics depending on fast muscle contraction and slow elastic recoil of the lappet substrate (figure 2.2, b), and geometry-dependent exploit of viscous boundary layers for diverting oncoming flow from gap spaces, thus facilitating efficient fluid displacement during contraction (figure 2.2, c). In order to recapitulate the key functional entities underlying jellyfish function, tools such as computational modeling, self-assembly, microfabrication, and quality control were used to design and build engineered structural entities across multiple spatial orders of magnitudes, including contractile fiber organization at micrometer scale, lappet geometry at millimeter scale, and flow patterns at centimeter scale (figure 2.2, bottom half, grey).

Linking structure to function represents the greatest challenge in this algorithm. Computational and empirical analysis revealed can help reveal weaknesses of the design and guide rational design optimization. In the jellyfish example, tissue and behavioral complexity were sufficiently modest to model straightforward structure-function relationships and constrain the design choices according to rational criteria. Creation of more complex systems, where functional entities and structure-function relationships are less well-defined, may benefit from complementary approaches such as an initial sensitivity analysis, which indicates important design parameters, and directed evolution, which screens random design variations according to functional selection criteria, such that working solutions "emerge" without necessitating initial full mechanistic insight (Esvelt et al. 2011; Andrianantoandro et al. 2006). Importantly, biomimetic function ensuing from any of these strategies does not necessitate biomimetic materials at all levels of organization; rather, we propose that functional convergence of dissimilar starting materials can be reached if key structure-function relationships are reproduced. For these

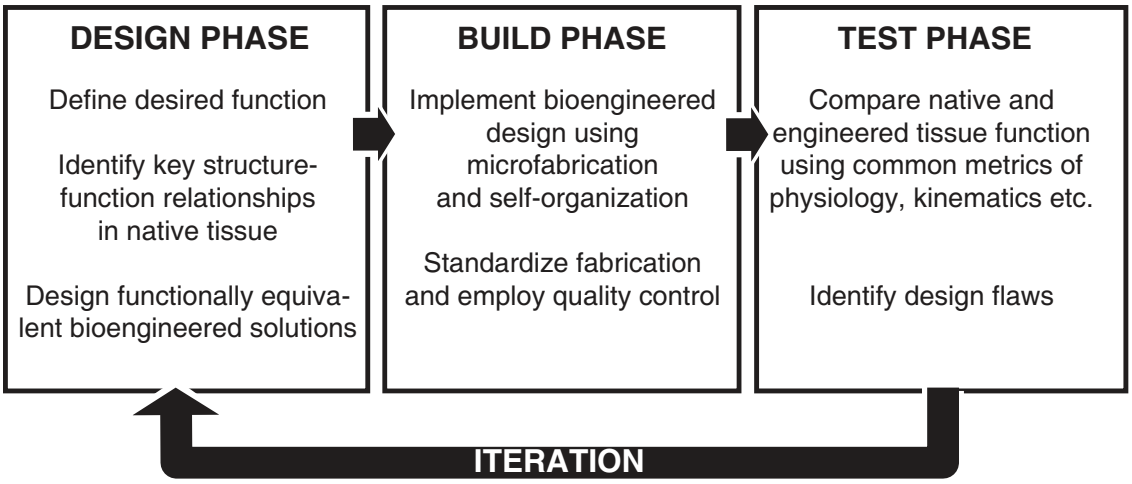

Figure 2.1. Engineering design algorithm for tissue-engineering functional constructs. The design algorithm consists of three phases: design, build and test. The series of steps is iterated until the engineered construct exhibits the desired functional performance. Design phase: Start by identifying quantitative benchmarks characterizing the desired function in a model system. Then, identify key design elements contributing to this function. Determine functionally equivalent bio-engineered solutions from the pool of available materials. Build phase: Proceed by fabricating the bioengineered solution and standardize fabrication for repeatability using quality control. Test phase: Quantify implementation of key design elements including structural, physiological, kinematic and fluid dynamics characteristics. Finally, compare functional performance to desired behavior using quantitative benchmarks. Return to design phase if performance is unsatisfactory.

ends, it is imperative to understand and control morphology and the response profiles of the engineered tissue's building blocks, cells, extracellular matrix components and cellular networks.

2.5 Economic Design: Exploit Cell Responses and Emergent Properties

Cells and extracellular matrix components are the building blocks of all tissues. Matching a tissue's list of components, is necessary, but not sufficient, to potentiate function; function is conferred by spatiotemporal organization and interaction of cells and their

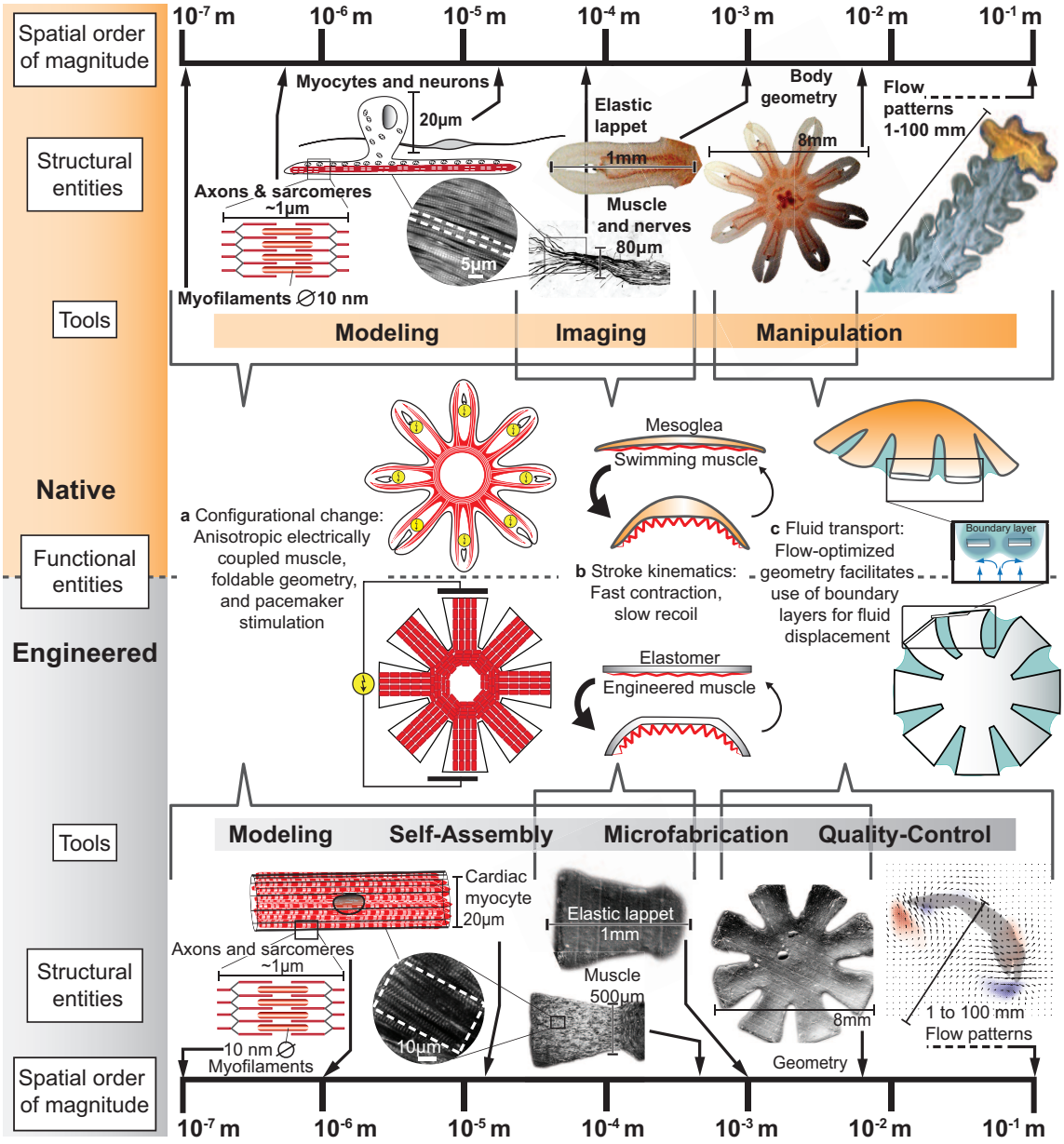

Figure 2.2. Structural and functional entities of jellyfish function, and engineered solutions. **Top half (yellow):** Structural entities in native jellyfish underlying swimming and feeding range from nanoscale contractile fibers to macroscale flow patterns. Modeling, imaging and experimental approaches reveal their relation to key functional entities: **a**, conformational change **b**, asymmetric stroke kinematics, and **c**, flow-optimized geometry. **Bottom half (grey):** Modeling, self-assembly, microfabrication, and quality control help to recapitulate these key functional entities with engineered materials across multiple spatial orders of magnitudes.

environment (Tsang et al. 2009). Microenvironmental cues such as matrix rigidity and the boundary conditions imposed on the cells drive the organization and function of cells and tissues (Grosberg et al. 2011). Substrate elasticity, for example, has been reported to contribute to mesenchymal stem cells commitment to neurogenic, myogenic or osteogenic phenotype (Engler et al. 2006). Further, changes in substrate elasticity can trigger remodeling in differentiated cells, such as the pathological adaptation of cardiomycoytes to fibrosis-associated matrix stiffening which alters cell-to-cell adhesion and ultimately impairs contractile function (McCain et al. 2012). Another example for microenvironmental cues are the systemic soluble factors accounting for age-associated decline of both myogenesis and neurogenesis in mice, such that progenitor cells from young animals exposed to blood serum from older animals assume the proliferation and regenerative capacities associated with aged systems, and vice versa (Villeda et al. 2011; Conboy et al. 2005). Other cues that influence cell behavior include spatiotemporal dynamics of extracellular matrix (ECM) components, signaling molecules, substrate topography and biomechanical forces (Keung et al. 2010) All of these agents present opportunities to turn cells into predictable building substrates and standardized components of tissues. Accordingly, various release and presentation schemes have been developed to incorporate chemical and physical cues into scaffolds, forming so-called microniches that trigger specific cell responses (Place et al. 2009). In the tissue-engineered jellyfish, muscle morphogenesis was controlled through micropatterning of fibronectin and suitable substrate stiffness (chapter 4).

Ensembles of cells, however, generate and sense mechanical, electrical and physiological properties not captured on the level of the microniche. Reentry, for example, the most common cause of cardiac arrhythmias, is an emergent property of the heart where particular combinations of conduction velocity, refractory periods, and tissue geometry generate a circular activation pathway (Lusis and Weiss 2010). The elastic recoil of lung tissue results from the multiscale organization of its cellular and matrix

constituents and cannot be understood from the properties of individual components (Suki and Bates 2011). Changes in cell motility can generate self-organization into patterned tissues (Chen et al. 2012), and cell polarity underlies spontaneous tube formation (Bryant and Mostov 2008). Conversely, tissue geometry and dimensions influence cell shape and force distributions within the cells, including distension of the cell nucleus which affects gene expression and differentiation (Ruiz and Chen 2008). In addition, cell ensembles can normalize the effects of stochastic gene expression, mutations, cell death and other sources that render single cell behavior unpredictable (Elowitz et al. 2002; Andrianantoandro et al. 2006). If understood and harnessed, such emergent properties need not be a nuisance but facilitate and economize building functional tissues. In the tissue-engineered jellyfish, for example, understanding the chain of effects linking myocyte shape, sarcomere alignment, electrical conduction and global force generation based on both empirical and computational studies (Shim et al. 2012; Alford et al. 2010; Bursac et al. 2002; Grosberg et al. 2011) provided clear guidelines for the design of swimming muscle and silicone substrate (chapters 4). Managing emergent properties, however, is not the only challenge when altering tissue dimensions; its complement is to preserve properties at various scales and conditions.

2.6 Physiological Scaling: Integrate Allometric and Dimensional Analysis

Preserving function in a tissue at altered scales or at different external conditions requires understanding how physiological function varies with spatiotemporal and environmental parameters. Allometric analysis generates quantitative expressions of how physiology scales with body dimensions but often stop short of providing mechanistic insights. One example is Kleiber's law (Kleiber 1932) which concludes from empiric data that the metabolic rate of an animal scales to the $\frac{3}{4}$ power of its mass. Although this relation has

been shown to hold for a surprising range of organisms, its mechanistic basis remains unresolved, possibly precisely because of the expectation that it should apply to single cells and elephants alike (Agutter and Tuszynski 2011), thereby limiting its use for systematic design studies. Greater promise for exposing biological structure-function relationships lies in focusing on functionally related systems with comparable constraints and pairing a systematic search for allometric laws in physiological data with dimensional analysis as performed in engineering and physical sciences. Dimensional analysis is a rigorous mathematical approach to identifying basic physical quantities, such as length, time and mass, and their interdependences relevant to explaining the functional characteristics of a system. Maintaining these relations when changing design parameters preserves kinematic and dynamic behavior, a concept called similitude, which allows, for example, for modeling the drag of cars based on data from miniature-sized models. In case of the synthetic jellyfish, dimensional analysis and computational modeling revealed how to achieve native propulsion efficiency by adapting the body geometry to account for the differences in fluid dynamics between seawater at 15°C and culture medium at 37°C (chapters 6 and 7). In another example, applying dimensional analysis to morphological and behavioral data of aquatic invertebrates revealed how access to nutrients and consequently the metabolic rate scale with flow parameters and body geometry (Patterson 1992). Similarly, Murray's law explains the geometric similarity of branching patterns in diverse fluid transport systems in animals and plants by showing that it keeps shear stress constant everywhere and minimizes the costs of flow and materials (LaBarbera 1984; Murray 1926).

Combining dimensional scaling laws with control of structure-function relationships at the level of cells and cellular networks provides the basis for the design of engineered tissues. The subsequent task is to develop fabrication strategies that can implement the design based on engineered materials and fabrication methods.

2.7 Fabrication Strategies: Exploit Microtechnologies and Self-Organization of Cells

A particular challenge for tissue-engineering is the reproduction of anisotropy that characterizes biological systems at various scales and is crucial to conferring functional characteristics, e.g., cell polarity, extracellular fiber orientation and preferential electrical conductivity. Which parts of this organization should be created by micro- and nanofabrication? Which parts can develop from physical and chemical processes (e.g., diffusion gradients, self-assembly, degradation)? And which parts are best left to the self-organizing powers of cells, an extreme example of which is given by the maze-solving abilities of the slime mold (Nakagaki et al. 2000)?

Attempts to engineer interfacial tissues, which are particularly rich in anisotropy, exemplify the advantages of exploiting cellular self-organization as part of the fabrication process. Tissue interfaces include bonds of mechanically dissimilar materials such as ligament-to-bone and cartilage-to-bone transitions where anisotropic structural properties gradually vary from one tissue to another and thereby reduce the risk of rupture. Such transition zones can be generated by self-organization of cellular phenotypes along gradients of soluble factors or physical properties. For example, differentially activating bone-specific gene expression using a microfabricated gradient of transcription factors resulted in a mineralization gradient that mimicked the mechanics and microstructure of native ligament-to-bone interfaces (Phillips et al. 2008). Also, as discussed earlier, stem cell differentiation is induced by substrate elasticity, often resulting in cell types that reinforce the mechanic characteristics of their environment, such as bone formation on stiff substrates (Engler et al. 2006). This response can be exploited for generating cell type and substrate gradients at finer resolution than would be possible with microfabrication (Seidi et al. 2011). In the case of the tissue-engineered jellyfish, macroscale body shape was carved by micromachining, photolithography generated features at cel-

lular resolution (ECM patterns with 20 μm line width), and cellular self-organization accomplished the alignment of subcellular entities (e.g., myofibrils and gap junctions) (chapter 4).

Importantly, fabricated tissues must meet structural benchmarks defined during the design process. It is equally important to choose well-defined criteria for system-level performance tests. Otherwise, no insight can be gained from the response of the final construct.

2.8 Evaluate Function: Use of Traditional and Novel Physiological Metrics at System Level

Systematic evaluation and optimization of tissue design requires common performance benchmarks for engineered and native systems. As case in point, the synthetic jellyfish was evaluated based on quantitative measures of flow field dynamics and feeding/swimming performance established in native medusae (Feitl et al. 2009; Dabiri et al. 2005), which are discussed in detail in chapter 8. However, whereas assessing cellular function by means of gene expression, protein synthesis and ionic fluxes has become standard practice across biological sciences, the functional evaluation of entire organs or organisms remains rare outside the domain of medical education or marine biomechanicians (e.g., Romanes 1898). Yet whole-organ studies can generate comprehensive functional data unattainable from cell cultures and other reduced experimental platforms. The Langendorff preparation, for example, a classical mammalian heart preparation, enables the study of contractile function, heart rate, vascular tone and cardiac metabolism over the course of several hours, (Bell et al. 2011; Skrzypiec-Spring et al. 2007; Wiechert et al. 2003). Complementary to preserving traditional physiology assays is the development of novel functional metrics that facilitate evaluating biological and engineered structures at system level. A recently described universal index of efficiency in fluid

transport via vortex formation, for example, applies to heart output, squid propulsion and piston pumps alike and gave rise to a noninvasive assay for assessing cardiac function and disease progression based on echocardiographical data (Dabiri 2009; Gharib et al. 2006). Beyond its diagnostic function, the efficiency index is also a promising candidate for evaluating tissue-engineered heart repairs and substitutions.

2.9 Conclusions

Developing design standards for engineered tissues will not only advance the creation of artificial organs and novel biological tools but also improve *in vitro* disease models currently limited to 2D cell cultures (Hutmacher 2010). As outlined in this chapter, it requires implementing the classical engineering algorithm (design, build, test) based on mechanistic understanding of the tissue's building substrates, dimensional scaling laws, multimodal fabrication strategies and system-level performance metrics. Importantly, quality control should be part of tissue engineering, and in many cases, this will cover both multiscale histology and organ-level physiological performance. Implementing the design-build-test algorithm will rely on both empirical and computational tools; the latter will be of particular benefit to design studies, dimensional scaling analysis and fabrication optimization. The greatest challenge, however, will be to provide scientists with the background and training needed to comfortably navigate the engineering algorithm's landscape (figure 2.3) spanned by various scientific and engineering disciplines (i.e., medicine-to-informatics axis), multiple spatial orders of magnitude (i.e., nanoscale-to-macroscale axis), and complementary modes of analysis (i.e., structure-to-phenomenon axis).

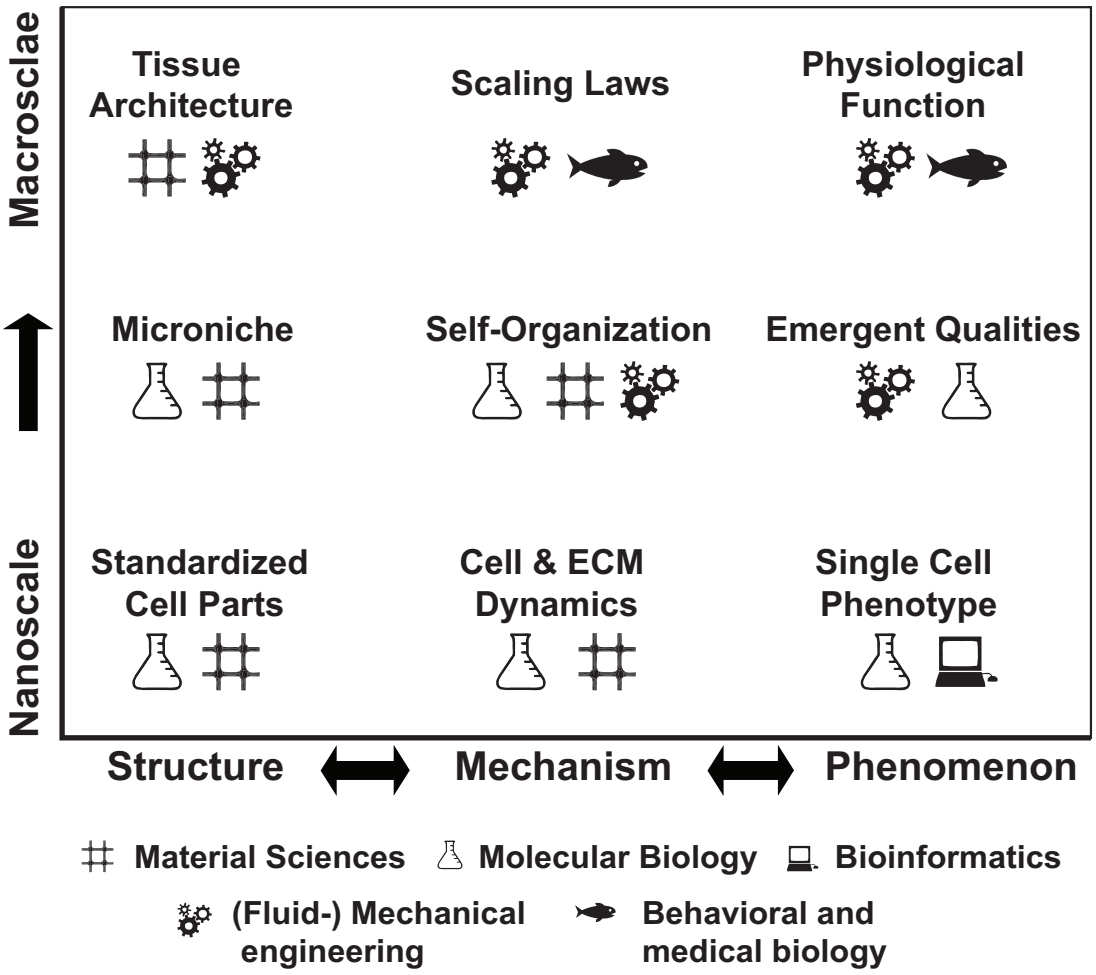

Figure 2.3. Simplified design-build-test landscape for tissue engineering.

Employing the design-build-test algorithm to engineer tissues and develop design standards involves the analysis, recapitulation and testing of materials, mechanisms and phenomena (abscissa) across multiple orders of magnitude (ordinate axis), a task that requires expertise and interaction of various scientific and engineering disciplines (examples indicated with icons).

Chapter 3

Proof of Concept: A Tissue-engineered Jellyfish with Biomimetic Propulsion

3.1 Motivation

> "If only anatomists were as familiar with the dissection of lower animals as with that of the human body, all these perplexing difficulties would, in my opinion, be cleared up." (William Harvey, 1648)[1]

In the spirit of William Harvey, the 17th century intrepid explorer of circulatory systems in amphibians, reptilians, worms and mollusks, it appears prudent to begin any engineering enterprise aimed at recapitulating nature's design by examining systems of reduced complexity. Though the concepts discussed in the previous chapter are framed with the long term goal in mind of devising organ replacements or muscle-powered robots, their implementation requires the understanding of the basic building blocks of any tissue, i.e., living cells and extracellular matrix components. It is thus not a deviation but an intermediate step and valuable exercise to first look at organisms readily accessible to the analysis of structure-function relationships, such as transparent jellyfish medusae characterized by a limited number of cell types and behaviors (Arai 1997), and to attempt a translation of their design principles to tissue-engineered materials.

[1] In "Exercitatio anatomica de motu cordis et sanguinis in animalibus" (Harvey and Leake 1928, reprinted)

The proof-of-concept study presented in the following summarizes the design, construction and evaluation of a tissue-engineered jellyfish with biomimetic swimming function, which, beyond representing a novel prototype of an *in vitro* muscular pump, exemplifies the power of a systematic engineering strategy. In order to not detract from this main point, the details of experimental methods and research tools employed in the study will be discussed in subsequent chapters.

3.2 A Tissue-Engineered Jellyfish with Biomimetic Propulsion

This chapter was submitted to Nature Biotechnology on December 7, 2011 and published online July 22, 2012. It is reproduced as is except for minor improvements of references, formatting and figure presentation. The supplementary materials section has been expanded and distributed onto subsequent chapters.

3.3 Authors

Janna C Nawroth[2], Hyungsuk Lee[3], Adam W Feinberg[3], Crystal M Ripplinger3, Megan L McCain[3], Anna Grosberg[3], John O Dabiri [4] & Kevin Kit Parker[3]

3.4 Author Contributions

K.K.P., J.O.D. and J.C.N. conceived the project and designed the experiments. J.C.N. prepared manuscript & figures, performed the experiments and analyzed the data.

[2]Division of Biology, California Institute of Technology, Pasadena, California, USA
[3]Disease Biophysics Group, Wyss Institute for Biologically Inspired Engineering and School of Engineering and Applied Sciences, Harvard University, Cambridge, Massachusetts, USA.
[4]Graduate Aeronautical Laboratories and Bioengineering, California Institute of Technology, Pasadena, California, USA

K.K.P.and J.O.D. advised and made final edits to the manuscripts. J.O.D. and J.C.N. developed the fluid model. H.L., A.W.F., C.M.R., A.G. and M.L.M. provided training, aided in analyzing data and gave conceptual advice. M.L.M. isolated rat cardiomycoytes for experiments.

3.5 Abstract

Recent advances in the mechanistic understanding of biosynthetic compound materials (von der Mark et al. 2010; Mitragotri and Lahann 2009; Place et al. 2009), computer-aided design approaches in molecular synthetic biology (Fu 2006; Kaznessis 2007) and traditional soft robotics (Bar-Cohen 2006 2004), and increasing aptitude in generating structural and chemical microenvironments that promote cellular self-organization (Alford et al. 2010; Grosberg et al. 2011; Huang et al. 2010) have enhanced the ability to recapitulate such hierarchical architecture in engineered biological systems. Here we combined these capabilities in a systematic design strategy to reverse engineer a muscular pump. We report the construction of a freely swimming jellyfish from chemically dissociated rat tissue and silicone polymer as a proof of concept. The constructs, termed "medusoids", were designed with computer simulations and experiments to match key determinants of jellyfish propulsion and feeding performance by quantitatively mimicking structural design, stroke kinematics and animal-fluid interactions. The combination of the engineering design algorithm with quantitative benchmarks of physiological performance suggests that our strategy is broadly applicable to reverse engineering of muscular organs or simple life forms that pump to survive.

3.6 Introduction

Jellyfish represent a unique test case for design-based tissue engineering of a functional device as their repetitive behavior and simple bauplan facilitate probing, and poten-

tially emulating, structure-function relationships. Jellyfish medusae feature a radially symmetric, transparent body powered by a few, readily identifiable cell types, such as motor neurons and striated muscle (Anderson and Schwab 1981; Arai 1997) and they generate quantifiable output functions, for example, well-defined feeding and swimming currents (Dabiri et al. 2005; Costello and Colin 1995), based on straightforward body-fluid interactions (Feitl et al. 2009; Nawroth et al. 2010). We started by identifying the key factors contributing to the jellyfish stroke cycle and its functions, that is, feeding and propulsion (figure3.1a and supplementary movie 1), with the goal of determining potential functional substitutes from tissue-engineering materials. First, previous studies and observations (Widmer 2008; Gladfelter 1973) have highlighted the importance of symmetric and complete bell contraction, which the jellyfish achieves by synchronously activating its axisymmetric musculature through a system of distributed pacemakers, resulting in controlled folding of the lobed or otherwise compressible bell (figure 3.1b, top) (Satterlie 2002; Gladfelter 1972; Passano 1965). We reasoned that a sheet of electromechanically coupled, anisotropic cardiac muscle tissue synchronized by an electrical field would be functionally equivalent (figure 3.1b, bottom). Second, jellyfish stroke kinematics derive from the alternating action of fast muscle contraction and slow elastic recoil of the bell's compliant gelatinous matrix (mesoglea), corresponding to the power and recovery strokes (figure 3.1c, top) (Gladfelter 1972). For the engineered construct, we envisioned that a bilayer of muscle and synthetic elastomer would be suitable to mimic this interaction, that is, the muscle would provide the force to contract the bell, and the elastomer would act to restore the original shape (figure 3.1c, bottom). Third, previous research has highlighted the contribution of viscous, fluid boundary layers to efficient solid-fluid interactions in juvenile medusae and other aquatic organisms (figure 3.1d, top) (Koehl et al. 2001; Koehl 2004; Feitl et al. 2009; Nawroth et al. 2010). We concluded that the geometry of our construct should be chosen based on ambient fluid conditions so as to facilitate the formation of boundary layers that fill the gaps between

neighboring lappets (figure 3.1d, bottom).

We then investigated in detail how the tissue components of juvenile specimens, so-called ephyrae, of the scyphozoan jellyfish *Aurelia aurita* generate these three key properties, and in parallel attempted to select and assemble functionally equivalent substitutes from synthetic and tissue-engineered materials.

3.7 Methods and Materials

3.7.1 Actuation and Configurational Change

In *Aurelia aurita*, bell contraction relies on a monolayer of striated muscle lining the subumbrella (Chapman 1999; Anderson and Schwab 1981). Using chemical staining, we mapped the cellular architecture of the swimming muscle in *Aurelia sp.* ephyrae, which consists of a central ring merging into eight radial branches (section 4.4). Jellyfish myofibrils displayed a high degree of alignment, and longitudinal continuity suggested mechanical end-to-end coupling of muscle cells (Blanquet and Riordan 1981). Optical mapping of membrane voltage potential revealed that, at least locally, action potentials propagate continuously within jellyfish muscle (section 4.3), whereas global coordination of muscle activation is thought to be accomplished by a networked ensemble of pacemaker cells (Satterlie 2002; Hayward 2007). Together, these findings suggested that highly ordered myofibril organization paired with spatiotemporal coordination of contraction would be critical to emulating jellyfish muscle function. As it turns out, these properties are intrinsic to engineered monolayers of anisotropic rat cardiac tissue designed to mimic the laminar structure of the heart ventricles (Grosberg et al. 2011). Given a suitable micropattern of extracellular matrix cues, neonatal rat cardiomyocytes self-assemble into a functional syncytium with well-defined axes of force generation (Shim et al. 2012; Böl et al. 2008). Cell-to-cell electromechanical coupling promotes tissue-wide propagation of electrical impulses and spatiotemporal synchronization of contraction, which differen-

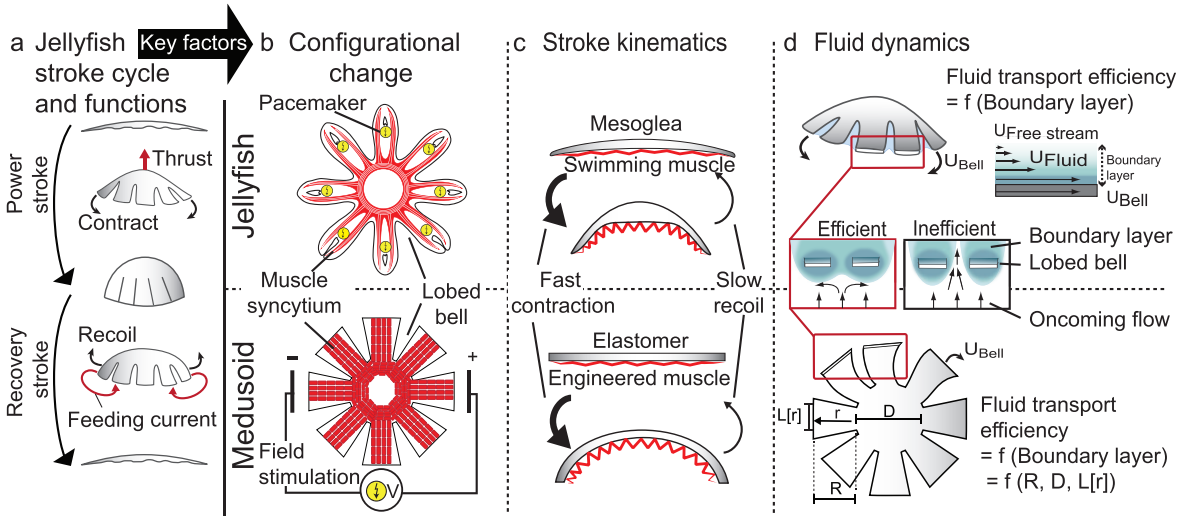

Figure 3.1. Key concepts of fluid transport in jellyfish and *in vitro* implementation.

a, Schematics of jellyfish stroke cycle generating thrust during the power stroke, and feeding currents during the recovery stroke. **b**, Controlled configurational change. Symmetric, complete bell contraction is mediated by anisotropic striated muscle tissue, a functional syncytium synchronized by a system of distributed neuronal pacemaker centers (jellyfish, top). This mechanism can be approximated by electrical field stimulation of electromechanically coupled, anisotropic cardiac muscle (medusoid, bottom). In either case, lobed geometry facilitates circumferential constriction of the bell. **c**, Stroke kinematics. In the bilayered design of jellyfish (top) and medusoid (bottom), a flexible elastomer opposes an actuator, which promotes asymmetric stroke patterns: active, fast contraction and passive, slow recoil. **d**, Fluid dynamics. Fluid velocity gradients, so-called boundary layers, extend effective reach of lappets (top). Overlapping boundary layers close interlobate gaps to oncoming flow. This prevents leakage and inefficient fluid transport despite the presence of gaps (center). Optimized medusoid body geometry favors the formation of boundary layer overlap and thus efficient fluid transport (bottom).

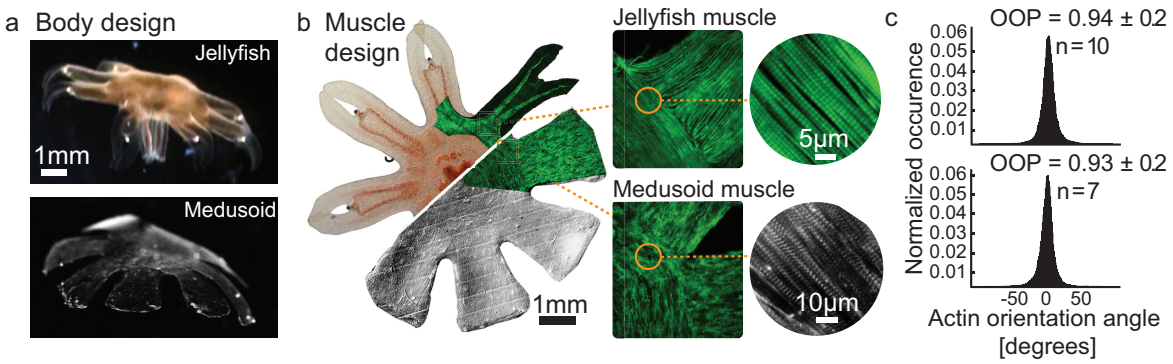

Figure 3.2. Body and muscle geometry in jellyfish and medusoid.

a, Body design of jellyfish (top) and free-swimming medusoid construct (bottom). Comparison demonstrates similar geometry and dimensions but also illustrates that the medusoid constitutes a simplified version of a jellyfish, reduced to elements necessary for propulsive function. **b**, Jellyfish 2D muscle architecture (top) was reverse engineered in medusoids (bottom). Left: Composite brightfield image overlaid with F-actin stain (green) of muscle cell monolayer. Square inset: Close-up on muscle organization at lappet-body junction; F-actin stain (green). Note that jellyfish muscle tissue consists of a single layer of myofibrils, here in focus, whereas engineered medusoid muscle tissue contains a stack of myofibrils, most of them being out of focus and blurring the image at this resolution. Circular inset: microstructure of single myofibril layer; F-actin stain (green), sarcomeric α-actinin (gray). **c,** Distribution of actin fiber orientation angles within single myofibril layer (centered on zero). Quantitative analysis of multiple fields of view revealed no significant difference in the orientation organization parameter (OOP) ($p = 0.61$, $n = 10$; two-sample t-test).

tiates cardiomyocytes from most other contractile cell types, such as skeletal myocytes. In particular, engineered cardiac tissue constructs contract synchronously when electric field stimulation is applied (Feinberg et al. 2007), eliminating the need for internal innervation by means of neuronal cells or embedded electrodes. We modeled medusoid body design after that of early-stage ephyrae, which do not possess a closed bell but an array of eight lappets, or lobes, arranged radially to a central disc (figure 3.2a). We emulated jellyfish myofibril organization in a monolayer of patterned neonatal rat cardiomyocytes, as evidenced by morphology at different scales as well as quantification of actin fiber alignment figure 3.2b,c and section 4.2). Further, optical mapping of membrane voltage potential confirmed the continuous spread of electrical activity through the nerve-free cardiac tissue (section 4.3). Next, we identified suitable substrates to substitute for mesoglea in stroke kinematics. Jellyfish stroke kinetics result from the cooperative effects of muscle and mesoglea mechanics, the former constricting the bell during the power stroke, the latter restoring the original shape through elastic recoil during the recovery stroke. In the medusoid, we attempted to create a similar interaction by coupling a layer of anisotropic cardiomyocytes with an elastic silicone substrate of adjustable stiffness (Fu 2006; Feinberg et al. 2007). Millimeter-scale medusoid constructs were fabricated by seeding neonatal rat cardiomyocytes onto micropatterned, jellyfish-shaped, polydimethylsiloxane (PDMS) thin films (4.2). Thus, PDMS surface modifications controlled 2D tissue architecture, whereas the overall medusoid shape was equal to PDMS film dimensions. Jellyfish mesoglea, however, is a heterogeneous substrate with soft folds allowing for compression and with stiffened ribs serving as springs and pivots around which the substrate can bend into a bell (Gladfelter 1973). A homogeneous disc of PDMS, on the other hand, is incompressible and cannot be turned into a bell without wrinkling, buckling or cracking, all of which require considerably higher stresses than bending (Feinberg et al. 2007). As a result, a naive biomimetic approach of precisely copying the muscle architecture and circular body shape of late-stage ephyrae

led to minimal film deformation and no propulsion at all (section 4.4 and supplementary movie 2). Successful medusoid designs must therefore match muscle stress generation with substrate compliance. In the lobed design, each arm freely bends around its base such that circumferential compression is avoided and a quasi-closed bell is formed at maximal contraction. Lappet bending angle was maximized by aligning the muscle fibers to the main axis of deformation and using minimal film thickness (ca.22 μm) without compromising stability, exploiting the known relation between myocyte tissue architecture, PDMS film thickness and resulting curvature of contraction. In particular, anisotropic engineered cardiac tissue generates peak stresses of 10 to15 mN mm^{-2}, which is similar to native cardiac muscle and sufficient to bend PDMS membranes of 20 μm thickness at a curvature of 1 mm^{-1}, meaning that a 2 mm long lappet will be arched by more than 90° (section 4.5). Conversely, in the bell's center, where little deformation was required, a circumferential muscle layout was implemented to facilitate electrical conduction between neighboring lappets, as action potential propagation velocity is fastest along the longitudinal axis of an anisotropic syncytium (Bursac et al. 2002). Medusoids of this design responded to electrical field stimulation applied by two U-shaped electrodes flanking the bath (1 Hz, 2.5 V cm^{-1}, 10 ms pulse width; cf.section 4.3 for details), with power and recovery strokes that closely resembled the stroke cycle of freely swimming jellyfish ephyrae (figure 3.3a and supplementary movies 3 and 4).

3.7.2 Stroke Kinematics

Constructs were assayed for up to 1 h, after which contractility and responsiveness to pacing decreased, presumably due to tissue damage resulting from electrical and manual manipulation. Tracking lappet displacement relative to the main body revealed qualitatively similar velocity-time functions of lappet motion in medusoid constructs compared to ephyrae (figure 3.3b). In particular, the greatest lappet acceleration and velocity were reached during the power stroke, followed by more gentle recovery. Quantitative analy-

sis confirmed a similar degree of lappet synchrony in the two systems as well as similar ratios of contraction and relaxation velocities (figure 3.3c,d). These results demonstrate that mechanistic understanding of the desired function and of available materials makes it possible to design and build constructs that exhibit similar macroscopic behaviors as the model system without necessarily sharing all underlying components.

3.7.3 Fluid Dynamics

Adequate three-dimensional kinematics do not, however, guarantee efficient body-fluid interactions, which must be considered separately. In particular, although emulating the ephyral body plan facilitates compression-free deformation, this design also risks "leaking" fluid through the gaps, and thus compromising fluid transport, unless lappet shape promotes sufficient bell drag, that is, the formation of overlapping viscous boundary layers to resist gap-crossing flows (Feitl et al. 2009; Nawroth et al. 2010). Viscous boundary layers are fluid velocity gradients that form at the fluid-animal interface and follow the motion of the lappets, effectively extending their reach. Boundary layers of sufficient thickness overlap and close interlobate gaps to oncoming flow, thus increasing bell drag. The factors determining bell drag are lappet Reynolds number (the local ratio of inertial to viscous fluid forces) and bell porosity (gap width relative to lappet width), or, more directly, fluid viscosity, lappet kinematics and body geometry. We developed and empirically validated a fluid dynamics model that determined optimal parameters of the jellyfish-like geometry for transporting isotonic Tyrode's solution at 37°C (mammalian cell culture conditions) while adhering to structural stability and fabrication constraints (chapter 7). The corresponding medusoid design features wedge-shaped lappets separated by gaps (figure 3.2a) that allow compression-free, collision-free deformation, whereas fluid leakage is resisted through formation of viscous boundary layers.

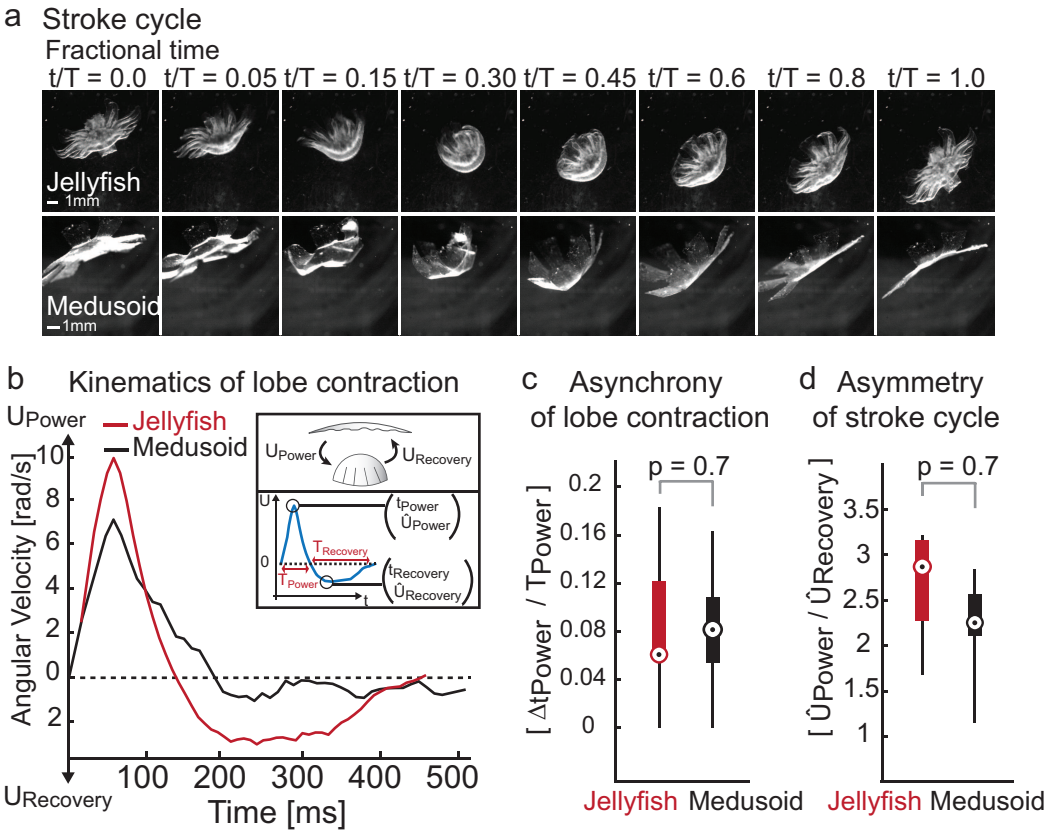

Figure 3.3. Medusoids were engineered to exhibit jellyfish-like stroke kinetics.

a, Time lapse of stroke cycle in jellyfish (top) and medusoid paced at 1 Hz (bottom); t, time (s) elapsed since start of stroke cycle; T, duration of stroke cycle; here: jellyfish, $T = 0.3$ s; medusoid, $T = 1.0$ s. **b**, Average trace of angular velocity of individual bell lappets throughout stroke cycle in juvenile jellyfish and medusoids ($n = 9$ lappets each). Inset illustrates characteristic parameters of stroke cycle (top) and velocity-time graph (bottom). $T_{power/recovery}$, duration of power/recovery stroke; $U_{power/recovery}$, velocity of power/recovery stroke; $\hat{U}_{power/recovery}$, peak velocity of power/recovery stroke; $t_{power/recovery}$, time point of peak power/recovery stroke velocity. **c** and **d**, Box-plot representation. Bull's eyes, median; lower edge of box, 25th percentile; upper edge of box, 75th percentile; whiskers, extreme data points. **c**, Relative asynchrony of lappet contraction. Asynchrony did not differ significantly in jellyfish and medusoids ($p = 0.7$, Wilcoxon rank sum test, $n = 4$ lappet pairs each). Δt_{power}, difference between time points of peak power stroke velocities in pair of lappets. **(d)** Ratio of maximal lappet velocities during power and recovery stroke did not differ significantly in jellyfish and medusoids ($p = 0.7$, Wilcoxon rank sum test, $n = 9$ lappets each).

3.8 Results

Medusoids with optimized muscle and PDMS geometry succeeded in replicating jellyfish swimming behavior (supplementary movies 3 and 4) and achieved similar propulsion and feeding performances. In particular, digital particle image velocimetry (DPIV) (chapter 8 and supplementary movie 5) revealed qualitatively and quantitatively similar flow fields generated during bell contraction. Both medusoid and jellyfish power strokes generated fluid velocities between 6 and 10 mm s^{-1}, indicating similar momentum transfer (figure 3.4a,b and supplementary movies 6 and 7). DPIV also revealed the wake structures formed due to bell acceleration and motion reversal. The presence of a so-called stopping vortex, a ring of circulating fluid shed during the recovery stroke, suggested that jellyfish-like feeding currents, which draw fluid inside the bell, were produced by the medusoid construct (figure 3.4d,e and supplementary movies 6 and 7). Changes to medusoid geometry resulted in altered fluid interactions (figure 3.4c,f), which will be discussed in detail later. Medusoid and jellyfish propulsion performances were expressed in units of body lengths traveled per swimming stroke (BL/S), a common metric for biological locomotion for efficiency that normalizes for size differences between the specimens that are being compared (Vogel 1996). Here, body length was defined as bell height at maximal contraction (figure 3.5a, inset). Medusoid performance mostly ranged between 0.4 and 0.7 and occasionally reached values close to 1 BL/S. Upper medusoid performance thus covered the span of regular ephyral swimming efficiency, which varied between 0.6 and 0.8 BL/S (figure 3.5a). Relative feeding performance was given by nondimensionalized volumetric flux across the underside of the bell during the recovery stroke. These metrics were drawn from DPIV data and quantify the rate of fluid turnover at the solid-liquid interface. In ephyrae, this rate determines the efficiency of transporting prey items to the subumbrellar feeding structures, hence the term "feeding performance". Comparison of volumetric flux across the entire bell revealed that

medusoids and ephyrae processed fluid at similar rates during each stage of the recovery stroke (figure 3.5b). Total volumetric flux in the medusoid equaled 75% of ephyral flux. The corresponding velocity profile of medusoid and jellyfish confirmed positive flux, that is, flow toward the bell, of similar magnitude throughout the stroke cycle (figure 3.6). Note that the pronounced "M"-shaped velocity profile observed in the ephyrae derives from the fact that the central oral arms (not present in medusoids) are diverting the flow.

For comparison, we also tested a suboptimal layout featuring slim, straight lappets. This body plan is adopted by ephyrae exposed to relatively low water temperatures where increased kinematic viscosity and thicker boundary layers allow for greater gaps between lappets without compromising fluid transport as boundary layer overlap is maintained. Exposed to the lower viscosity conditions at warmer temperatures, this same body plan provides little resistance to the flow and effectively sieves through the fluid instead of transporting it (Chapter 6; Nawroth et al. 2010). Similarly, sieve-designed medusoids accelerated the fluid to no more than 50% of the velocities reached by the original design, which was optimized for 37°C (figure 3.4b,c and supplementary movie 8), resulting in a 60% reduction of median propulsion performance (figure 3.5a and supplementary movie 4). Further, although sieve-designed medusoids generated a stopping vortex ring during the recovery stroke (figure 3.4e,f and supplementary movie 8), they nonetheless exhibited an 80% reduction in total volumetric flux toward the bell compared to optimal medusoids (figure 3.5b). As the velocity profile reveals, the reduced feeding performance was due to lower flow rates as well as reversal of flow, which corresponds to expelling potential prey from the bell (figure 3.6).

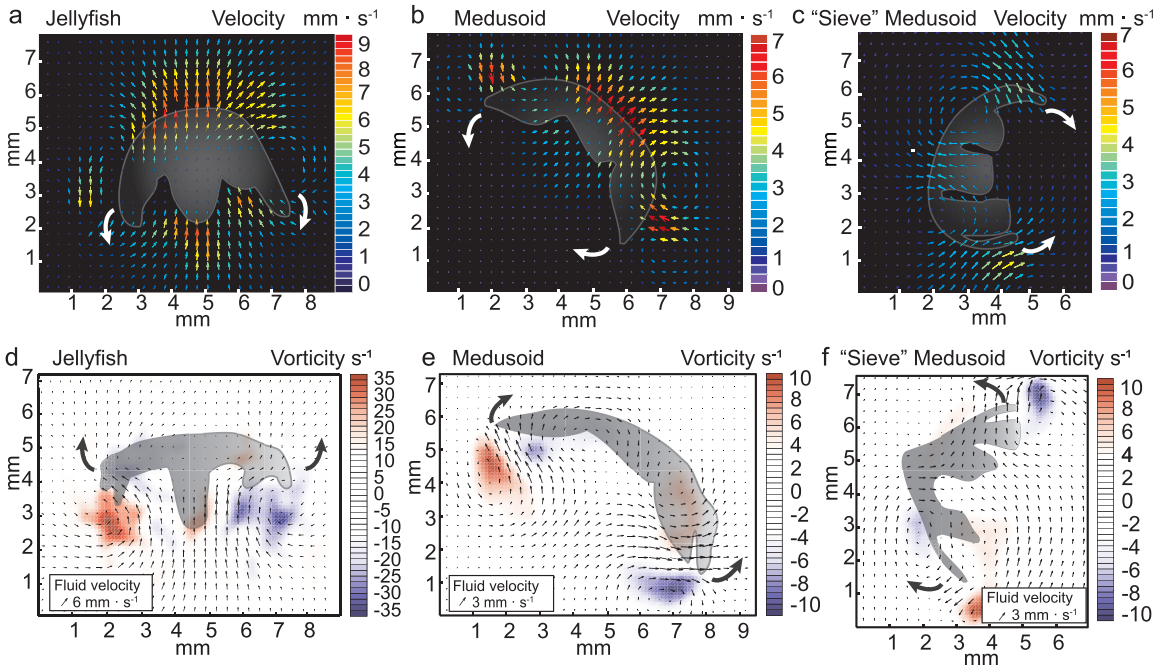

Figure 3.4. Medusoids generated jellyfish-like flow fields.

a–**c**, Velocity field at end of power stroke reveals similar thrust generation in **a**, jellyfish and **b**, medusoids, and reduced thrust in **c**, sieve-designed medusoids. White arrows, lappet motion. **d**–**f**, Vorticity field during recovery stroke reveals similar formation of stopping vortices in **d**, jellyfish, **e**, medusoids, and **f**, sieve-designed medusoid. Blue and red contours, counterrotating cross sections of stopping vortex ring; gray arrows, lappet motion.

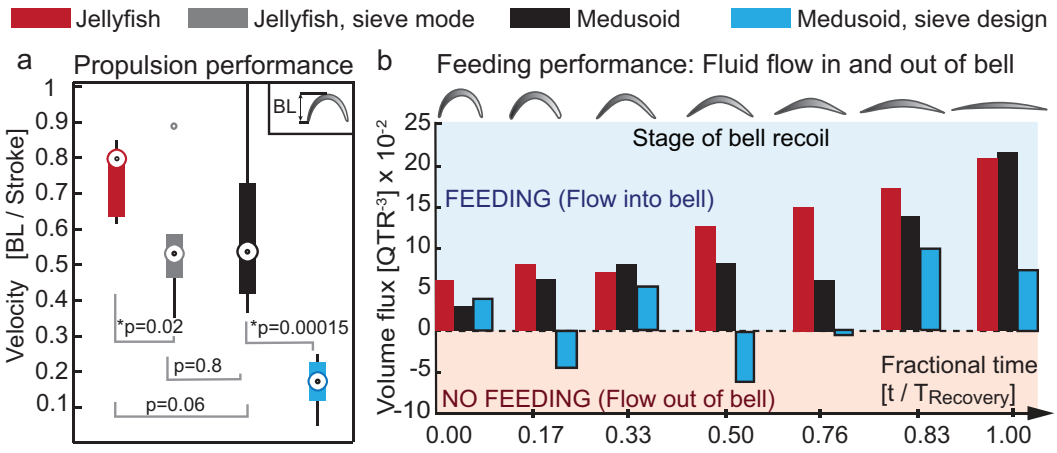

Figure 3.5. Medusoids achieve functional performance of jellyfish.

a, Box-plot representation of propulsion performances in BL/S. Jellyfish ($n = 7$, red) and optimally designed medusoids ($n = 11$, black) perform comparably while jellyfish in sieve conditions ($n = 7$, blue) and sieve-designed medusoids ($n = 6$, gray) perform significantly worse ($p = 0.02$ and $p = 0.00015$; Wilcoxon rank sum test). Bull's eyes, median; lower edge of box, 25th percentile; upper edge of box, 75th percentile; whiskers, extreme data points; circle, outlier. Asterisks, statistically significant difference, i.e., $p < 0.05$. **b**, Volume flow rate in and out of bell during recovery stroke, indicating feeding, or failure to feed, respectively. Q, volume flow rate (mm^3/s) Details are provided in figure 3.6.

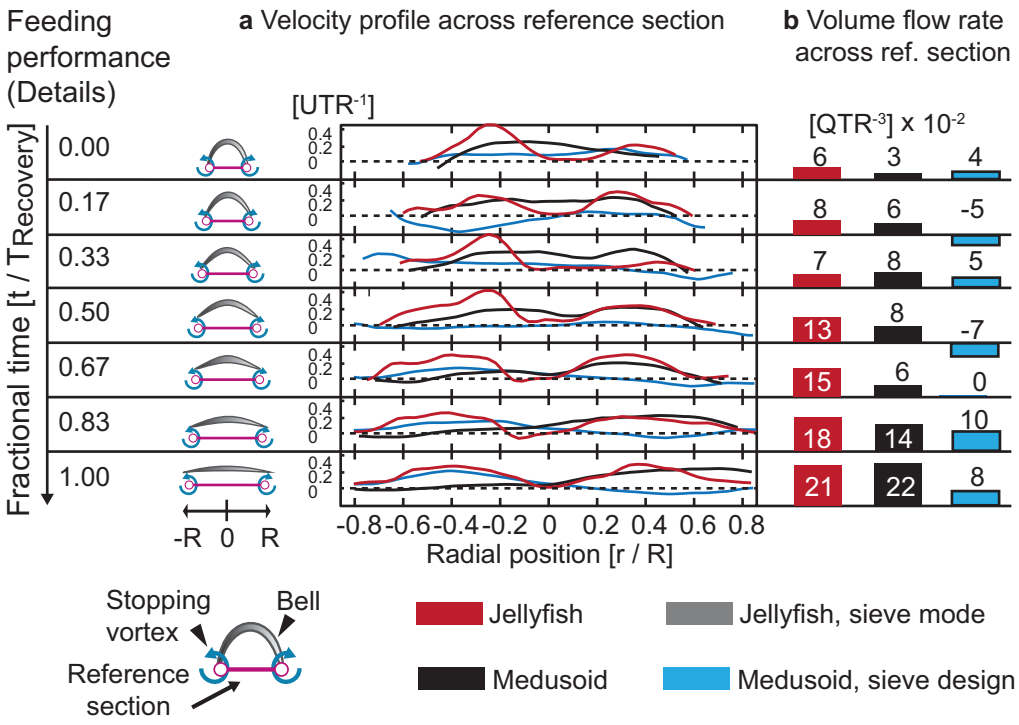

Figure 3.6. Details of feeding performance.

For each stage of the recovery stroke (left), flow profile (i) and volume flow rate (ii) across subumbrellar reference section reveal similar fluid transport in jellyfish and medusoids, and reduced performance—including flow reversal—in sieve-designed medusoids. Data shown for one representative sample each. R, bell radius (mm); jellyfish: $R = 9$ mm; medusoid: $R = 9$ mm; sieve-designed medusoid: $R = 9$ mm; r, radial distance (mm) from center. $T_{recovery}$, duration (s) of recovery stroke; jellyfish: $T = 0.2$ s, medusoid, $T = 0.48$ s; sieve-designed medusoid, $T = 0.55$ s; t, time (s) elapsed since start of recovery stroke. U, flow velocity [mm/s] normal to reference section; jellyfish: $U_{max} = 9$ mm/s; medusoid: $U = 2.4$ mm/s; sieve-designed medusoid: $U_{max} = 1.6$ mm/s. Q, volume flow rate (mm^3/s) passing across reference area; jellyfish: $Q_{max} = 100$ mm^3/s; medusoid: $Q_{max} = 40$ mm^3/s; sieve-designed medusoid: $Q_{max} = 15$ mm^3/s.

3.9 Discussion

This study extends the process of designing novel biological or bioinspired systems to the realm of pseudoorganisms. We have employed traditional quantitative engineering approaches to build a millimeter-scale construct from living and synthetic materials that emulates typical jellyfish behaviors. Our current work builds on our previous work in biohybrid actuators (Feinberg et al. 2007), where the objective was to build a biologically powered mechanical device. We have demonstrated here how such devices can be designed and incorporated into synthetic organisms that mimic the biological function of an organism. As shown here for muscle-powered fluid transport, the main challenge for macroscale synthetic biology is to dissect complex behaviors into mechanistic components that have functionally equivalent, tissue-engineered solutions. Our results illustrate that a biomimetic design does not always reproduce the intended function (section 4.4 and supplementary movie 2), and that complex behaviors can be generated from relatively few materials by establishing key interactions with cells that exploit their powers of self-organization. In conclusion, we have succeeded in recreating jellyfish swimming, a well-defined animal behavior, in an artificial tissue construct. At this stage, swimming behavior is limited to exactly one stereotypic mode of execution because we have no means of fine-controlling local muscle contraction to achieve, for example, turning and maneuvering. However, the future integration of multiple cell types and compound materials will allow for constructs of greater autonomy that are capable of sensing the environment and employing internal decision-making circuits to choose a suitable response from a variety of behaviors. Our design algorithm is applicable to the assembly of any synthetic muscular pump. With respect to the engineering of tissues or organs intended for therapeutic use in patients, our results highlight the importance of developing and applying quantitative performance specifications. With simple model systems, the design of these specification standards can be accomplished in carefully

controlled conditions.

3.10 Acknowledgements

We acknowledge financial support from the Wyss Institute for Biologically Inspired Engineering at Harvard, the Harvard Materials Research Science and Engineering Center under National Science Foundation award number DMR-0213805, US National Institutes of Health grant 1 R01 HL079126 (K. K. P.), and from the office of Naval Research and National Science Foundation Program in Fluid Dynamics (J. O. D.). We acknowledge the Harvard Center for Nanoscale Science for use of facilities and the New England Aquarium for supplying jellyfish. We thank J. Goss, P.W. Alford, K.R. Sutherland, K. Balachandran, C. Regan, P. Campbell, S. Spina and A. Agarwal for comments and technical support.

Chapter 4

Design Principle Configurational Change: Morphological Features Enabling Bell Contraction, and Their Implementation *In Vitro*

This chapter expands on the methods and supplementary information of Nawroth et al. (2012) reproduced in chapter 3. The thesis author has contributed all text and data unless noted otherwise. sections 4.2 and 4.3 closely follow the published materials, whereas sections 4.4 and 4.5 constitute novel additions except for individual figure components.

4.1 Overview

The locomotive system of *Aurelia aurita*, or moon jellyfish, and other jellyfish medusae consists of a monolayer of striated muscle fibers arranged in a sheet and anchored to the mesogleal matrix, a gelatinous hydrogel interwoven by neuronal processes and a variety of elastic and structural fibers (Anderson and Schwab 1981; Gladfelter 1973; Megill et al. 2005; Gambini et al. 2012). Muscle activation contracts the mesoglea during the power stroke, which pushes fluid rearward and propels the animal forward. Whereas in squid one set of muscle powers the contraction phase and another helps to refill the mantle (Gosline and DeMont 1985), jellyfish medusae lack such antagonistic setup,

and the recovery stroke results from passive recoil of the mesoglea deformed during the contraction (Megill 2002; Demont and Gosline 1988; Gladfelter 1972).

The parameters that characterize the locomotive system include body shape, mechanical properties of the mesogleal matrix, muscle cell morphology and neuromuscular arrangement (Gladfelter 1972 1973). Interestingly, most jellyfish species can be classified by only two categories of locomotive designs whose structural and functional aspects are optimized for either powerful jet propulsion, or efficient drag-based rowing (Dabiri et al. 2007; Costello and Colin 1995). *A. aurita* falls into the latter category and as such possesses an oblate, saucer-shaped body, as opposed to the prolate profile of typical jetters. Its planar, 2D body and muscle architecture lends itself to imaging, structural analysis and reverse engineering. This chapter discusses key elements of muscle actuation and body deformation in juvenile *A. aurita* medusae (the so-called ephyral stage) and how they were implemented in the medusoid. In particular, the ability to reverse-engineer jellyfish muscle anisotropy (section 4.2) was essential for the systematic probing of structure-function relationships, i.e., electrical conductivity underlying synchronous contraction addressed in section 4.3, and the effect of muscle arrangement and substrate geometry on bell deformation discussed in sections 4.4 and 4.5.

4.2 Ordered Muscle Arrangement

4.2.1 Introduction

Given appropriate surface cues, isolated mammalian muscle cells can be induced to assemble into customized 2D muscle pattern on a substrate of choice (Feinberg et al. 2007; Kane et al. 1999). The process and validation of accurate recapitulation, and customized variation, of jellyfish muscle arrangement using micropatterned cardiomyocytes is detailed in the following.

4.2.2 Methods

4.2.2.1 Medusoid Fabrication

The meduosid body was made from a monolayer of engineered cardiac muscle growing on top of a thin film of polydimethylsiloxane (PDMS), a transparent silicone elastomer approximating the elastic properties of jellyfish mesoglea.

Building muscle-powered medusoid constructs involved PDMS film fabrication by spin-coating, PDMS surface modification by microcontact printing to apply extracellular matrix patterns that guide muscle alignment, seeding cardiomyocytes and maintaining the maturing tissue in cell culture, and releasing of the medusoids into the bath for evaluation of contractile function. These procedures were adapted from previous studies on building generic types of muscular thin films (Feinberg et al. 2007) (figure 4.1).

First, titanium templates were created by CNC-milling a 100 µm high plateau in the shape of the chosen medusoid body geometry from a circular base. At times, templates were made from acrylic instead, using a CO_2 laser cutting device (VersaLaser VLS3.50 by Universal Laser Systems, Scottsdale AZ, 85260, USA). The templates were cleaned by sonicating for 20 minutes in 95% ethanol and air dried. Next, the templates were spin-coated for 1 minute at 6,000 RPM with poly(N-isopropylacrylamide) (PIPAAm, Polysciences, Inc.,Warrington, PA 18976, USA) at 10% in 1-butanol (w/v). Sylgard 184 (Dow Corning Corporation, Midland, MI 48686, USA) PDMS elastomer was mixed at a 10:1 base to curing agent ratio and allowed to cure for 3.5 hours at room temperature, then spin-coated on top of the PIPAAm coated templates for 1 minute at 4,500 RPM. This resulted in medusoid-shaped PDMS films of ca.22 µm in thickness on top of the casting molds. These medusoid substrates were cured for a minimum of 4 hours at 65°C, followed by surface functionalization. First, the PDMS film surface was oxidized using UV ozone (Model No. 342, Jelight Company Inc., Irvine, CA 92618, USA) in order to increase hydrophilicity and facilitate protein transfer during microcontact printing.

Medusoid-muscle patterned PDMS stamps casted from negatively patterned photoresist silicon wafers (for details see Feinberg et al. 2007) were inked for 2 hours with human fibronectin (Sigma-Aldrich Co. LLC Natick, MA 0176, USA), dissolved at a concentration of 50 μg/mL in deionized water. Freshly oxidized medusoid substrates were place under a dissection scope for microcontact printing. The air-dried stamps were lowered onto the medusoid substrates and gently pushed down to achieve efficient fibronectin transfer. The micropatterned medusoid substrates were then placed into 6-well culture dishes equipped with one custom-made height adapter per well. The height adapter consisted of a snug-fitting acrylic disc featuring four holes holding one medusoid substrate each. Discs and medusoid substrates being of similar height, the overall surface was approximately even, promoting homogeneous cell seeding. Prior to cell seeding the samples were sterilized by 15 minutes exposure to the UV light of the culturing hood. Neonatal rat ventricular cardiomyocytes were isolated from 2-day-old neonatal Sprague-Dawley using published methods (Feinberg et al. 2007; Alford et al. 2010). All procedures were approved by the Harvard Animal Care and Use Committee. Cells were seeded at a density of 1 million cells per well of a 6-well dish. Standard culture media were used (M199 culture medium supplemented with 0.1 mM MEM nonessential amino acids, 10% heat-inactivated fetal bovine serum, 10 mM HEPES, 3.5 g/L glucose, 2mM L-glutamine, 2 mg/L vitamin B-12, and 50 units/mL penicillin). Samples were incubated under standard conditions at 37°C and 5% CO_2. At 6 hours postseeding 50 nM epinephrine (Sigma-Aldrich) was added to the media. At 24 hours postseeding the medium was replaced to remove epinephrine and cellular debris. At 48 hours postseeding the media was exchanged with maintenance media (M199 media supplemented as above but with 2% FBS). At 72 hours post seeding the media was exchanged with maintenance media once again until use at 4 days post seeding. Medusoids were released from their titanium or acrylic molds after 4 days of culture when the cardiomyocytes had formed a confluent 2D tissue. The samples were removed from the incubator and placed into a Petri

dish filled with 37°C normal Tyrode's solution, an extracellular mammalian electrolyte at pH 7.4 suitable for *in vitro* contractility assaying. Tyrode's solution was prepared from powdered formulation (Sigma-Aldrich, SKU T2145) according to supplier's instructions (9.6 g/L in deionized water supplemented with 1 g/L sodium bicarbonate). The solution was allowed to cool below 35°C, so that the temperature-sensitive, sacrificial layer of PIPAAm transitioned from a hydrophobic to a hydrophilic state and began to dissolve. After 5–10 minutes the medusoids could be peeled off from the titanium or acrylic templates using fine forceps. Substrate-bound medusoid muscle tissue used for immunohistochemistry and optical mapping was fabricated by culturing neonatal cardiomyocytes on micropatterned PDMS-coated glass cover slips as described previously (Feinberg et al. 2007). Briefly, glass cover slips were spin-coated with a 20 µm thick layer of PDMS, followed by microcontact printing and cell culture as described above.

4.2.2.2 Histochemistry and Analysis of Muscle Alignment

Cardiac muscle is, like jellyfish muscle, characterized by striated myofibrils allowing for quantitative comparison of sarcomere alignment, and thus degree of order, in native and engineered systems.

Muscle microstructure in both jellyfish and medusoids was determined by histochemistry and immunofluorescence to visualize actin fiber architecture and sarcomere orientation (figure 4.2a,b). Medusoid-patterned myocardial tissues were cultured on PDMS-coated glass cover slips and stained for F-actin fibers and sarcomeric α-actinin as previously described (Feinberg et al. 2007). Briefly, washed samples were fixed for 15 minutes in 4% paraformaldehyde and 2.5% TritonX-100 in PBS at 37°C, followed by 1 hour incubation with 1:200 dilutions of mouse anti-sarcomeric α-actinin monoclonal primary antibody (Sigma-Aldrich). Samples were then washed and concurrently incubated with 1:200 dilutions of DAPI (Sigma-Aldrich), phalloidin conjugated to Alexa-Fluor 488 (Invitrogen, Carlsbad, CA 92008, USA) and goat anti-mouse secondary antibody conju-

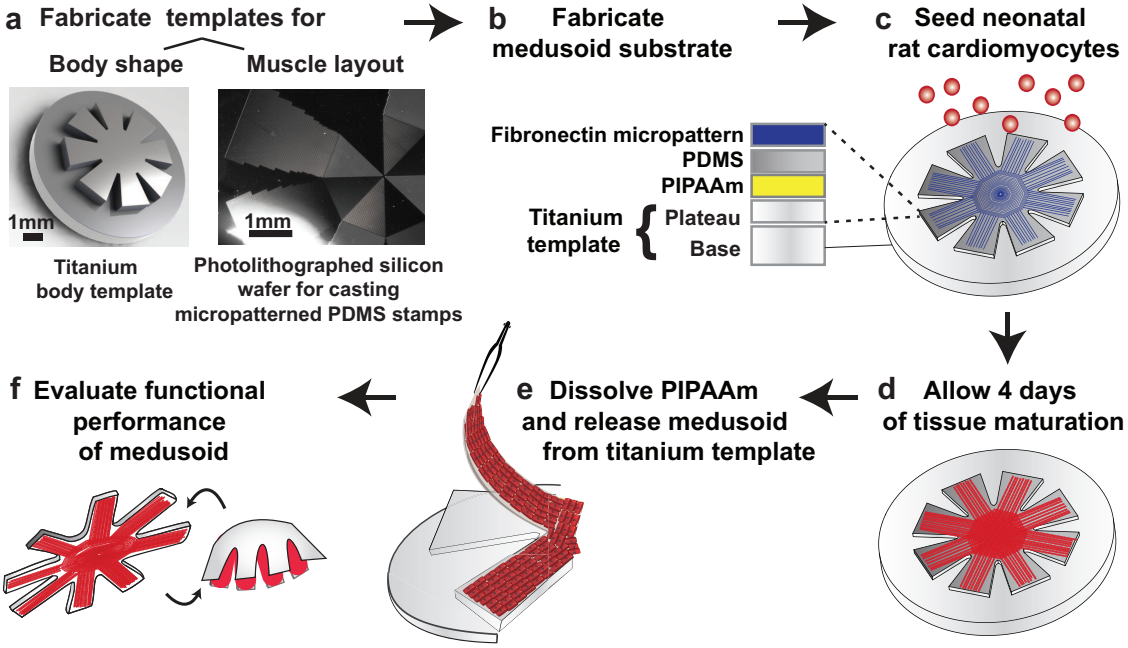

Figure 4.1. Medusoid fabrication

a, Titanium templates and PDMS micropatterned stamps fabricated from photolithographed silicon wafers provided templates for medusoid body shape and muscle layout, respectively. **b**, Medusoid substrates were fabricated by spin-coating the titanium template with PIPAAm for temperature-sensitive adhesion to a PDMS top layer. PDMS stamps were inked with fibronectin, and the fibronectin covering the stamp surface features was transferred to the medusoid PDMS film by contact-printing, resulting in a fibronectin micropattern. This pattern promotes cell adhesion and the formation of anisotropic tissue. **c**, Substrates were seeded with a suspension of freshly isolated neonatal rat cardiomyocytes. **d**, Medusoid substrates were cultured for four days to allow for maturation of the 2D myocardium. **e**, Lowering bath temperatures below 35°C dissolved the layer of PIPAAm, allowing to gently peel off the medusoid from the titanium mold. **f**, The free-floating medusoid was assayed for bell contraction and fluid transfer and compared to jellyfish feeding and swimming.

gated to tetramethylrhodamine for 1 hour at room temperature. Juvenile jellyfish were anaesthetized in 7.5% $MgCl_2$ solution in artificial seawater (1:1) and fixed overnight in 4% paraformaldehyde and 2.5% TritonX-100 in PBS at 4°C. Following fixation the animals were stained overnight at 4°C with 1:250 dilutions of phalloidin conjugated to Alexa-Fluor 488 (Invitrogen) and DAPI (Sigma-Aldrich). Following staining, jellyfish and medusoid samples were mounted to glass slides and imaged on an inverted light microscope (Model DMI 6000B, Leica Microsystems, International Headquarters, Wetzlar, Germany) in epifluorescence using a Coolsnap HQ digital camera (Roper Scientific Inc, Trenton, NJ 08619, USA). Custom-made imaging processing software developed by Adam Feinberg (coauthor of Nawroth et al. 2012) was used to quantify actin fiber alignments (Bray et al. 2008). The code was adapted from biometric fingerprint algorithms (Peter Kovesi, School of Computer Science & Software Engineering, University of Western Australia) and implemented in MATLAB (The MathWorks Inc., Natick, MA 01760, USA). Briefly, intensity images of actin fiber stains (figure 4.2c) were normalized and thresholded to create a binary mask blocking actin-free areas (figure 4.2d). From the masked image intensities a field of orientation vectors was calculated that "flow" tangential to the edges (like velocity vectors along streamlines) and thus correspond to fiber orientation (figure 4.2e). Dominant orientation angles were visualized through the histogram of orientation vector angles (figure 4.2f). In order to quantify the degree of fiber alignment, a derivation of the orientational order parameter (OOP) developed by Anna Grosberg (coauthor of Nawroth et al. 2012) was employed. The OOP is commonly used to determine the degree of order in anisotropic media such as liquid crystals and polymeric solutions (Hamley 2007) and has also been adapted to quantify cell alignment (Umeno and Ueno 2003). Briefly, for each nonempty pixel i an orientation unit vector $r_i = (r_{i,x}, r_{i,y})$ was constructed that was used to form the pixel orientational tensor

$$T_i = \begin{bmatrix} r_{i,x}, r_{i,x} & r_{i,x}, r_{i,y} \\ r_{i,y}, r_{i,x} & r_{i,y}, r_{i,y} \end{bmatrix}. \tag{4.1}$$

Image orientational tensor T is found by averaging over all pixels,$i = 1..n$, followed by normalization. The largest eigenvalue of T corresponds to the orientational order parameter (OOP) and ranges — since$T$ is normalized — from 0 to 1, the former indicating completely random orientation, the latter reporting perfect alignment of all vectors. The OOPs calculated from field of views of different samples can be assumed to be independent of each other and normally distributed, enabling the use of the paired t-test to compare two populations (i.e., jellyfish and engineered muscle).

4.2.3 Results and Discussion

Employing a standardized micropatterning protocol coupled with quantitative structural analysis enabled the implementation of customized muscle architectures with alignment accuracies comparable to native jellyfish tissue (figure 4.2a, b and f., and fig.3.2c). This anisotropy provides the basis for maximizing force generation along a chosen axis (Shim et al. 2012; Feinberg et al. 2012). In addition to generating directional forces, the muscle layer must also allow for continuous propagation of electrical activation to achieve (quasi-)synchronous contraction across the medusoid body. This is addressed in the following section.

4.3 Synchronous Muscle Activation

4.3.1 Introduction

Micropatterned anisotropic cardiac tissue forms an electromechanical syncytium (Bursac et al. 2002), allowing for the through-conduction of electrical and mechanical impulses

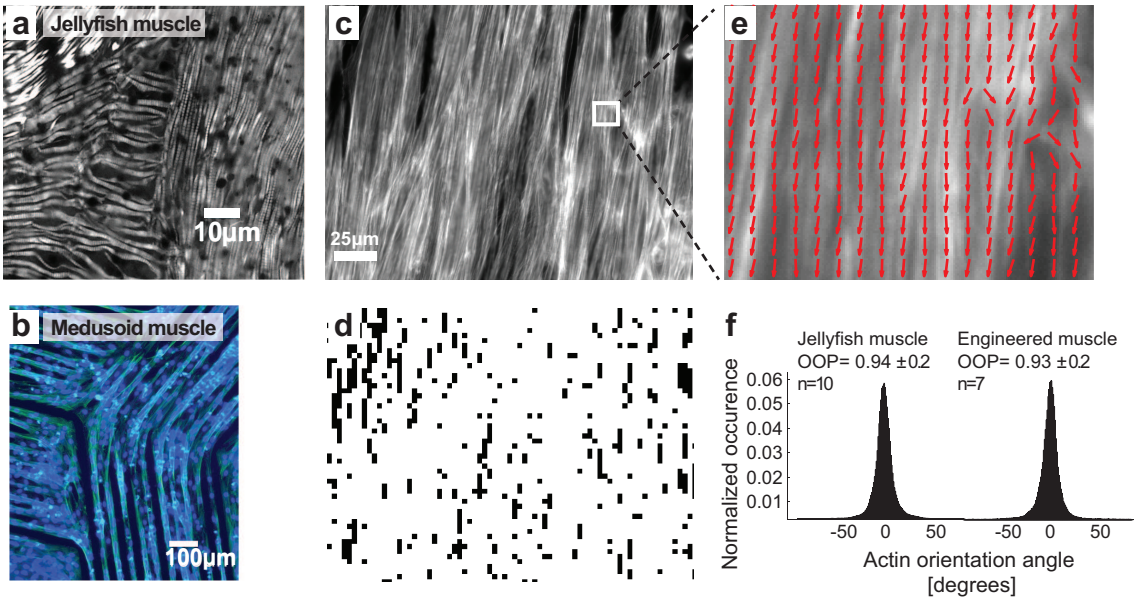

Figure 4.2. Processing steps of quantitative fiber alignment analysis.

a, Close-up on junction of radial and circular muscle in jellyfish. **b**, Close-up on junction of radial and circular muscle in medusoid. Note: This tissue was micropatterned using 20 µm wide lines spaced by 20 µm wide gaps to emphasize longitudinal edges and improve pattern visibility. Final constructs were patterned with 22 µm wide lines separated by 4 µm gaps resulting in confluent anisotropic tissue as seen in **c**, Actin stain intensity image of engineered muscle. **d**, Binary image mask with black regions indicating regions exempted from analysis. **e**, Detail of intensity image overlaid with local vector field showing tangential vector. **f**, Histogram of all orientation vector angles for n jellyfish and engineered muscle samples, peaking at dominant fiber orientation with corresponding orientational order parameter (OOP).

via gap-junctions and cytoskeletal coupling. Tissue at optimal density and alignment exhibits a highly synchronous response to electrical field stimulation, which facilitates quality control and functional assays.

In scyphozoan jellyfish muscle similar mechanical coupling is suggested by the presence of lateral and end-to-end desmosomes joining adjacent muscle fibers (Blanquet and Riordan 1981). Although the muscle is enwrapped by a dense nerve net (Anderson and Schwab 1981; Horridge 1956), little is known about the electrical pathways synchronizing muscle activation (Satterlie 2002). Both jellyfish and medusoid constructs are actuated by a monolayer sheet of muscle which facilitates optical mapping of 2D action potential propagation, allowing for direct comparison of muscle physiology.

4.3.2 Methods

4.3.2.1 Electrical Stimulation Protocol for Free-Swimming Medusoids

In free-swimming medusoids, synchronous contraction was tested and triggered via electrical field stimulation. Field stimulation was accomplished by installing two U-shaped platinum electrodes at opposite walls of a Petri dish containing ca.15 mL of normal Tyrode's solution. A voltage pulse generator (MyoPacer Cell Stimulator by IonOptix, Milton, MA 02186, USA) was used to apply monophasic square pulses (5–10 V, 10 ms duration, maximal current 65 mA) at pacing rates from 0.5 to 2 Hz. (figure 4.3) .

4.3.2.2 Optical Mapping in Jellyfish and Substrate-Bound Medusoids

Optical mapping is the visualization of spatiotemporal changes in membrane potential such as action potential propagation; this is achieved by recording changes in the light emission of a voltage-sensitive membrane stain. Raw optical mapping readout is a scalar field of membrane potentials for each recording time point, allowing to compute velocity vectors of membrane voltage changes across the field of view. Here, optical mapping

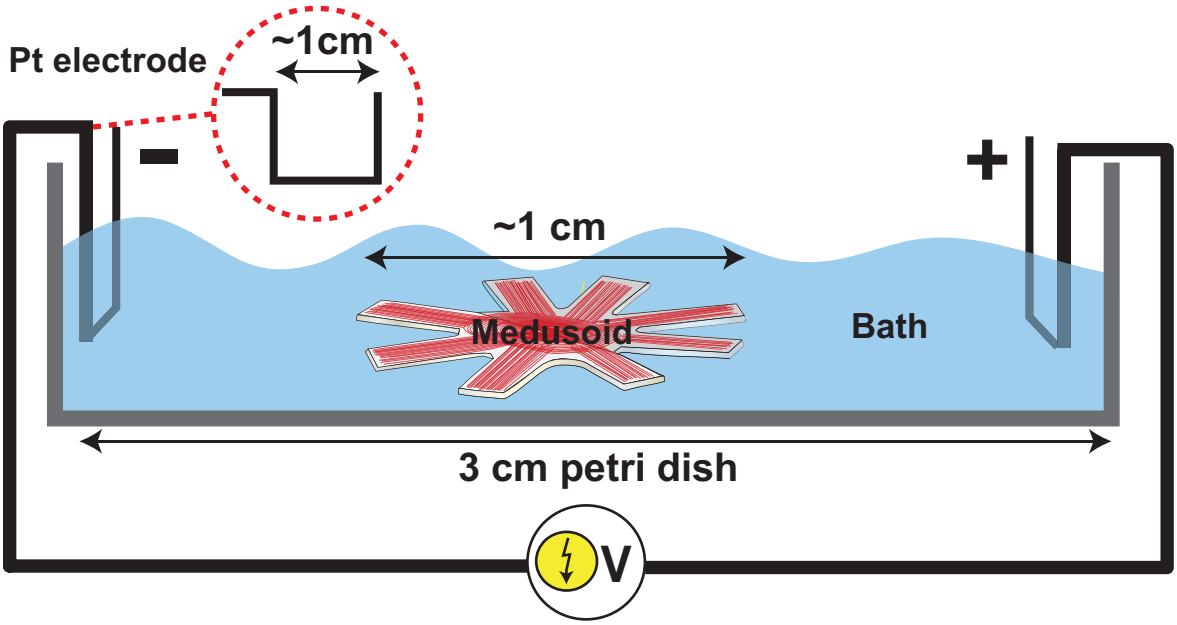

Figure 4.3. Experimental setup for field stimulation of medusoid constructs.

Monophasic square pulses (5 to 10 V, 10 ms duration, maximal current 65 mA) are delivered to the bath (∼10 mL Tyrode's solution at 37°C) by two U-shaped platinum electrodes flanking the construct. Pacing frequency ranged from 0.5 to 2 Hz.

was used to capture the propagation of action potentials across the monolayer of muscle cells powering native jellyfish and engineered medusoid.

Medusoids. PMDS-coated glass cover slips with cardiomycocyte monolayers of medusoid muscle architecture were assayed in a custom-made optical mapping system (figure 4.4f–i) by adapting previously described protocols (Bursac et al. 2002). Briefly, the cultures were incubated for 5 minutes in 8 µM RH-237 voltage-sensitive dye (I_{ex}/ I_{em} in DMSO = ∼550 / ∼800 nm; Invitrogen, Carlsbad, CA 92008, USA) in Tyrode's solution, and washed three times with Tyrode's solution. During recording the tissue was placed in Tyrode's solution containing 10 µm excitation-contraction uncoupler Blebbistatin, thereby minimizing motion artifacts (Fedorov et al. 2007). All solutions were maintained at 35–37°C. A platinum point electrode connected to a Grass S48 stimulator (Grass technologies, West Warwick, RI 02893, USA) was placed ca.1 mm above the culture surface (figure 4.4f) and used to apply point stimuli (5–8 mV, 10 ms duration) at a rate of 2 Hz. Imaging was performed using an inverted microscope (Zeiss Axiovert 200; Carl Zeiss MicroImaging, LLC Thornwood, NY 10594, USA) equipped with a 40× Plan-Neofluar (1.3 NA) oil-immersion objective, a fluorescence light source (Hamamatsu L2422 100 Watt Mercury-Xenon lamp) and a filter cube appropriate for RH237 imaging (Zeiss EX BP530-585, DC FT600, EM LP615). Fluorescence shutter opening and closing was synchronized to the pacing stimulus. Membrane voltage signals, i.e., a shift in the emission spectrum detectable by a change in emission intensity, were optically recorded at 5 kHz using a honeycomb of 124 independent optical fibers array connected to the base of the inverted microscope, each monitoring an approximately circular field of view of 25 µm in diameter (figure 4.4g and h) and each connected to a discrete photodiode transimpedance amplifier. The outputs of the photodiode amplifiers were digitized by a bank of National Instruments (National Instruments Corporation, Austin, TX 78759, USA) differential amplifiers and DAQ cards. The digitized signals were filtered and processed using custom-made software implemented in MATLAB (fig-

ure 4.4i). Activation times, defined as the time point of maximum positive slope of the action potential, served to calculate isochronal maps of activation and velocity vector fields across the field of view monitored by the LED array (Bayly et al. 1998) (figure 4.5d–f).

Jellyfish. Optical mapping in jellyfish (figure 4.4a–e) was performed as in medusoid coverslips except for the following differences: All procedure were performed in artificial seawater at room temperature, freshly prepared from marine salt mix according to manufacturer's recommendations (KENT Marine Sea Salt, 5401 West Oakwood Park Drive, Franklin, WI 53132). After staining with RH237 no excitation-contraction uncoupler was added to the solution since jellyfish swimming muscle proved to be insensitive to all tested uncoupling agents commonly used in cardiac optical mapping studies including Blebbistatin, Cytochalasin D and 2,3-Butanedione monoxime (BDM), as well as skeletal muscle uncoupler Dantrolene sodium. The jellyfish was placed onto a coverslip with its subumbrellar muscle layer facing down towards the LED recording array. To constrain movement, an additional cover slip was placed on top of the jellyfish. In some cases vacuum grease was used as a spacer. Anode and cathode pole of a platinum pacing electrode were placed into excess seawater protruding from either side of the coverslips to apply field stimulation (5–8 mV, 10 ms duration) at a rate of 1 Hz (figure 4.4a). This stimulus reliably led to muscle contraction starting near the pacemaker centers within the lobes (figure 4.4b). Presumably, the electrical stimulus activated the neuronal pacemaker centers which in turn activated adjacent swimming muscle, effectively mimicking point stimulation of the lobe muscle. Due to the muscle contraction the optical signals contained motion artifacts that appeared subsequent to the voltage signal. This difference in relative timing allowed identifying those channels recording from muscle-free extracellular matrix (ECM) and isolating true voltage signals (figure 4.4c,d). Subsequently, the voltage signal was filtered (figure 4.4e) and analyzed as described above to calculate activation times, isochronal maps and velocity vector fields (figure 4.5a–c).

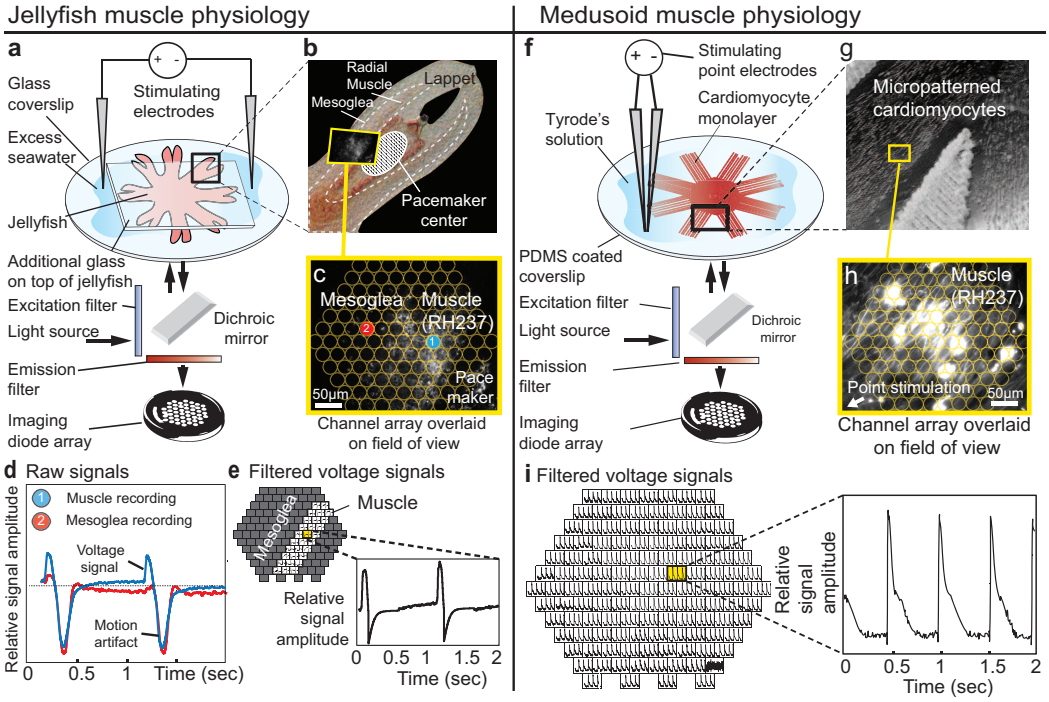

Figure 4.4. Optical mapping setup.

a, Setup of optical mapping system (OMS) for membrane voltage recording in jellyfish muscle stained with RH237. **b**, Close-up on jellyfish lobe with typical field of view (FOV) on RH237-stained radial muscle. **c**, FOV overlaid with LED recording array. The two labeled channels are representative for channels recording from muscle tissue (channel 1, blue) or from mesoglea (channel 2, red). **d**, Recording traces from the two channels marked in (c) illustrate that only muscle recordings contain voltage signals. **e**, Filtered data set only contains channels recording from muscle. **f**, OMS setup for membrane voltage recording in medusoid muscle (anisotropic monolayer of cardiomycoytes). **g**, Close-up on medusoid micropatterned muscle. **h**, Typical FOV of RH237-stained muscle tissue overlaid with LED recording array. **i**, Filtered voltage signal and exemplary trace recorded by single channel.

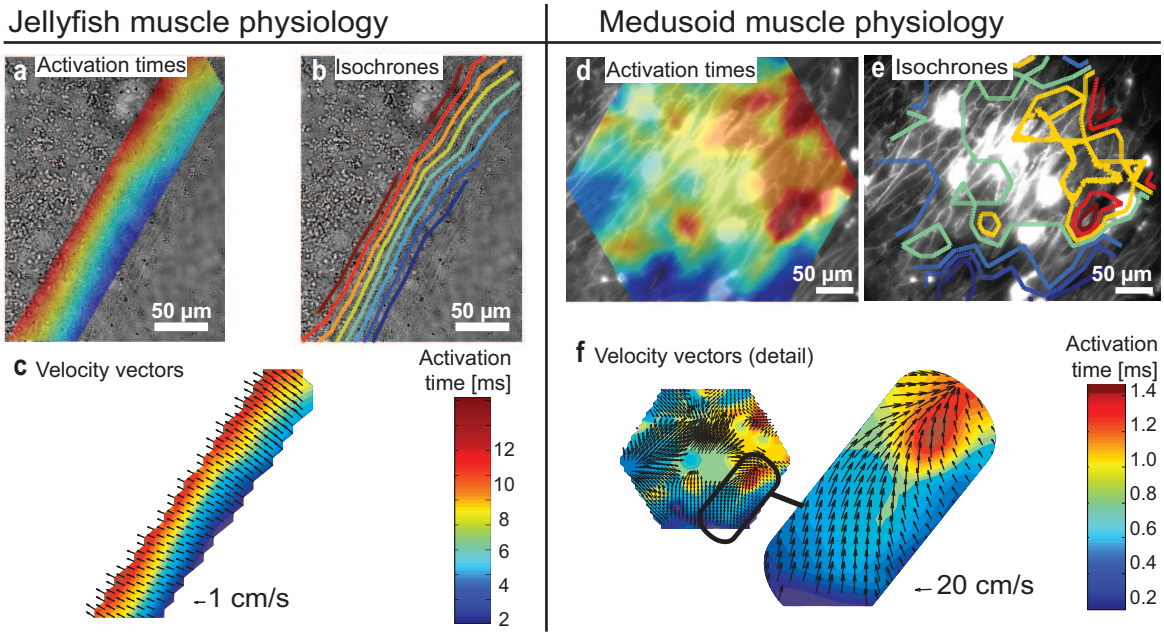

Figure 4.5. Optical mapping results confirm continuous action potential propagation in medusoid and jellyfish striated muscle.

a–**c**, Activation times and velocity vectors calculated from filtered data set in figure 4.4e illustrate spread of continuous wave front activating the jellyfish muscle. Mean conduction velocity: 1±0.35 cm/s; n=13 FOVs (from 3 animals). **d**–**f**, Activation times and velocity vectors calculated from filtered data set in figure 4.4i illustrate spread of continuous wave front activating the medusoid muscle. Mean conduction velocity: longitudinal, 27±4 cm/s, transverse, 9±1 cm/s; n=4 FOVs (from 2 medusoid constructs).

4.3.3 Results and Discussion

Electrical field stimulation of medusoid constructs usings stimulation settings of 1 Hz, 2.5 V/cm, 10 ms pulse width resulted in reliable pacing and synchronized contraction of constructs that, when not externally stimulated, exhibited spontaneous unsynchronized lappet contractions (supplementary movie 9, also see figure 3.3c,d). For comparison, note that native jellyfish contraction occurs in bursts of 2–3 Hz for animals of ca.1 cm diameter as used in this study; frequency goes down at larger sizes.

Optical mapping in a field of view of approximately 400×400 µm confirmed continuous wave front propagation in both jellyfish muscle and the engineered cardiac tissue of medusoids (figure 4.5). These similarities in electrophysiological properties suggest that engineered cardiac tissue is suitable for achieving jellyfish-like lappet contraction, despite recent findings that striated muscle in jellyfish may have evolved separately from other animal muscle cells (Steinmetz et al. 2012). Indeed, jellyfish and free-swimming medusoids exhibit very similar stroke kinematics as presented in chapter 3 (figure3.3a). It is noteworthy, however, that despite the macroscopic similarity of jellyfish and meduosid contraction, local myoid conduction velocity in jellyfish (1 cm/s) appeared to be one order of magnitude slower than local conduction velocity in the cardiomyocyte monolayer of medusoids (10–25 cm/s). Interestingly, the conduction velocity of muscle-activating electrical signals in hydrozoan jellyfish (distantly related to scyphozoan jellyfish) has been shown to vary from 5 to 50 cm/s, depending on whether the signal is constrained to travel within the muscle layer or is free to also move through adjacent bell tissue, respectively (Mackie and Passano 1968). These findings and the optical mapping data suggest the presence of both myoid and non-myoid electrical pathways innervating the jellyfish muscle layer in parallel. Indeed, recent research in hydrozoans indicates that synchronized bell contraction is achieved through a two-layered conduction system consisting of a fast, global component — the neuronal motor network — that activates the second component, patches of muscle cells within which the electrical signal spreads

locally, and potentially more slowly, via gap junctions (Satterlie 2008). These results demonstrate that biomimic and bioinspired devices need not necessarily copy all components of a model system to achieve a similar function. In particular, for the purpose of mimicking global jellyfish muscle physiology, there was no need to distinguish between gap junction mediated myoid conduction, synaptic input from neurons, or a mixture of both, since activation of the cardiomyocyte syncytium resulted in the same contraction kinematics.

4.4 Biomimetic Muscle Design

4.4.1 Introduction

Initial design of medusoid muscle architecture and body shape followed a biomimetic approach, copying the morphology of juvenile medusae featuring a circular disc with short lobes, reduced radial muscles and a comparatively narrow band of ring musculature (figure 4.6a–c). Muscle activation was expected to generate circumferential compression and contract the disc into a conical bell shape. However, in contrast to native jellyfish, medusoids with biomimetic design failed to notably deform the disc, indicating a mismatch of muscle force and substrate compliance. A brief review of the physical laws governing the deformation of thin plates elucidates this outcome. A flat, isotropic and homogeneous thin plate like the silicone disc that constitutes the medusoid's body has two primary modes of deformation in response to compressive forces: out-of-plane bending and in-plane compression. The energy needed for compression, a form of stretching, scales linearly with plate thickness while bending energy is proportional to cubed thickness. For thin substrates, the stretching energy term thus dominates, and compression strains are reduced by either buckling, wrinkling or crumpling, all of which generate high curvatures, reflecting the plate's preference for bending (Marder et al. 2007; Holmes et al. 2008). Hence, thin plates that are compressed generate a multitude of radial folds like

a closing umbrella (Bella and Kohn 2012; Hure et al. 2012; King et al. 2012) instead of stretching into a smooth sphere. [1] However, unlike the plates in these studies, the medusoids are not clamped at their outer edge, which changes boundary conditions and the stress field. Indeed, as noted, medusoids with biomimetic design failed to generate wrinkles and fold the silicone disc into a bell. More specifically, deformation of the disc was limited to two circumferential buckles, forming a very shallow cone (figure 4.6d,e and supplementary movie 2). This is reminiscent of the conical surface formed by a planar, incompressible disc forced into a cylindrical frame, such as a circular sheet of paper on top of a glass, by applying a centered normal force (figure 4.6f). Cerda and Mahadeva (2005) developed a mathematical model of this phenomenon which they called the "puckered cone." In both medusoid and puckered cone, the thin plate buckles once or twice out of plane to attain the smaller diameter imposed by circumferential contraction, or by the cylindrical frame, respectively. As detailed in the following, applying the puckered cone model to the biomimetic medusoid (figure 4.6g-i) helps analyzing its failure to bend into a pronounced cone.

4.4.2 Methods

In the puckered cone, the application of a central transverse force F_C generates a normal force F_N along the line of contact between disc and cylinder and pushes the center of the disc into the cylindrical frame. A normalized measure of vertical displacement is given by $\epsilon = d/R$, where d is the height of the cone and R is a characteristic radius (figure 4.6i). In addition, as ϵ is increasing, the disc forms radial buckles characterized by their width and curvature. Displacement ϵ reaches equilibrium when the stresses generated by the elastic deformation of the disc balance F_C. Similarly, the radially compressive

[1] Only isometric transformations, which preserve the Gaussian curvature, maintain areas and angles and thus do not stretch the surface. For example, a sheet can be rolled into a cylinder without stretching since both surfaces have a Gaussian curvature of zero, but neither can be isometrically transformed into a spherical surface which has a Gaussian curvature of $1/\mathrm{R}^2$.

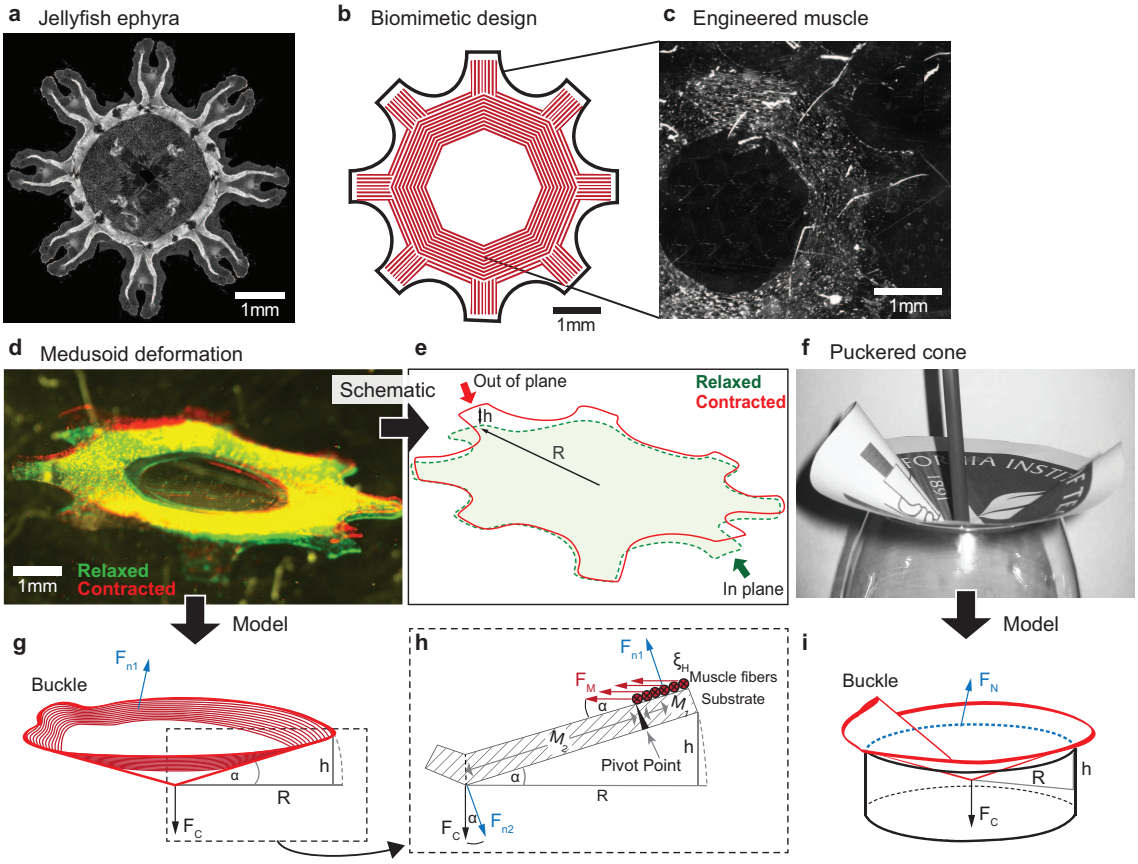

Figure 4.6. Failure analysis of biomimetic medusoid.

a, Muscle architecture in *A. aurita* jellyfish ephyra with radial and circular fiber orientations. White: actin stain of muscle fibers. Mosaic image was created by rotating image of single stained lappet to eight positions around central axis. b, Biomimetic medusoid body and muscle design, and c, tissue-engineered implementation (bright field image). d, e, Medusoid in relaxed state (green) and contracted state (red). The overlay illustrates maximal out-of-plane deformation, reminiscent of the radial buckles exhibited by the f, Puckered cone formed by pushing a pencil down the center of a paper disc that lies on top of a glass. g, h, Model of medusoid deformation with parameters and forces adapted from i, Model of puckered-cone by Cerda and Mahadeva (2005). See main text for details.

muscle force F_M in the biomimetic medusoid results in a central transverse force F_C which displaces the center vertically by a factor $\epsilon = d/R$ until balanced by opposing forces generated by elastic deformation (figure 4.6g,h).

4.4.2.1 Forces Required for Elastic Deformation

Assuming only isometric transformations of the disc, i.e., not permitting stretching, applying F_C results in central displacement and the formation of one or maximally two radial buckles (Cerda and Mahadevan 2005). The equilibrium state is reached when applied and opposing forces and moments are balanced, storing the applied work in the elastic bending energy of the cone, U, which thus provides a relation between applied force, the variation of elastic energy, and geometry. The applied force can be related to ϵ and disc dimensions with $F_C = \frac{1}{R}\frac{\delta U}{\delta \epsilon}$. For small displacements with $\epsilon \leq 0.1$, the system acts like a linear spring such that the applied force is proportional to displacement, $F_C \sim \epsilon$. Cerda and Mahadeva compute the normalized $\widehat{F_C}$ as a function of ϵ for the case of one or two buckles, which represent the deformation of lowest elastic energy. From this, F_C can be expressed by

$$F_C = log(\frac{R}{R*})\widehat{F_C}R^{-1}B \tag{4.2}$$

and computed for the specific material properties and geometry of the medusoid where R = 4000 μm, $R*$= 1200 μm is the radius of the central region responding to F_C by local stretching[2], and $B = Eh^3/12(1-\sigma^2)$ is the bending stiffness where E = 1.5 MPa is the Young modulus and h= 25 μm is the thickness of the PDMS sheet. Given $\epsilon \leq 0.1$, F_C for these parameters is on the order of 10^{-5}N.

[2]Empirically determined to be ca.20% of R (Cerda and Mahadeva, 2005)

4.4.2.2 Muscle-Generated Forces

The muscle band is assumed to consist of n individual circular muscle rings of single cell thickness t and radius r_i, $1, ..., n$, which shortens by a factor of $cos(\alpha)$ upon contraction, whereα is $arcsin(\epsilon)$. Assuming even spacing between individual muscle fibers, the average radius is thus $r(\alpha) = \frac{1}{n}\sum_{i=1}^{n} r_i cos(\alpha)$. The modified Young-Laplace law relates circumferential "hoop" stress ξ_H of a muscle ring to radially compressive stress ξ_M (Zhang et al. 2011):

$$\xi_M = (2 + tr^{-1})\xi_H tr^{-1}. \tag{4.3}$$

The average radial force per muscle ring is then

$$F_M = 2\pi t \xi_M. \tag{4.4}$$

Even for constant muscle stress, F_M is thus a function of α, and therefore of ϵ. In addition, according to the length-tension relationship of striated muscle, muscle-generated stress decreases as the muscle shortens (Gordon et al. 1966). However, for small deflections with $\epsilon \leq 0.1$, $cos(\alpha) \approx 1$ and $r(\alpha) = r(0)$, and muscle shortening is $\leq 5\%$, resulting in quasi-isometric conditions. Contracting medusoids fall into this regime, with $\epsilon \leq 0.08$ estimated from experimental data (figure 4.6d and e).

The normal component of F_M is given by $F_{n1} = F_M sin(\alpha)$. Since the muscle layer is raised relative to the substrate, F_{n1} acts around a pivot point and generates a lever force $F_{n2} = F_{n1}\frac{M_1}{M_2}$ at the center of the cone, where M_1 and M_2 denote the lengths of the levers. The central transverse force component is $F_C = F_{n2} cos(\alpha)$ (figure 4.6h). Hence, radial muscle force F_M relates to central transverse force F_C with

$$F_C = \frac{1}{2} F_M \frac{M_1}{M_2} sin(2\arctan(\epsilon)) \tag{4.5}$$

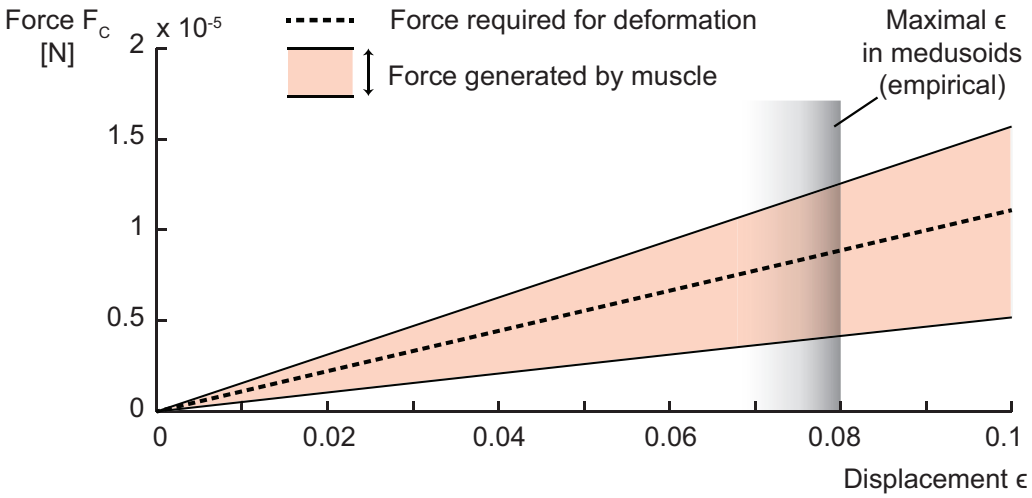

Figure 4.7. Model of required and available force for small deflections of medusoid body. These curves are based on parameter estimates and serve for qualitative comparison. In particular, for small deflections, muscle-generated forces (solid line) are proportional to, and on the same order of magnitude as the forces required for elastic deformation (dashed line).

Given isometric muscle stresses of of 5–15 kPa (Alford et al. 2010), $n = 250$ parallel circular muscle rings with average radius $r = 3500$ μm and thickness $t = 10$ μm, and $\epsilon \leq 0.08$, F_C is on the order of 10^{-5} N.

4.4.3 Results and Discussion

For small deflections, muscle-generated forces are proportional to, and roughly on the same order of magnitude as the forces required for disc deformation (figure 4.7). These result are consistent with the finding that the average biomimetic medusoid was capable of generating a central displacement of 0.4 mm, corresponding to $\epsilon \leq 0.08$. Here, maximal ϵ represents maximal deflection anywhere along the rim of the disc because ϵ in medusoids was too small to distinguish between buckled and nonbuckled regions. In the original model by Cerda and Mahadeva, ϵ refers to the nonbuckled region of the disc. This means that the actual ϵ achieved by medusoids might be even smaller but this does not alter the interpretation of the model.

Further, this model relies on the assumption that $\epsilon \leq 0.1$ and thus does not allow probing the case of greater deformation. However, with increasingϵ the muscle needs to shorten further, leaving the regime of isometric contraction such that stress generation declines rapidly (Gordon 1966). Shortening of cardiac muscle by 10%, which corresponds to $\epsilon = 0.4$ in our model, results in a decline in generated stresses of more than 30% (Holubarsch et al. 1998; Jewell and Porter 2008). In contrast, the forces required to bend the cone continue to increase with ϵ until $\epsilon \approx 0.32$ (Cerda and Mahadevan 2005), suggesting that muscle-generated forces will be insufficient to achieve such deformation. This qualitative prediction is consistent with the observation that biomimetic medusoids never contracted to $\epsilon > 0.1$.

The question then arises why native jellyfish medusa are capable of contracting into a bell given this apparently unfavorable design. As discussed in the model above, the silicone polymer used in medusoids is effectively incompressible and of homogeneous stiffness, leaving buckling as the only — and energetically expensive — option for deformation. Jellyfish mesoglea, on the other hand, contains an anisotropic architecture of extracellular fibers that create stiff ridges separated by soft tissue, corresponding to hinges and bendable zones, which enable radial folding during both bell contraction and relaxation (figure 4.8) (Gladfelter 1972; Megill 2002; Gambini et al. 2012).

The experimental and modeling results presented in this section illustrate the mechanical constraints imposed by fabricating the medusoid body from PDMS. Instead of searching for alternative materials, which would potentially affect all fabrication and tissue-culturing procedures, medusoid geometry and muscle architecture were adapted to reduce bending stresses and fully exploit muscle stresses, as discussed in the following section.

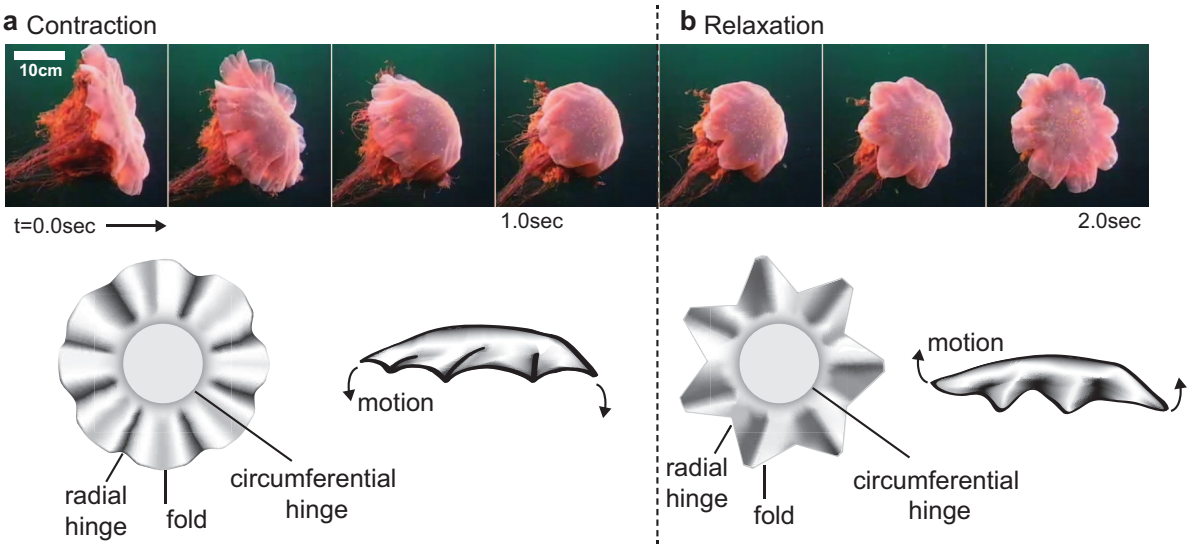

Figure 4.8. Stroke cycle of adult Lion's Mane scyphomedusa (*Cyanea capillata*) illustrates the anisotropic properties of the mesoglea that facilitate folding.

a, During the contraction phase, or power stroke, the saucer-shaped body is smoothly folded along stiff hinges such that a spherical bell is formed while pushing water backwards. **b**, During the relaxation phase, or recovery stroke, the bell unfolds while reducing drag by sharply bending around the hinges. Photographic images (top row) were extracted from raw video footage (FootageBank HD) and interpreted (bottom row) according to Gladfelter (1972).

4.5 Rational Muscle Design

4.5.1 Introduction

The biomimetic medusoid's design and failed response was simple enough to analyze and qualitatively explain the phenomenon. For elucidating and — more importantly — predicting more complex conformational changes of engineered contractile tissues, computational tools need to be established that account for cell dynamics, nonlinear material responses, and customized geometries. The author was part of a collaborative effort to develop such a tool for designing PDMS films powered by spatially aligned cardiac myocytes, with the immediate application of improving the design of the medusoid. The resulting 3D phenomenological constitutive finite element (FE) model of cardiac muscular thin films (cMTFs) is reported in Shim et al. (2012).

4.5.2 Methods

Constitutive Model of Muscle-Powered Thin Films

Design parameters to be explored include muscle architecture, contraction frequency and bending stiffness of the film. The FE model of cMTF developed by Shim et al. captures both contraction and relaxation of the cardiac muscle cells as well as their passive properties such as the prestretch, a deformation of the muscle cell during maturation which affects force generation. Model parameters were chosen to match experimental results in cMTFs, often spanning a range of values to account for the variation in mechanical properties observed *in vitro*. Based on the model predictions and empirical data it became apparent that the most favorable configuration would be that of a thin cantilever where a film strip is bent along its long axis through the contraction of a monolayer of longitudinally aligned muscle cells (figure 4.9a,b; Shim et al. 2012). The effect of parameters such as contraction frequency and film thickness on maximal bending cur-

vature were investigated (figure 4.9c,d). In particular, the model predicts that a 22 µm thick film of ca.2 mm length with a Young modulus of 1.5 MPa (regular PDMS) and activated at a frequency of 1-2 Hz, achieves bending angles of about 90° (supplementary movie 10), which is comparable to jellyfish lappet contraction (supplementary movie 1). This corresponds to a curvature of ca.0.8 mm^{-1}, implying that the cMTFs still operate at quasi-isometric contraction regimes (Alford et al. 2010), thus maintaining maximal force generation which is of interest when dealing with the added resistances due to fluid interactions.

Lobed Medusoid Design

We therefore developed a rational medusoid design featuring pronounced radial lappets actuated by radial muscles, such that a bell would be formed by inward bending of the lappets, not unlike a flower closes its petals. Since maximal conduction velocity occurs along the longitudinal axis of anisotropic myocardium, a central ring muscle was installed to facilitate lappet synchronization by providing a rapid circumferential conduction pathway (figure 4.9e). This design is similar to early stage jellyfish ephyrae. In contrast to native jellyfish, however, the medusoid body was covered entirely with muscle to maximize stress generation, which scales with cross-sectional area, and facilitate electrical synchronization.

4.5.3 Results and Discussion

Medusoids built according to this lobed design exhibit robust bell contraction, with 90° lappet bending at 1–2 Hz pacing rates (figure 4.9f). However, despite these vigorous contractions, the lobed medusoids moved barely forward (supplementary movie 11). There are at least two potential causes for this result. Either, the kinematics of lappet contraction could be unsuitable for generating net thrust, i.e., fluid could be moved back and forth symmetrically without a net rearward direction. Alternatively, or in addition,

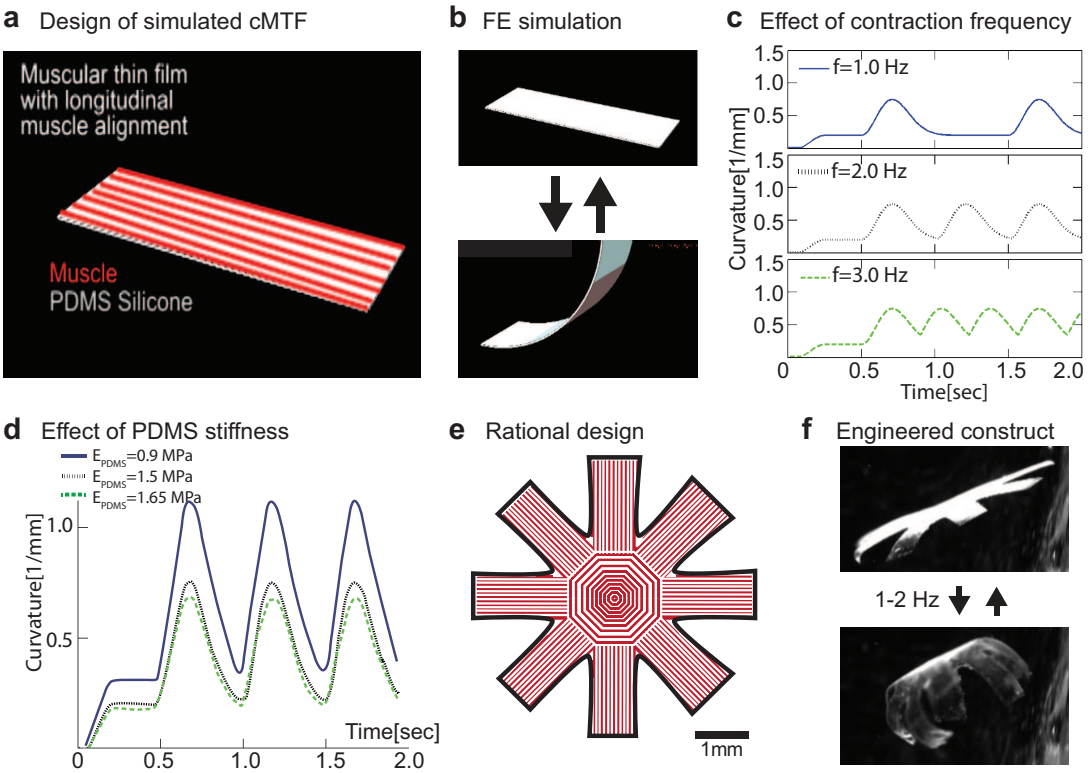

Figure 4.9. Lobed medusoid design guided by finite element simulation.

a, Example of simulated cardiac muscular thin film (cMTF) featuring a PDMS film strip with longitudinal muscle alignment. Other designs included diagonal muscle alignments. **b**, Simulated contraction of cMTF using a finite element model. **c**, Effect of contraction frequency on film curvature. **d**, Effect of PDMS stiffness (Young's modulus) on film curvature. **e**, Rational meduosid design with radial lappet and muscle layout. The central circular muscle facilitates through-conduction. **f**, Engineered implementation exhibits desired 90° lappet bending at 1–2 Hz pacing rates (see also supplementary movie 3). Panels a–d are adapted from originals courteously provided by Jongmin Shim.

body-fluid interactions could be inefficient such that lappets sieve the water rather than transport it. These two options will be investigated in the following three chapters.

Chapter 5

Design Principle Stroke Kinematics: Stroke Parameters Contributing to Thrust Generation, and Their Implementation *in vitro*

This chapter expands on the methods and supplementary information of Nawroth et. al. (2012) reproduced in chapter 3. The thesis author has collected all data and composed all graphics and text unless noted otherwise.

5.1 Introduction

Locomotion in jellyfish medusae is unsteady and consists of a periodic pulsation cycle (Daniel 1985 1983). The contraction phase expels water and produces forward thrust, whereas the relaxation phase restores the original bell shape and generates rearward thrust. Note that traditionally, it was thought the forces generated by the jellyfish muscle had to equal thrust force; Dabiri et al. (2005) however found that in scyphozoan jellyfish like *Aurelia aurita*, constructive interference of vortices produced during contraction and subsequent relaxation reduce these force requirements, enabling the occurrence of large oblate jellyfish operating with only a single layer of muscle (Dabiri et al. 2007).

Intuitively, contraction and relaxation phase must differ in parameters relevant to

thrust generation in order to generate net forward thrust. Formally, net forward thrust is equal to the rate of momentum efflux during the contraction phase, minus the rate of momentum influx during the relaxation phase. Daniel (1983 and 1985) investigated in detail the thrust produced by either power or recovery stroke of a medusa, and the balancing fluid forces that act on it:

$$Thrust = D + A + I, \tag{5.1}$$

where D is drag, A are forces due to accelerating the fluid around the animal (acceleration reaction), and I are forces required to overcome inertia. Briefly, drag D is proportional to animal dimensions and instantaneous velocity:

$$D = \frac{1}{2} C_D \rho S u^2, \tag{5.2}$$

where ρ is the fluid density, C_D is the drag factor, and S is the projected area of the medusa facing the flow. Acceleration reaction A is proportional to animal geometry and changes in velocity:

$$A = \alpha \rho V \frac{du}{dt}, \tag{5.3}$$

where α is the dimensionless added mass coefficient, a factor which takes into account the effect of shape on the acceleration of fluid around an object, V is the volume of the animal, and u is the flow velocity; and I is the force required to accelerate the mass of the animal itself:

$$I = \rho V \frac{du}{dt} \tag{5.4}$$

Daniel (1983 and 1985) evaluated the relative importance of these fluid forces in a mathematical model and found that while the acceleration reaction represents the largest force component during swimming initiation, drag dominates during continuous medusa

swimming. Further, assuming that the projected area of the medusa facing the flow is comparable during power and recovery stroke, the model predicts that no net thrust is generated for symmetric stroke kinematics, i.e., for equal durations of recovery and power stroke. Conversely, greatest average velocity in continuously swimming medusae is predicted for a ratio of about 2.5:1 for the duration of recovery versus power stroke. This mainly results from the fact that a slower recovery stroke generates less drag and thus less rearward thrust relative to the forward thrust of a faster power stroke (equation 5.2).

In summary, an asymmetric stroke cycle where relaxation takes longer than contraction is important for generating net forward thrust in continuously swimming medusae and, in extension, in continuously paced medusoids. The finite element simulation presented in section 4.5 indicates that such asymmetry might occur naturally in contracting cardiac muscular thin films (c.f. figure 4.9c,d). In the following, this is verified in medusoid contracts and compared to stroke kinematics of native jellyfish ephyrae.

5.2 Methods

5.2.1 Lappet Kinematics

Analysis of medusoid and jellyfish lappet kinematics was performed by tracking the frame-to-frame displacement with image processing software. First, bright field AVI video recordings of free-swimming medusoids and jellyfish were opened as image stacks in ImageJ (National Institutes of Health; Abramoff et al. 2004) to manually label the distal tips of a chosen set of lappets as well as a reference point on the bell within each frame. The centroids of the labeled tips were tracked using an in-house MATLAB software to derive relative displacement of the lappets relative to the central reference point, allowing to express angular lappet speed as a function of time (figure 5.1a–d, supplementary movie 12). Note the sign convention: Angular velocity is positive during

contraction and negative during relaxation phase. For each lappet, stroke asymmetry is defined as the maximal lappet contraction velocity divided by absolute maximal lappet relaxation velocity. Relative contraction asymmetry within each set of labeled lappets is expressed as the temporal variance in reaching maximal contraction velocity (figure 5.1e–g).

5.2.2 Statistical Analysis

Lappet kinematics data did not follow a normal (or otherwise obvious) statistical distribution, and sample sizes were relatively small ($n < 10$). Therefore, non-parametric methods were chosen for both data analysis and data representation (figure 5.1f and g). Briefly, the data sets are presented in a so-called boxplot diagram which gives a graphical summary of the data distribution in a non-parametric form, i.e., without making assumptions about an underlying statistical distribution. In particular, since the data do not follow a normal distribution, mean and standard deviation have little relevance for representing and comparing data sets. Instead, the boxplot summarizes each data set in five numbers: median (bull's eye), 25th and 75th percentile (upper and lower edge of rectangle, respectively), and the smallest and the greatest observation (upper and lower end of whiskers, respectively). Note: The 25th percentile is the value below which 25% of the observations may be found; the 75th percentile is the value below which 75% of the observations may be found. Thus, the rectangle spans 50% of the observations. Consistent with the boxplot representation, a nonparametric statistical test was employed for examining the sample sets pairwise for statistically significant differences in performance/kinematics without making any assumptions about underlying statistical distributions. We used the Wilcoxon rank-sum test, synonymously called Mann–Whitney U test or Mann–Whitney–Wilcoxon (MWW) test, to determine the P-values noted in the plots. Here, the P-values denote the probability of obtaining two data distributions that are at least as different as the ones that were actually observed

if the two sample sets were equal in their performances/kinematics (null hypothesis). Asterisks denote a statistically significant difference, i.e., $P < \alpha = 0.05$, where α is the significance level.

5.3 Results and Discussions

Lappet kinematics of jellyfish ephyrae and medusoids are optically similar, revealing a clear asymmetry in the stroke cycle as the relaxation phase takes longer than the power stroke (figure 5.1b,c). Whereas individual lappet kinematics are more varied in medusoids than in jellyfish, the average traces are comparable (figure 5.1d). In particular, median stroke asymmetry was 2.2 in medusoids, corresponding to the factor by which the recovery period exceeds the contraction period. Native jellyfish demonstrated greater median stroke asymmetry but the statistical difference was not significant (p-value = 0.7, Wilcoxon rank sum test, n=4 lobe pairs each; figure 5.1f). Lappets belonging to the same animal or construct contracted in comparable synchrony, i.e., the ratio of maximal lappet velocities during power and recovery stroke did not differ significantly in jellyfish and medusoids (p-value = 0.7, Wilcoxon rank sum test, n=9 lobes each; figure 5.1g).

In summary, the average recovery stroke in medusoids takes least twice as long as the power stroke, which is comparable to the native jellyfish, and the lappets are well coordinated. These results indicate that medusoid lappet kinematics are suitable for generating forward thrust, suggesting that the poor swimming performance of the original lobed medusoid design (supplementary movie 11) might be due to inefficient interaction of the body geometry with the surrounding fluid. The following two chapters confirm this hypothesis, and present the design solution.

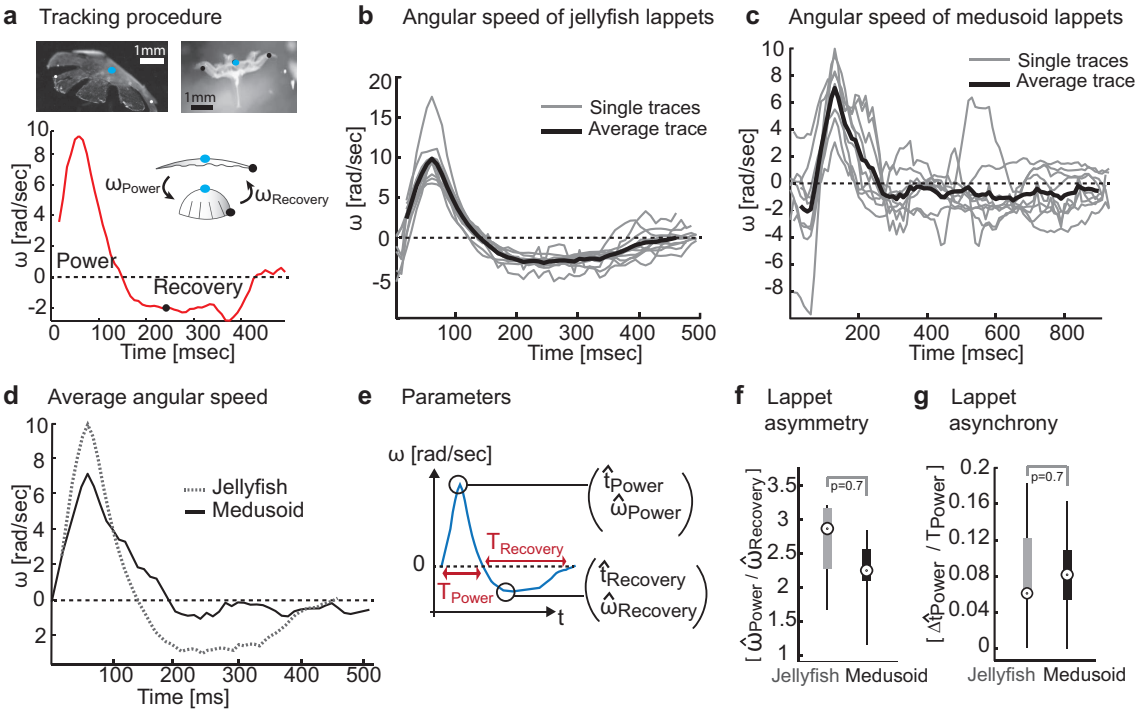

Figure 5.1. Lappet kinematics.

a, Tracking procedure. Top: Examples of labeled medusoid and jellyfish ephyra with central reference dot (blue) and distal tracking dots (white or black). Bottom: Example trace of angular velocity of tracked jellyfish lappet with respect to reference point. **b**, Single and average angular velocity traces of 9 jellyfish lappets throughout the stroke cycle. **c**, Single and average angular velocity traces of 9 medusoid lappets throughout the stroke cycle. **d**, Average trace of angular speed in juvenile jellyfish and medusoids (n=9 lappets each) throughout the stroke cycle. **e**, Characteristic parameters of stroke cycle. T_{Power}, $T_{Recovery}$, duration of power and recovery stroke; $(\hat{t}_{Power}, \hat{\omega}_{Power})$, coordinate of peak velocity of power stroke; $(\hat{t}_{Recovery}, \hat{\omega}_{Recovery})$, coordinate of peak velocity of recovery stroke. **f**, Stroke asymmetry expressed by the ratio of maximal lappet velocities during power and recovery stroke. **g**, Relative asynchrony of lappet contraction expressed by the normalized difference between time points of peak power stroke velocities in pairs of lappets, $\Delta\hat{t}_{Power}$. Boxplot representation: Bull's eyes, median; lower edge of box, 25th percentile; upper edge of box, 75th percentile; whiskers, extreme data points.

Chapter 6

Design Principle Fluid Dynamics: Phenotypic Plasticity Reveals Geometric Parameters Relevant to Propulsive Efficiency

6.1 Phenotypic Plasticity and Ontogeny as Heralds of Design Principles

> "We maintain that it is not particular genes (with minor exceptions), nor the discrete phenotypes produced in different environments, that are the objects of selection: it is the capacity of organisms to deal with environmental contingency that is the focus of selective forces in nature." (Schlichting and Pigliucci 1998)

The study of phenotypic plasticity, i.e., the ability of organisms with the same genotype to develop alternate, but reproducible, phenotypes under varying environmental conditions has a long tradition within biology (Schlichting and Pigliucci 1998). It remains debated whether phenotypic plasticity constitutes an adaptation or rather an inevitable consequence of the dynamics of biochemical and biophysical reactions; however, a multitude of examples document functional advantages gained by changes in design. Among

the most striking are differences in leaf morphology and physiology exhibited by many plants as a function of light exposure that adjust photosynthesis (Wyka et al. 2007), and the water flea's formation of a defensive carapace in response to predatory pressure (Riessen and Trevett-Smith 2009). This suggests that, in some cases, phenotypic plasticity highlights design parameters contributing to a particular function. Similarly, design changes exhibited during ontogeny can represent structure-function relationships adapting to increased body dimensions and associated changes in environmental interactions. Developing squid, for example, encounter a range of flow regimes as a consequence of growing body size yet maintain propulsive efficiency due to key design changes to body geometry and locomotive system (Bartol et al. 2008). As indicated in the previous chapter, propulsive efficiency in (artificial) jellyfish also seems to depend on body geometry. Indeed, the study of phenotypic plasticity and ontogeny of juvenile jellyfish medusae presented in the following confirms a tight link between body geometry and propulsion efficiency, and subsequently guides design studies for optimizing the tissue-engineered jellyfish's shape (chapter 7).

6.2 Phenotypic Plasticity in Juvenile Jellyfish Medusae Facilitates Efficient Animal-Fluid Interactions

This section was submitted to *Biology Letters* on January 23, 2010 and published online March 24, 2010 as a part of a special feature on "Control and dynamics of animal movement". It is reproduced as is except for minor changes to style, formatting and figure presentation.

6.2.1 Authors

Janna C Nawroth[1], Klara E Feitl[2], Sean P Colin[3], John H Costello[4] and John O Dabiri [5]

6.2.2 Author Contributions

J. O. D. and J. C. N. conceived the project and designed the experiments. J.C.N. performed the experiments, analyzed the data and prepared the manuscript. J. O. D., K. E. F., S. P. C. and J. H. C. provided advice and training, and made final edits to the manuscript.

6.2.3 Abstract

Locomotion and feeding in marine animals are intimately linked to the flow dynamics created by specialized body parts. This interaction is of particular importance during ontogeny, when changes in behavior and scale challenge the organism with shifts in fluid regimes and altered functionality. Previous studies have indicated that scyphozoan jellyfish ontogeny accommodates the changes in fluid dynamics associated with increasing body dimensions and velocities during development. However, in addition to scale and behaviour that — to a certain degree — underlie the control of the animal, flow dynamics are also dependent on external factors such as temperature. Here, we show phenotypic plasticity in juvenile *Aurelia aurita* medusae, where morphogenesis is adapted to altered fluid regimes imposed by changes in ambient temperature. In particular, differential proportional growth was found to compensate for temperature-dependent changes in viscous effects, enabling the animal to use adhering water boundary layers

[1]Division of Biology, California Institute of Technology, Pasadena, California, USA
[2]Department of Ecology and Evolutionary Biology, University of California, Irvine, CA 92697, USA
[3]Department of Marine Sciences, University of Connecticut, Groton, CT 06340, USA
[4]Biology Department, Providence College, Providence, RI 02918, USA
[5]Graduate Aeronautical Laboratories and Bioengineering, California Institute of Technology, Pasadena, California, USA

as "paddles" — and thus economize tissue — at low temperatures, while switching to tissue-dominated propulsion at higher temperatures where the boundary layer thickness is insufficient to serve for paddling. This effect was predicted by a model of animal–fluid interaction and confirmed empirically by flow-field visualization and assays of propulsion efficiency.

6.2.4 Introduction

The swimming and feeding performance of marine animals depends on the interaction of fluid flow and body morphology. For example, an array of body appendages such as hairs, cilia or tissue lappets (figure 6.1a) can serve either as a paddle or as a sieve (Koehl et al. 2001), depending on the ratio of inertial versus viscous fluid forces as expressed by the Reynolds number:

$$Re = \frac{bU}{\nu}, \tag{6.1}$$

where ν is the kinematic viscosity of water, b is the appendage width and U is the velocity of appendage relative to water. As the appendage is set in motion, the surrounding fluid does not slip with respect to the surface of the appendage. Consequently, a velocity gradient, i.e., boundary layer, forms in the water between the appendage and the free-stream flow (figure 6.1b). The lower Re, the thicker becomes this boundary layer of sheared fluid relative to the gaps of the appendage array, eventually overlapping between the neighboring edges and conferring additional paddle surface. Conversely, at increasing Reynolds numbers, the boundary fluid layer retreats, turning the array into a grate useful for filtering (figure 6.1c). New functions may thereby arise from unchanged structures simply through a shift in velocity or scale (Koehl 2004), whereas continuous function may be achieved when changes in fluid dynamics owing to scaling effects are compensated by behavioral or morphological responses (Yen 2000). Furthermore, tuning morphogenesis to fluid dynamics may conserve resources as suggested by a recent study on ephyrae, i.e.,

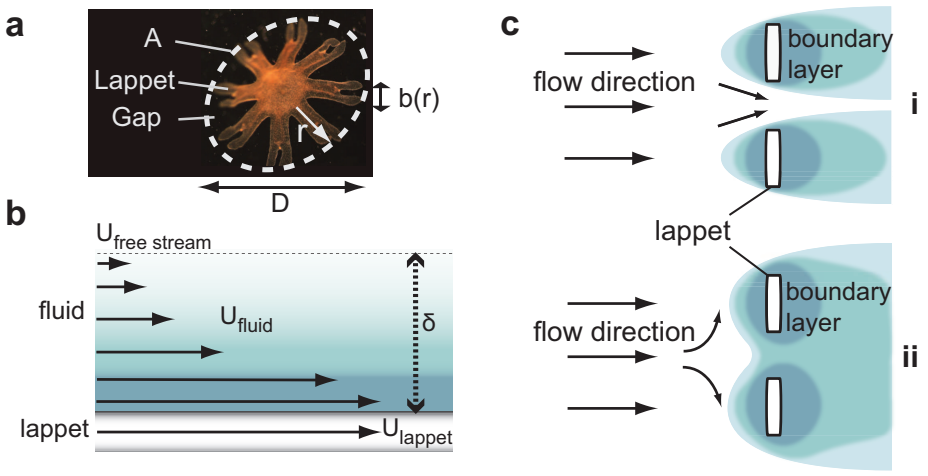

Figure 6.1. Model of body–fluid interactions in jellyfish ephyrae.

a, Characteristic parameters of ephyra morphology. A, potential bell area; D, diameter; r, radial lappet position; $b(r)$, lappet width at radial position r. **b**, Model of boundary layer formation on solid surface. U, velocity. Arrows represent velocities relative to free stream flow. Thickness of boundary layer (δ) denotes distance from solid surface to the point where U_{fluid} = 0.99% U_{free} stream. **c**, Schematic illustration of the two operation modes of the lappet array with different flow Reynolds numbers: (i) filter mode with no boundary layer overlap (high Re); (ii) paddle mode with complete boundary layer overlap (low Re). Different shades of blue correspond to velocity gradient in boundary layer as in (b).

juvenile scyphozoan medusae (Feitl et al. 2009). In particular, boundary layer overlap allows ephyrae to propel themselves through the water with a lean, starlike array of lappets, also referred to as lobes, instead of employing a full bell. As the animals increase in size, the reduction in boundary layer thickness is balanced by gap-narrowing tissue growth, ensuring complete boundary layer overlap throughout the development (figure 6.2d). These results indicate that jellyfish ontogeny exploits viscous effects to minimize the costs of tissue maintenance without compromising momentum transfer essential for swimming and feeding.

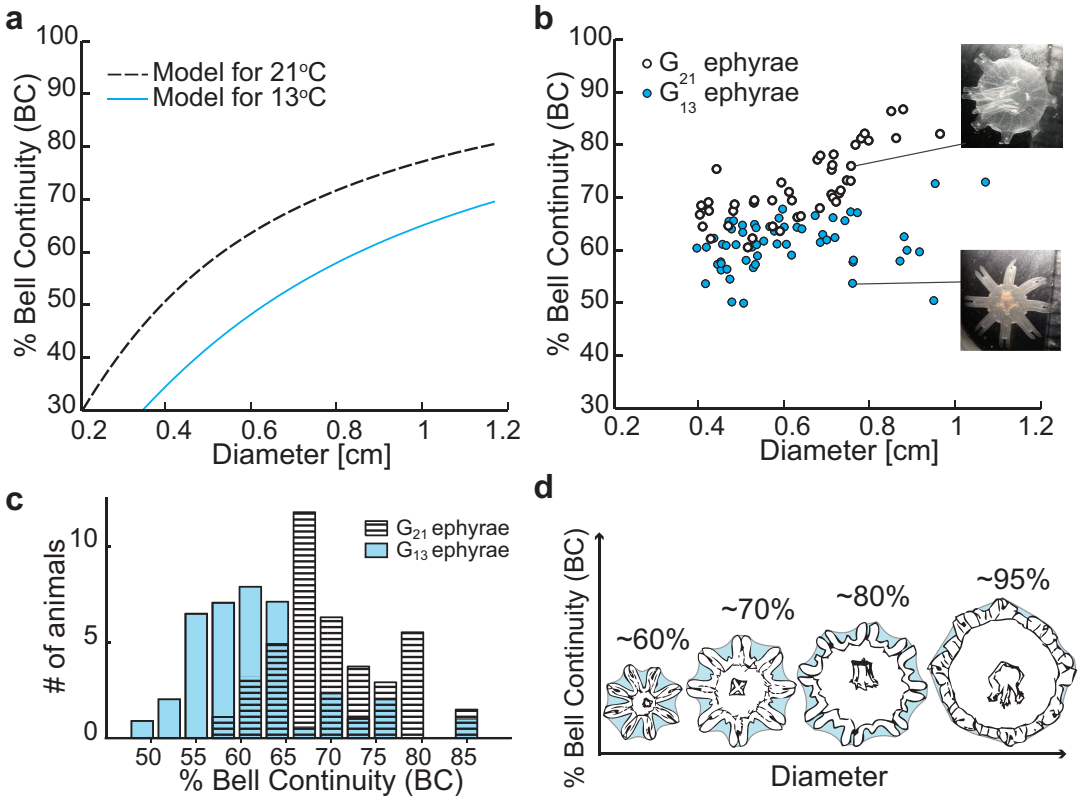

Figure 6.2. Predicted versus observed temperature-dependent morphological changes in jellyfish ephyrae.

a, Stokes model of bell continuity (BC) as a function of diameter, with $C = 0.8$. Blue line, model for 13°C; black dashed line, model for 21°C. **b**, Morphometric data of *Aurelia aurita*. BC is plotted against diameter. Blue circles, G_{13} ephyrae; white circles, G_{21} ephyrae. Right: two ephyrae from G_{21} (top) and G_{13} (bottom) are depicted to illustrate the differences in morphology. **c**, Histogram of BC values of the two temperature groups ($n = 41$ for each group, equal distribution of diameters). Blue bars, G_{13} ephyrae; black striped bars, G_{21} ephyrae. **d**, Model of continuous boundary layer overlap at all stages of bell development.

However, given that ephyral development is tuned to scale-dependent changes in Reynolds number, it raises the question as to whether it is capable of adapting to variation in other factors affecting *Re*, most notably water viscosity, which is strongly dependent on temperature. Such adaptive "phenotypic plasticity", the environmentally sensitive production of alternative phenotypes by the given genotype (DeWitt and Scheiner 2004) would be beneficial for globally distributed scyphozoan jellyfish species like *Aurelia aurita*, which are subject to significant temperature (and thereby viscosity) variation. Here, we extend the fluid-dynamical model of ephyral ontogeny proposed by Feitl et al. (2009), in conjunction with experimental measurements of ephyral morphology, fluid dynamics and swimming performance, in order to determine whether jellyfish morphogenesis is plastic in response to temperature conditions, and if so, whether the changes can be considered adaptive by facilitating economic and effective animal–fluid interaction.

6.2.5 Materials and Methods

6.2.5.1 Animals

Experiments were performed with newly budded Scyphozoan medusae of the species *A. aurita* obtained from aquaculture (New England Aquarium, Boston, MA, USA). Animals were maintained in artificial sea water (Seachem's Marine Salt) gently stirred by aeration. At the onset of the study, the ephyrae were randomly distributed into two groups subsequently kept at water temperatures of 13°C and 21°C, a span that lies comfortably within the range encountered by *A. aurita* in the wild (Lucas 2001). The two groups will be referred to as G_{13} and G_{21} in the following. The animals were fed daily with freshly hatched *Artemia salina*.

6.2.5.2 Morphometric Analysis

Over the course of development, the eight-armed ephyra transforms into the circular adult medusa. An idealized adult silhouette can be superimposed onto the ephyral body plan by circumscribing the lappets with a circle of diameter D, enclosing the potential bell area A (figure 6.1a):

$$A = \pi \left(\frac{D}{2} \right)^2, \tag{6.2}$$

The progress of transformation from ephyral to adult shape was quantified using the so-called bell continuity (BC) index, defined as the percentage of potential bell area comprised of ephyral tissue:

$$BC = \left(\frac{A - G}{A} \right) \cdot 100, \tag{6.3}$$

where G is the total gap area, i.e., the sum of wedge-shaped spaces between adjacent lappets. A BC value close to 100% thus corresponds to the approximate shape of an adult *Aurelia* medusa. BC values were determined once every week by measuring diameters and gap areas (ImageJ software; National Institutes of Health). A two-tailed Wilcoxon rank sum test (equivalent to Mann–Whitney U-test) was used to compare median BC values in G_{13} and G_{21}.

6.2.5.3 Stokes Model

A model of boundary layer formation around ephyral lappets was derived from Stokes' first problem, i.e., the flow over an abruptly started flat plate (Schlichting and Gersten 2000). The model was customized to ephyral morphology to assess the effect of temperature on morphogenesis under the constraint that complete boundary layer overlap be present at each stage of development (Feitl et al. 2009). Briefly, the fluid boundary layer thickness δ at radial position r along the lappet is estimated by

$$\delta(r) = \frac{bC}{\sqrt{Re(r)}}, \tag{6.4}$$

where C is a constant of proportionality whose magnitude for flow past flat plates is approximately 1 (Schlichting and Gersten 2000). *Re(r)* is the lappet Reynolds number defined as

$$Re(r) = \frac{rb\omega_T}{\nu_T}, \tag{6.5}$$

where ν_T is the kinematic viscosity of sea water at temperature T; b, lappet width at radial position r; $\omega_T$denotes angular speed of contraction at temperature T. Viscosities $\nu_{13} = 1.25 \times 10^{-6}$ m^2 s^{-1} and $\nu_{21} = 1.05 \times 10^{-6}$ m^2 s^{-1} were determined empirically using a stress rheometer (AR 1000, TA Instruments). Average angular speeds (swept angle divided by contraction time) were $\omega_{13} = 14$ and $\omega_{21} = 18.5$ rad s^{-1} in both G_{13} and G_{21} animals. Note that from equation (6.5), we expect a 25% greater value of $\delta(r)$ at 13°C when compared with 21°C, because of the temperature dependence of viscosity and angular speed. The total boundary layer A_{BL} is approximately twice the area of the boundary layer integrated over each lappet edge:

$$A_{BL} \approx 2N \int_0^{r_{max}} d(r)dr, \tag{6.6}$$

with $N = 8$, number of lappets. The constraint of complete boundary layer overlap demands that $A_{BL} > G$, and we can express the minimal BC value (equivalent to maximal gap area) fulfilling this condition as a function of diameter, yielding a family of curves for different temperatures. The shift between the two model functions for $T =$ 21°C and for $T = 13$°C predicts the difference in bell formation between animals raised at either temperature, under the constraint of complete boundary layer overlap (figure 6.2a). Note that the choice of the proportionality constant C influences the *absolute* vertical position of the family of model curves but does not alter their shift relative to

each other. The value $C = 0.8$ was chosen such that the model curve for $T = 21$°C fits, i.e., falls just below, the corresponding morphometric data as previous studies have documented complete boundary layer overlap under comparable conditions (Feitl et al. 2009).

6.2.5.4 Boundary Layer Visualization

Fluorescein dye was used to visualize fluid boundary layers surrounding swimming ephyrae at different water temperatures. For this, dye/sea water solution was injected in the immediate proximity of a freely swimming animal and highlighted using side illumination. The error of the boundary layer visualization can be estimated by the distance the dye will diffuse during the duration of one contraction (and thereby blur fluid boundaries). Diffusion distance l during time period Δt can be derived by

$$l = C_{Diff}\Delta t = \frac{\nu_T}{N_S} \tag{6.7}$$

where C_{Diff} and N_S are the diffusion constant and Schmidt number, respectively. With $N_S = 2000$ for fluorescein (Lavertu et al. 2008), we find that at 21°C, dye diffuses over a distance of $l = 0.013$ mm during contraction. This compares favorably to the theoretical boundary layer thickness, ranging from $\delta_{min} = 0.03$ mm (lappet tip) to $\delta_{max} = 0.5$ mm (lappet "root") in the coldwater-reared animals that we assayed. Similar relations are found for 13°C ($l = 0.013$ mm, $\delta_{min} = 0.05$mm, $\delta_{max} = 0.7$ mm). We conclude that the visualization error due to diffusion is negligible compared to boundary layer thicknesses and the differences seen in overlap at different temperatures (figure 6.3a,b).

6.2.5.5 Swimming Performance

Swimming performance was defined as the average distance traveled per full stroke (90° sweep), measured in units of body length/pulse. Measurements were obtained from movie recordings of freely swimming ephyrae at different ambient water temperatures

(Sony HDR-SR12 Camcorder, 30 fps). Temperature changes were induced gradually (max. 0.2°C min^{-1}) to avoid shock responses. A two-tailed Wilcoxon rank sum test was used to compare median swimming performances in G_{13} and G_{21} animals.

6.2.6 Results

6.2.6.1 Effects of Temperature on Morphogenesis and Behaviour

BC values in G_{13}jellyfish were significantly lower when compared with animals of equal diameter distribution grown at 21°C (G_{13}: median $BC = 62$, G_{21}: median $BC = 70$, Wilcoxon rank sum = 1232, $n_1 = n_2 = 41$, z-statistic = −4.3495, $p = 1.4 \times 10^{-5}$ two-tailed; figure 6.2c). G_{13} ephyrae increased in body diameter at a two- to threefold lower rate than G_{21} ephyrae. No obvious behavioral differences were observed in G_{13} versus G_{21} animals. In particular, pulsation frequencies as a measure of activity were comparable in both groups (ca.1.6 strokes s^{-1}).

6.2.6.2 Fluid Boundary Layer Overlap

Consistent with Feitl et al. (2009), the relation of *BC* value to body diameter measured in G_{13} and G_{21} ephyrae approximately followed the shape of the Stokes model curves. Note that we do not expect quantitative agreement between experimental results and theoretical forecasts because of the free scaling parameter C; however, we do observe qualitative agreement. In particular, the distribution of (D, BC) measurements from G_{21}ephyrae was shifted upward when compared with G_{13} ephyrae, as predicted by the two model curves (figure 6.2a,b). This suggests that, as G_{21} animals reduce gap sizes when compared with G_{13} animals, they are able to compensate for the diminished boundary layer formation at 21°C and thereby avoid operating in the (propulsion-inefficient) sieving mode. Consistent with this assumption, G_{13} animals swimming at 21°C indeed failed to develop fluid-webbing (figure 6.3a), whereas the same animals assayed at 13°C

showed complete boundary layer overlap (figure 6.3b).

6.2.6.3 Functional Consequences

G_{13} animals showed significantly higher stroke efficiency at 13°C than at 21°C water temperature (median performances of 0.88 versus 0.58 body lengths per stroke, Wilcoxon rank sum = 63, $n_1 = n_2 = 7$ (includes apparent outliers), $p = 0.02$ two-tailed; figure 6.3c,d). This result is consistent with the Stokes model and the dye visualization assay, suggesting a paddle mode of the G_{13} morphology at a lower temperature when compared with a sieving or "water-treading" action at the higher temperature (supplementary movies 13 and 14).

6.2.7 Discussion

Here we demonstrate that phenotypic plasticity in Scyphozoan ephyrae tunes ontogeny to temperature-dependent changes in fluid flow, facilitating efficient animal–fluid interactions and conserving resources during development. In particular, morphology was found to dynamically exploit viscous effects by recruiting adhering boundary fluid layers as additional paddles throughout development. Crucially, the animals do not depend on the presence of a particular boundary layer thickness but are able to compensate for temperature-dependent thinning of the fluid-webbing by tissue growth. Thereby, tissue formation is economized when possible, i.e., without compromising vital functions such as swimming performance. Such "smart" economy can be crucial to survival in the ephyral stage, a bottleneck in jellyfish population dynamics (Haruto and Chiharu 2005) and may improve survivorship in jellyfish populations subjected to temperature variation as induced, for example, by climate and ocean circulation changes.

We acknowledge, however, that the correlation between temperature-dependent changes in morphology and Reynolds number need not be an evolutionary adaptation, even though the fluid dynamic effects we describe in the paper appear beneficial to

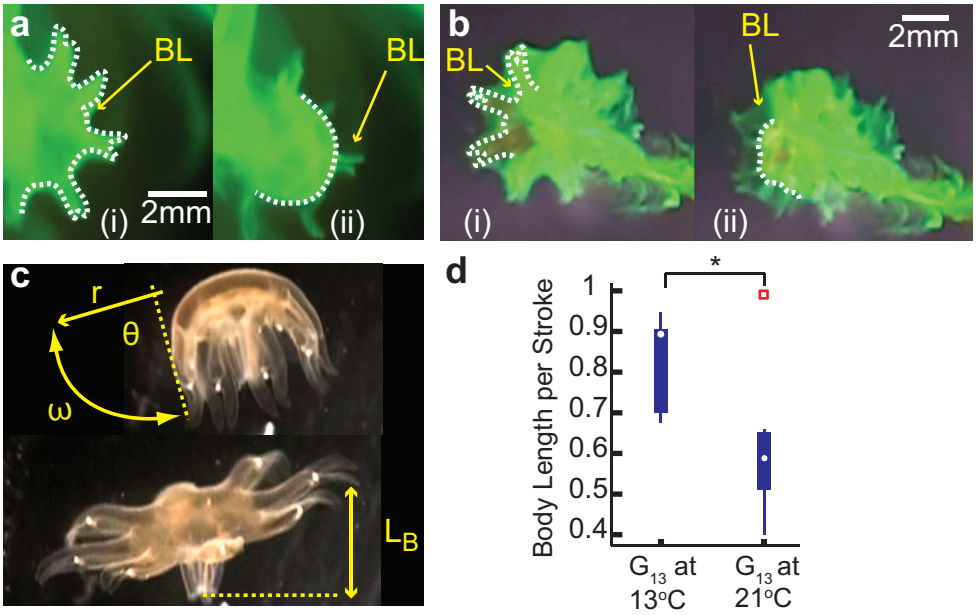

Figure 6.3. Temperature-dependent thickness of boundary layers and consequent propulsion efficiency **a, b**, Dye visualization of boundary layer during powerstroke. Dotted line indicates outline of animal body. BL, boundary layer. **a**, Sieve-mode: G_{13}ephyra swimming at 21°C water temperature. (i) Start of powerstroke, bell is fully relaxed, (ii) end of powerstroke, bell is fully contracted. Note that the thin boundary layer outlines the body but fails to connect between lappets. **b**, Paddle-mode: G_{13}ephyra swimming at 13°C water temperature. (i) Start of powerstroke, bell is fully relaxed, (ii) end of powerstroke, bell is fully contracted. Note the delay in boundary layer motion when compared with body motion, visualizing the velocity gradient at the fluid–solid interface. **c**, Parameters of ephyra propulsion. r, Radial position along lappet; ϑ, swept angle; ω, angular velocity; L_B, body length. **d**, Effect of ambient water temperature on propulsion efficiency of G_{13}ephyrae. Box plots show body length traveled per stroke at 13°C ($n = 7$) and at 21°C ($n = 7$). White marks correspond to median, the edges of the box are 25th and 75th percentiles, whiskers indicate extreme data points not considered outliers. Outliers are plotted as individual squares. Asterisk represents significant difference in median values. The associated movies are supplementary movies 13 and 14.

the animal. Temperature affects many biological processes including development, and the differences in morphologies might be a side effect, not an adaptation specifically to changes in fluid regimes. Changing viscosity by chemical means does not seem to induce the phenotypic plasticity reported here, and further experiments are underway to confirm this finding (J. C. Nawroth & J. O. Dabiri 2010, unpublished data). This, however, does not rule out the possibility that temperature serves as a proxy for sensing boundary layer thickness during development, given that under natural conditions the animals would rarely encounter changes in viscosity and/or contraction speed brought upon by other means than temperature variation. Similarly, in addition to shedding light on fluid dynamic effects, the swimming performance assay might be sensitive to metabolic responses to the short-term temperature changes employed in this study. Along these lines, our next experiments will focus on isolating the acute physiological effects of temperature from its role on boundary layer thickness and animal–fluid interaction. In particular, we plan to investigate the propulsion efficiency of G_{21} animals at 21°C water temperature when compared with G_{13} animals in water of 21°C with artificially raised viscosity. Assuming that sufficient boundary layer thickness is the decisive factor in propulsion efficiency, and not exposure to a familiar ambient temperature, we expect both groups to show similar performances. In the long term, it would be interesting to elucidate the signaling pathways underlying the link between temperature, fluid forces and ontogenetic programs, given the emerging role of gelatinous species as model systems for regeneration and development (e.g., Hoffmeister-Ullerich 2007).

6.2.8 Acknowledgements

The authors thank Michael Mackel and Eric Mattson for technical assistance. We are particularly grateful for the generous support by the New England Aquarium, Boston, MA, and the Cabrillo Aquarium, San Pedro, CA, USA.

Chapter 7

Design Principle Fluid Dynamics: Body Shape Parameters Relevant for Fluid Transport, and Their Implementation *in vitro*

This chapter was published as part of the methods and supplementary information of Nawroth et al. (2012) reproduced in chapter 3. The thesis author has collected all data and composed all graphics and text unless noted otherwise.

7.1 Fluid Model and Empirical Validation

7.1.1 Introduction

Final medusoid body shape was inspired by the lobed geometry of early stage ephyrae featuring an array of lappets instead of a full bell. This design allows for compression-free bell contraction, enabling a single layer of cardiomyocytes to fold a planar PDMS thin film into a 3D conformation. However, as the previous chapter has shown, lappet geometry needs to be adapted to fluid conditions to ensure efficient propulsion. To simplify the design study, outer body diameter and number of lappets were kept constant across all medusoid designs while varying relative lappet length L_{Lappet} and relative

lappet broadening B_{Lappet}:

$$L_{lappet} = \frac{D_{in}}{D_{out}}, \tag{7.1}$$

$$B_{lappet} = \frac{W_{out}}{W_{in}}, \tag{7.2}$$

with D_{out}, outer diameter; D_{in}, inner diameter; W_{out}, outer lappet width; $W_{in.}$, inner lappet width (figure 7.1a). Parameter space was explored to achieve two functional objectives: The first goal was to approach propulsion efficiency achieved by ephyrae. Juvenile jellyfish adapt their lappet geometry to flow conditions as to promote an overlap of boundary layers within the gap separating neighboring lappets (figure 7.1b). In fact, boundary layer overlap is maintained throughout ephyral development, effectively converting the interlobal gaps into additional paddle surface and synergistically increasing bell drag. Without boundary layer overlap, propulsion becomes inefficient as fluid leaks through the gaps, reducing drag and turning the bell into a sieve (figure 7.1c) (Feitl et al. 2009; Nawroth et al. 2010). Optimal medusoid design therefore needs account for the relation between geometry and boundary layer formation to maximize bell drag. Second, lappet dimensions are constrained by considerations of mechanical stability, feasibility of fabrication and freedom of motion (figure 7.1d). In particular, maximal lappet dilation is geometrically bounded by the condition that lappets may not interfere with each other during contraction.

7.1.2 Methods

The relation between bell geometry and drag was studied through a simple fluid-solid interaction model. Lappets were represented as n continuous arrays of elliptical cylinders perpendicular to the flow (figure 7.2a). Each array corresponded to a radial lobe position r_i, with i= *1,...,n*, and was characterized by parameters, b_i, lobe width; L_i, width of lappet plus adjacent gap; N, number of lobes; v, kinematic fluid viscosity; and U_i, fluid

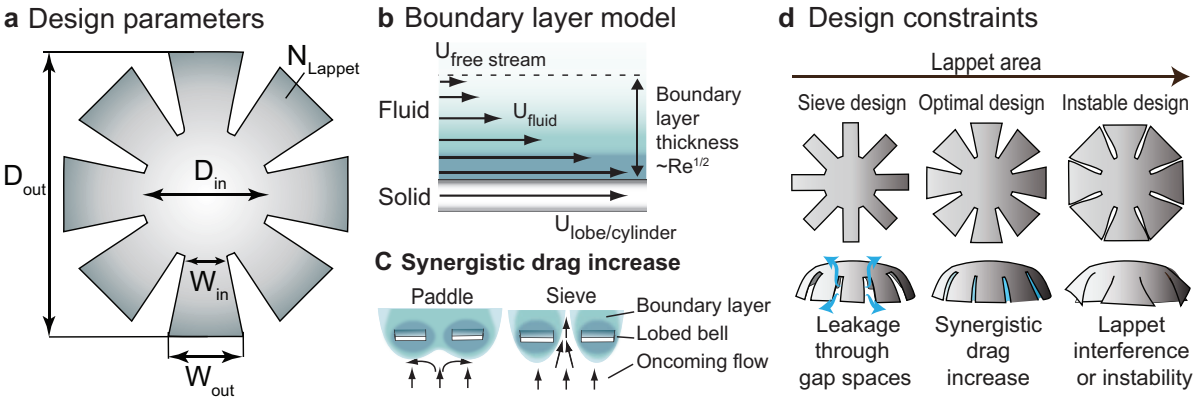

Figure 7.1. Medusoid design parameters, fluid interactions and design constraints.

a, Medusoid geometric parameters. Fixed parameters: outer diameter, $D_{out} = 9$ mm; number of lappets, $N_{Lappet} = 8$. Free parameters: inner diameter, D_{in}; outer lappet width, W_{out}, inner lappet width, W_{in}. **b**, Viscous boundary layer model describing velocity gradient at solid-fluid interfaces. Thickness of boundary layer is proportional to $Re^{-1/2}$, with Re = local Reynolds number. **c**, Given suitable medusoid geometry and flow conditions, overlap of neighboring boundary layers may occur, blocking interlobal gaps to oncoming flow. This raises both viscous and pressure drag, leading to synergistic increase in lobe drag and paddling efficiency (right) compared to the case of insufficient boundary layer overlap with interlobal leakage (left). **d**, Optimal medusoid geometries (center) promote sufficient boundary layer overlap, thereby minimizing leakage through interlobal gaps (left), and avoid instable or interfering lobe dimensions (right).

velocity which is the product of r_i and angular velocity ω. These parameters in turn determined local array properties P_i, porosity; Re_i, Reynolds number; and A_i, reference area :

$$P_i = (L_i - b_i)L_i^{-1}, \tag{7.3}$$

$$Re_i = b_i U_i \nu^{-1}, \tag{7.4}$$

$$A_i = (r_{r+1} - r_i)b_i N. \tag{7.5}$$

The drag factors of circular and elliptical cylinders at Reynolds numbers relevant for medusoid lobe contraction ($Re = 0.1$–20) have been characterized empirically as a function of Re and P Masliyah and Epstein 1971; Satheesh et al. 1999. Interpolation of the published data across our parameter space of interest allowed us to estimate local drag factor Cd_i for each radial lappet position (figure 7.2b). Total bell drag was calculated by summing local drag over all radial positions:

$$Drag_p = \sum_{i=1}^{n} \frac{1}{2}\rho Cd_i A_i U_i^{-2}, \tag{7.6}$$

where n was chosen high enough to approximate integration, subscript "p" stands for prediction, and ρ is fluid density. We validated the model by empirically determining the relative magnitude of drag factors of two sets of medusoid-shaped and -sized acrylic discs ("medusoid dummies") varying systematically in lappet divergence within each set, and varying in relative lappet length across sets. The empirical order of drag factors within each set was compared to the order predicted by the model. Empirical drag data were obtained by measuring terminal sinking velocities of medusoid dummies in a cylindrical column containing glycerol-water solutions. The viscosity of the solution

depended on the relative proportions of glycerol and water. The mix was adjusted for each run to achieve a similar average lappet Reynolds number

$$\bar{Re} = \frac{1}{n}\sum_{i=1}^{n} b_i U_i \nu^{-1}, \tag{7.7}$$

for all tested shapes, and within a range covered by the fluid model. The column was 20 cm in width and 50 cm in height, minimizing edge effects and allowing the shapes to travel at least 30 cm at terminal velocity before reaching the bottom. The dummies were released electromagnetically to ensure zero starting velocity and avoid tilting. A metal weight attached to the center of the acrylic disc served the dual purpose of responding to the electromagnetic field and lowering the center of mass to stabilize the falling trajectory. Terminal sinking velocities were determined from video recordings of the fall. We then applied equation

$$Cd_e = \frac{2W}{\rho U_T^2 A}. \tag{7.8}$$

to calculate empirical drag factors with U_T, terminal velocity, A, reference area and W, weight of the medusoid dummy (figure 7.2d) (Halliday et al. 2010). Predicted drag factors were derived by computing total drag from equation (7.6) with $U_i = U_T$ for all radial positions, and applying

$$Cd_p = \frac{2Drag_p}{\rho U_T^2 A} \tag{7.9}$$

7.1.3 Results and Discussion

For both sets of medusoid dummies it was found that empirical and predicted orders of normalized drag factors were consistent. Importantly, this order was independent of the order of average lappet Reynolds numbers (figure 7.2e). These results, although based on rigid medusoid dummies, suggested that the model was suitable for predicting the

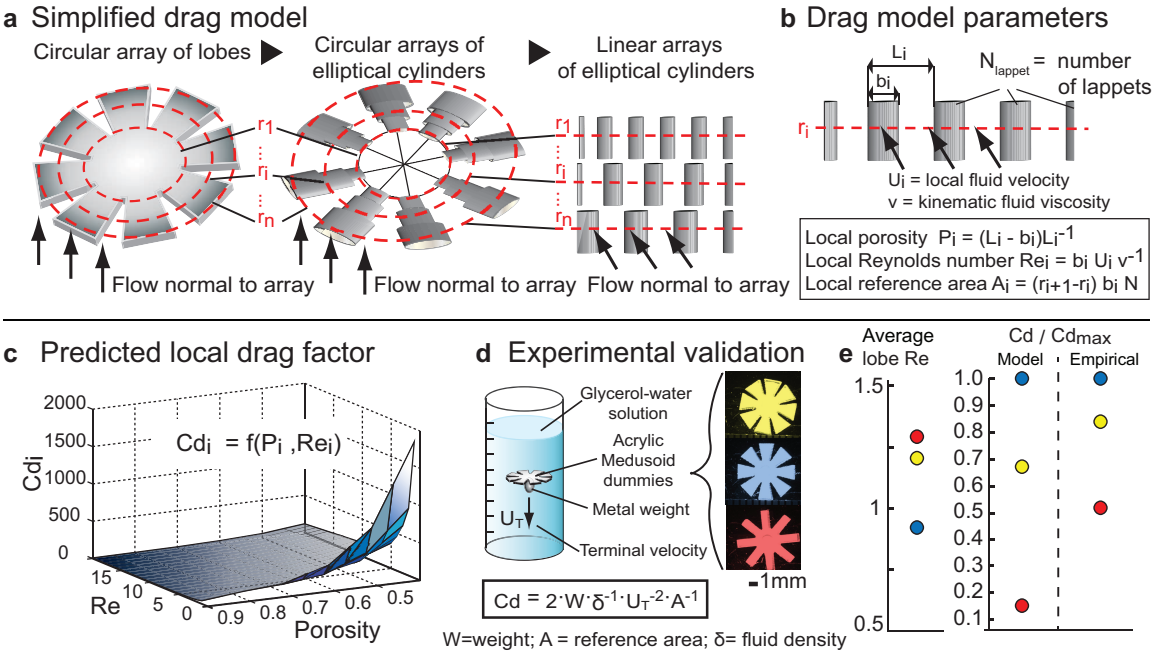

Figure 7.2. Model and empirical validation of medusoid-fluid interaction

a, Bell drag was estimated from simple fluid-solid interaction model. Medusoid lobes were represented as continuous arrays of elliptical cylinders perpendicular to flow. **b**, At each radial position, geometric and kinetic parameters are given from overall geometry and flow conditions, allowing to derive local porosity, Reynolds number and reference area. **c**, Local Reynolds number and porosity predict local drag coefficient. **d**, Empirical validation of the model was achieved by sinking acrylic Medusoid dummies of varying geometries in glycerol-water solutions. Drag factors were calculated from terminal sinking velocity. **e**, Empirical order of drag factors in medusoid dummies was consistent with predicted order (right), and independent of the order of average lobe Reynolds numbers (left). Drag factors were normalized to respective maximal value. Color code relates dummy shapes depicted in (d) with plotted data.

relative performance of actual medusoid constructs as a function of geometry. We subsequently computed total bell drag of medusoid constructs as a function of relative lappet length and divergence (figure 7.3a). Flow parameters were adjusted to tissue culture conditions, with cell media viscosity v=0.8 x10^{-6}m^{2}s^{-1} and average muscle construct velocity ω=2.5 rad s^{-1}. In general, higher lobe divergence resulted in higher maximal drag; however, lobe divergence was limited to 1.8 due to stability and fabrication constraints. The optimal design chosen for medusoid fabrication corresponded to the geometry achieving peak drag at lobe divergence of 1.8. For performance comparisons we also chose to fabricate a suboptimal design with much lower predicted drag at same relative lappet length. Final optimal and suboptimal body designs were implemented in live medusoid tissue constructs (figure 7.3b,c), which exhibited the expected propulsion and sieving behavior, respectively (supplementary movie 4). The following chapter discusses the functional evaluation of optimal and suboptimal medusoid designs with respect to native jellyfish function.

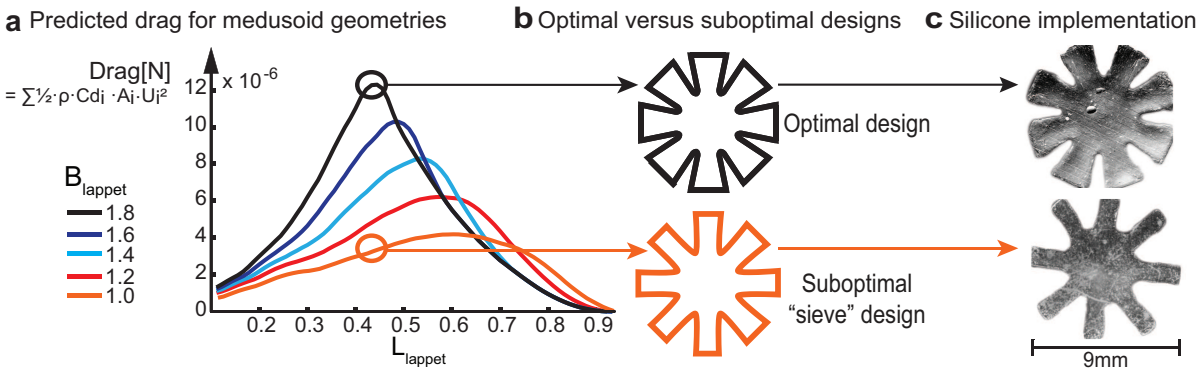

Figure 7.3. Model and implementation of flow-optimized medusoid geometries.

a, Total predicted bell drag of in medusoid geometries as function of relative lappet length and broadening. In general, greater lappet broadening results in disproportionally greater bell drag indicating synergistic effects of additional area and reduced leakage. Note that for stability reasons, maximal relative lappet broadening was 1.8. **b**, Final optimal design and example of suboptimal design promoting paddling and sieving, respectively. **c**, Implementation of designs in muscle-powered silicone substrates.

Chapter 8

Functional Performance: Quantify Jellyfish Function and Establish Functional Metrics

This chapter expands on the methods and supplementary information of Nawroth et al. (2012) reproduced in chapter 3. The thesis author has collected all data and composed all graphics and text unless noted otherwise.

8.1 Introduction

The swim stroke of optimally designed medusoids bears remarkable resemblance to native jellyfish (supplementary movie 4), qualitatively confirming the successful implementation of key mechanistic design principles underlying jellyfish function. Further mechanistic insight and evaluation of the different designs requires however a quantitative comparison of fluid dynamics and transport associated with the stroke cycle, i.e., the generation of well-defined propulsion and feeding currents (Dabiri et al. 2005). These currents can be quantified in terms of velocity and vorticity, and they result in quantifiable animal locomotion and fluid transport toward the bell.

8.2 Methods

8.2.1 Velocity and Vorticity Fields

Fluid dynamics in free-swimming jellyfish and medusoids were assessed through digital particle image velocimetry (DPIV) that allows for quantitative analysis of flow created by swimming animals in a two-dimensional plane (Adrian 1991). In DPIV, fluid motion is determined by quantifying the displacement vectors of small seeding particles between successive video frames. The same basic DPIV setup was used for jellyfish and Medusoids (figure 8.1a). The specimens were imaged in custom-built acrylic containers filled with either artificial seawater at room temperature (for jellyfish), or with Tyrode's solution maintained at 35°C using a custom-made heated stage (for medusoids). Additionally, the medusoid tank was equipped with two U-shaped platinum electrodes installed at opposite walls of the tank and connected to a voltage pulse generator (MyoPacer, IonOptix) for electrical field stimulation of the tissue constructs. The solutions were seeded with neutrally buoyant, silver-coated, hollow glass spheres with a nominal diameter of 13 μm (Potters Industries). Particles were illuminated with a 5 mW green (532 nm) laser pointer for studies in Medusoids, or a 300 mW green (532 nm) laser for studies in jellyfish, the difference in power reflecting the larger tank size required for unconstrained swimming of the jellyfish. The laser beam was diverged into a 1 mm thick planar sheet by a plano-concave cylindrical lens with a focal length of –4 mm (Thorlabs). The laser was positioned to one side of the tank to illuminate a horizontal plane dissecting the vertically swimming specimens along their bell diameter (figure 8.1a). A camera was installed perpendicular to the laser sheet (figure 8.1b). In some cases, a mirror was placed on the opposite side of the tank to reflect the laser sheet and improve illumination. In case of the jellyfish, the motions of the particles were recorded with a Sony HDR-SR12 camcorder (1440×1080 pixels, 30 frames per second; Sony Electronics). In case of the medusoids an A602f/fc Basler camera was used (656×491 pixels, 100

frames per second; Basler Vision Technologies). The raw videos (supplementary movie 5) were processed with an in-house DPIV algorithm (Willert and Gharib 1991). The DPIV interrogation window size was 32×32 pixels with 50–70% overlap (16 to 10 pixels step size). Velocity vectors were yielded from average particle displacement within each interrogation window (figure 8.1c). Resultant velocity vector and vorticity fields (figure 8.1d) were used to compare fluid transfer and vortex formation in medusoids and jellyfish.

8.2.2 Propulsion and Feeding Metrics

To assess feeding performance we derived the velocity profile and volumetric flow rates across the subumbrellar side during a single recovery stroke, corresponding to the generation of feeding currents per stroke cycle. Briefly, in each image frame of the recovery stroke sequence, a reference line was drawn to span the stopping vortex formed during the recovery stroke (figure 8.1d). This distance was found to approximate the diameter of subumbrellar bell aperture (i.e., the site of feeding) and was much easier to track in the DPIV image frames than the bell outline. The normal components of the velocity vectors across this reference line then corresponded to the velocity profile across the bell aperture at a given instant of time (figure 8.1e). Flow toward the bell was defined to be positive. To facilitate comparison between Medusoids and jellyfish, flow velocities were nondimensionalized by multiplying with the total duration of the recovery stroke and dividing by bell diameter. Volumetric flux across the area of the subumbrellar bell aperture was estimated by assuming that the specimens were axisymmetric and integrating the velocity profile over a circular area. Propulsion performance was defined as relative swimming speed expressed in units of body length per stroke. Here, body length denoted the bell height at maximal contraction.

Propulsion performance was calculated from bright field video recordings of free-swimming medusoids and jellyfish. The movements of the specimens were tracked man-

ually by choosing a reference point on the bell and recording the pixel coordinates in each frame. Displacements were then calculated as the difference in position between frames and converted to units of body length.

8.2.3 Statistical Analysis

Propulsion data were analyzed nonparametrically as discussed in detail in section 5.2. Briefly, statistical significance of differences between sample populations was determined using the Wilcoxon rank-sum test; p-values were evaluated against a significance level of $\alpha = 0.05$. Data were represented in the so-called boxplot format which summarizes each data set in five numbers: median, 25th and 75th percentile, and the smallest and the greatest observation.

8.3 Results and Discussion

Optimally designed medusoids demonstrated propulsion and feeding functions that approached those observed in native jellyfish whereas suboptimal, sieve-designed medusoids exhibited consistent inferior performance in both categories (figure 3.5, 8.2c, supplementary movie 4). These differences are also reflected in the flow fields generated by each system. Whereas optimal medusoid and jellyfish exhibit comparable fluid acceleration and feeding vortex generation during power and recovery stroke, these features are underdeveloped in suboptimal medusoids (supplementary movies 6-8 and figure 3.4).

In conclusion, key design principles of jellyfish swimming and feeding function were identified and implemented in a tissue-engineered construct, resulting in biomimetic functional performance. Importantly, medusoid performance was compared to the native system using quantitative functional benchmarks of propulsion and feeding. Mechanistic understanding of the design was demonstrated by applying changes such that predictable deterioration of performance resulted.

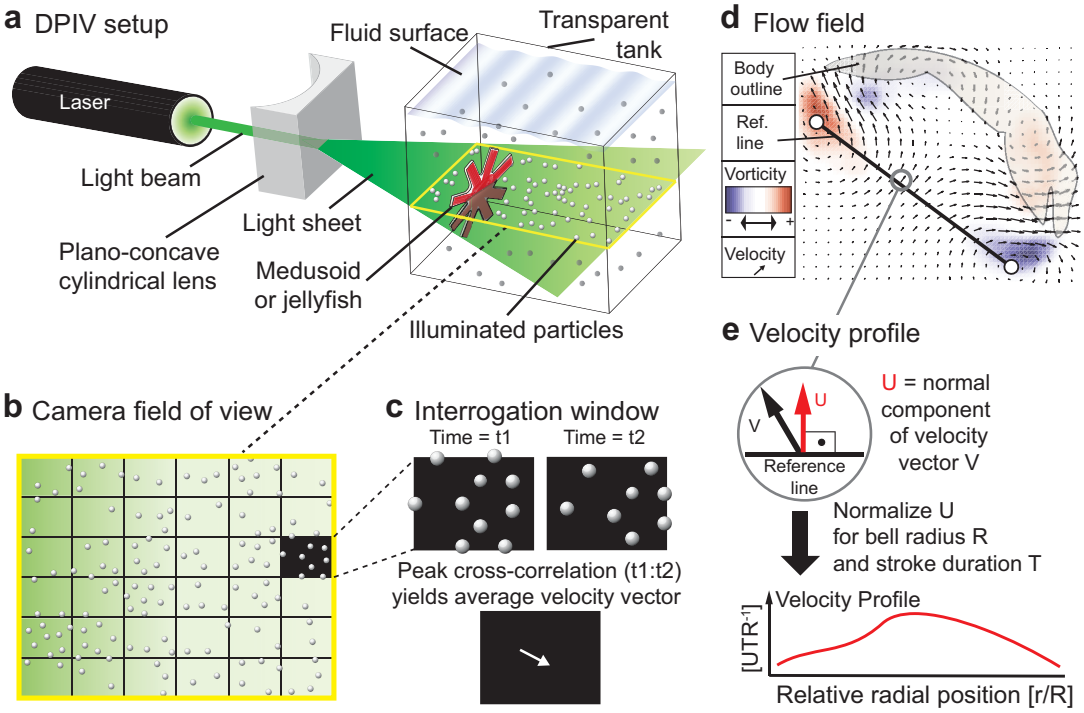

Figure 8.1. Flow field visualization and functional evaluation.

a, Digital particle image velocimetry (DPIV) setup for jellyfish and medusoids. A laser light beam directed through a plano-concave cylindrical lens diverges into light sheet of ca.1 mm in thickness. This illuminates a plane within the particle-seeded fluid, thereby visualizing 2D fluid motion. **b**, Top-view onto plane of illuminated particles as seen by video camera. For flow analysis the field is divided into subsample areas, so-called interrogation windows. **c**, Each interrogation window is compared at time 1 (*t1*) with the corresponding area at time 2 (*t2*) in the following video frame. The average velocity vector for the window corresponds to the shift of particle positions at *t1* that results in matching most of the particle positions at $t2$, equal to peak crosscorrelation between positions at *t1* and $t2$. **d**, The flow field is derived by plotting the average velocity vector for all windows in the field of view. Further analysis on the flow yields metrics such as vorticity (blue: clockwise; red: anti-clockwise) or the velocity profile across a line of reference. **e**, The nondimensionalized velocity profile is derived from the normal component of the velocity vectors across a line of reference.

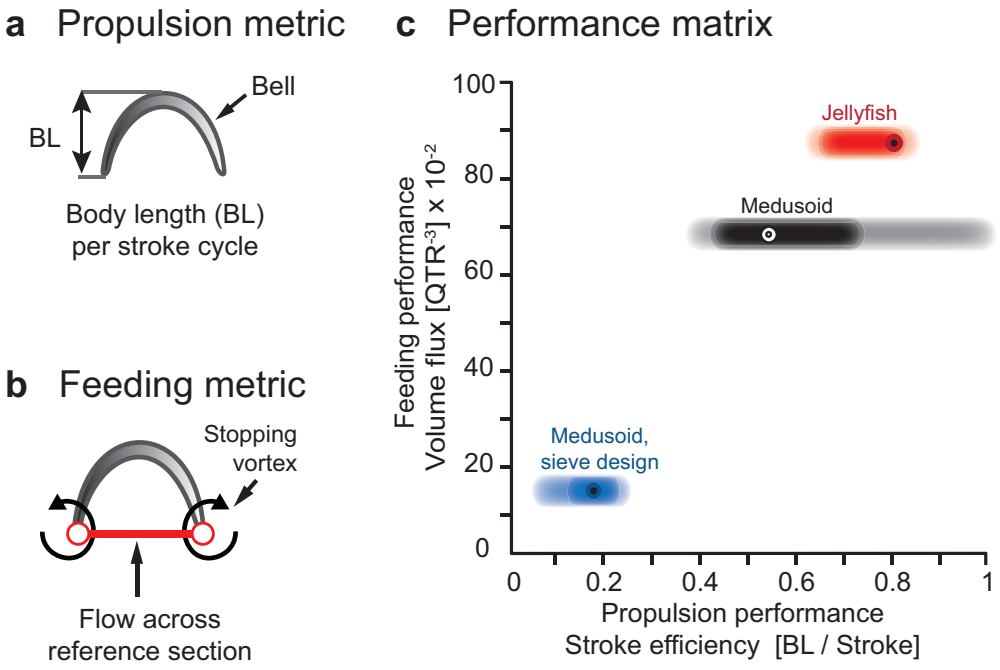

Figure 8.2. Performance metrics and results matrix.

a, Propulsion metric. Swimming performance is quantified in units of $BL/Stroke$, i.e., body lengths traveled per stroke cycle. **b**, Feeding metric. Feeding performance is quantified in units of QTR^{-3}, i.e., volume flux Q during recovery stroke across reference section spanned by stopping vortices, normalized for R, bell diameter and T, duration of recovery stroke. **c**, Results matrix illustrating range of feeding and propulsion performances of jellyfish, optimally designed medusoids, and sieve-designed medusoids. Modified boxplot representation: Bull's eyes, median; left edge of inner ellipsoid, 25th percentile; right edge of inner ellipsoid, 75th percentile; outer ellipsoid, extreme data points.

Chapter 9

Discussion and Outlook

9.1 Summary of Achievements

Using a systematic design strategy, a tissue-engineered jellyfish was built that generates biomimetic feeding and propulsion currents. Three key design components underlying jellyfish function were revelead and implemented using bioengineered substitutes:

- **Synchronous bell actuation** was accomplished in the meduoid by a monolayer of anisotropic engineered cardiac muscle, a foldable body geometry and electrical field stimulation.
- **Asymmetric stroke kinematics** were generated in the meduoid by a bilayer of silicone and muscle.
- **Fluid dynamics** efficient for propulsion were achieved in the meduoid by using a flow-optimized body geometry.

The medusoid design process implemented the conceptual framework towards design standards in tissue-engineering discussed in chapter 2:

- The iterative **design-build-test algorithm** was applied to reveal key design principles. Quality control criteria, such as proper alignment of contractile fibers, ensured proper implementation of engineered solutions.

- An **economic design** using only two components (muscle and silicone) was implemented by exploiting the electrical coupling of cardiac muscle to substitute for the jellyfish motor nerve net.
- **Physiological scaling laws** that relate body geometry to fluid environment were revealed, modeled and implemented.
- An **economic fabrication strategy** was devised that uses a combination of microfabrication and cellular self-organization to generate anisotropic muscle.
- **Performance testing** was based on system-wide metrics of swimming and feeding function established in the native system.

9.2 Remaining Challenges

9.2.1 Variability

Only 10% of the cultured medusoids were fully functional; most samples had small defects in muscle architecture that impaired optimal contraction. More reliable and repeatable function in engineered constructs may be achieved by installing automated fabrication procedures that reduce human error. Further, automated characterization and quality control procedures for cellular materials, including cell selection based on gene expression markers and structural criteria, could reduce tissue variability. Variability in commercial tissue culture agents and materials presents an additional source of error, and common composition standards and tolerances could facilitate systematic comparisons between experiments.

9.2.2 Long Term Survival and 3D Tissues

The medusoids are powered by a monolayer of a single cell type specialized for contraction, i.e., cardiomyocytes isolated from neonatal rat hearts. Since these cells are non-dividing, medusoid survival and function is limited by the viability and purity of the initial cell population. In cell culture conditions, any contamination with non-contractile, dividing cell types naturally found in the tissue of origin, such as fibroblasts, eventually (i.e., after 1-2 weeks) lead to their dominance, overgrowth and suffocation of the muscle layer, and subsequent loss of medusoid function. This illustrates two challenges: Maintaining tissue-organization, and designing viable 3D tissues.

In particular, designing 3D tissues for long term survival requires providing the cues necessary for self-regulation and maintenance of tissue-organization that prevent any single cell type from overgrowing the others. Solid, multilayered tissues require vasculature or other internal interfaces with the extracellular fluid to aid diffusion-mediated cellular gas and mass exchange. Further, convective fluid transport mechanisms are needed whenever diffusion alone does not suffice.

9.2.3 Clinical Application

The cellular materials used in this study (rodent cardiomyocytes) are not suitable for application in humans. In order to transfer the insights to clinical application, equivalent but compatible materials such as induced pluripotent stem cells and other sources of human cells have to be adapted.

9.3 Next Steps and Applications

An immediate extension of the work reported in this thesis is to exploit the medusoid as a tool for testing the effects of mechanical jellyfish features on locomotion and feeding that were omitted in the current medusoid design (figure 9.1). This includes

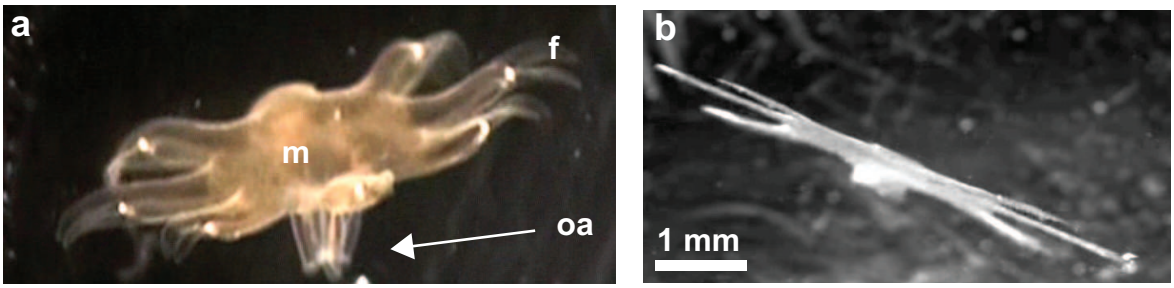

Figure 9.1. Example of jellyfish mechanical features not explored in the current medusoid design. **a**, Juvenile moon jellyfish. oa., oral arms; m, mesoglea; f, flaps. **b**, Medusoid.

assaying the oral arms which extend like a stalk behind the body and could potentially confer stability, or aid in feeding and propulsion by diverting currents and altering the flow and pressure field. Also unexplored are the mechanical properties achieved by the anisotropic architecture of the jellyfish mesoglea. They presumably aid in generating specific configurational changes and kinematics, and they could be implemented by changing the homogeneous composition and topography of the medusoid silicone body through embedded fibers or surface textures such as ridges. It would also be interesting to investigate the effect of passive, flexible flaps at the end of the lappets.

More complex next steps include adding other cell types to the medusoid design in order to augment its function and autonomy. Pacemaker cells from the heart, for example, could provide an internal stimulator for autonomous rhythmic contraction. Sensory nerve cells could activate all or parts of the muscle to induce locomotion or even turning in response to external stimuli and thus provide a crude mechanism for decision making.

Lastly, how can the insights gained in this thesis be practically applied to other tissue-engineering projects? The objective is to move away from biomimetic toward bioinspired design, i.e., a design that is based on mechanistic understanding rather than on mere copying of structures existing in nature. In summary, the universal approach as proposed in this thesis is an iterative strategy consisting of the following steps:

- Dissect the native tissue to reveal its structural entities, using physical dissection,

imaging and quantitative analysis.

- Identify the role of these structural entities in generating the desired mechanical or biochemical function.
- Develop bioengineered solutions that recapitulate key structure-function relationships within the specific clinical or technical context. Use quality control procedures to ensure proper implementation.
- Evaluate engineered construct based on quantitative performance benchmarks.
- Link functional flaws to structural elements and revise the design accordingly.

Chapter 10

Appendix: Movie Captions

Supplementary Movie 1

The stroke cycle in a free-swimming juvenile moon jellyfish (*Aurelia aurita*) consists of a muscle-powered contraction phase (power stroke) followed by elastic recoil (recovery stroke).

Supplementary Movie 2

Failure of biomimetically designed medusoid to contract and propel itself. The medusoid was stimulated at 1 Hz through an externally applied monophasic voltage square pulse (2.5 V/cm, 10 ms duration). Due to mismatch of muscle stresses and substrate compliance, muscle contraction does not result in sufficient bell deformation, and no thrust is generated.

Supplementary Movie 3

Optimally designed medusoid constructs exhibit jellyfish-like body contraction and propulsion. Medusoids were paced at 1 Hz through an externally applied monophasic voltage square pulse (2.5 V/cm, 10 ms duration). The first scene shows a mature construct still attached at its center to its acrylic template, just prior to release. Note that the striated appearance of the template is caused by its fabrication process; this striation does not reflect the alignment of the muscle tissue on top of the silicone membrane

covering the template. Subsequent scenes show exemplary propulsion of free-swimming medusoids.

Supplementary Movie 4

Jellyfish and optimal medusoids achieve comparable propulsion efficacy (distance traveled per stroke), whereas suboptimal medusoids ("sieve design") exhibit inferior performance. While medusoids were paced at 1 Hz through an externally applied electric field (2.5 V/cm, 10 ms duration), in this particular scene the jellyfish contracts at a frequency of ca.2 Hz. In order to facilitate comparison, the frame rate of the jellyfish recording was halved to synchronize stroke phases.

Supplementary Movie 5

Sequence of raw DPIV data of jellyfish, medusoid and suboptimally (= sieve-) designed medusoids. Here, fluid flow around the jellyfish/Medusoid bell is visualized by the displacement of neutrally buoyant particles suspended within the fluid and illuminated within a single plane using laser light. The relative motion of the particles allows quantifying 2D fluid flow within the plane.

Supplementary Movie 6

Fluid flow field and vorticity field of a juvenile jellyfish during the stroke cycle. The movie was generated from DPIV data. The power stroke is characterized by maximal fluid velocities and formation of a starting vortex, generating thrust. The recovery stroke is characterized by reduced fluid velocities and the formation of a stopping vortex, generating feeding currents towards the subumbrellar side.

Supplementary Movie 7

Fluid flow field and vorticity field of an optimally designed medusoid during the stroke cycle. The movie was generated from DPIV data. As in the jellyfish, the power stroke generates maximal fluid velocities and a starting vortex ring, resulting in thrust. The recovery stroke generates a stopping vortex ring that draws feeding currents towards the subumbrella.

Supplementary Movie 8

Fluid flow field and vorticity field of a suboptimal medusoid design. The movie was generated from DPIV data. In contrast to jellyfish and optimal medusoids, suboptimal medusoids with "sieve design" fail to sufficiently accelerate fluid during the power stroke, resulting in poor thrust generation. Vorticity patterns are more diffuse compared to those observed in jellyfish and optimal designs, and further flow analysis revealed that generation of feeding currents was inferior as well.

Supplementary Movie 9

Spontaneous lappet contractions of medusoid construct are unsynchronized; external field stimulation (monophasic voltage square pulse, 2.5 V/cm, 10 ms duration) synchronizes muscle activation.

Supplementary Movie 10

Finite element simulation of cardiomyocyte-powered thin film contraction, adapted from original movie courteously provided by Jongmin Shim (cf. Shim et al. 2012).

Supplementary Movie 11

Lobed medusoid design exhibits pronounced contraction but no propulsion.

Supplementary Movie 12

Tracking of angular speed of jellyfish lappets during stroke cycle. Displacement of labeled lappet tip relative to central reference pint is plotted as a function of time.

Supplementary Movie 13

Efficient propulsion: Ephyra reared at 13°C, swimming at 13°C water temperature, propels itself efficiently. The lobed geometry is suitable for propulsion due to boundary layer overlap that resists leakage through gap space and effectively extends paddle surface.

Supplementary Movie 14

Treading the water: Ephyra reared at 13°C, swimming at 21°C water temperature, fails to propel itself. The lobed geometry sieves through the fluid and is not suitable for propulsion at the lower viscosity of water at this temperature.

Bibliography

M. Abramoff, P. Magelhaes, and S. Ram. Image processing with ImageJ. *Biophotonics Int*, 11(7):36–42, 2004.

R. J. Adrian. Particle-imaging techniques for experimental fluid mechanics. *Annual Review of Fluid Mechanics*, 23(1):261–304, Jan. 1991. ISSN 0066-4189. doi: 10.1146/annurev.fl.23.010191.001401. URL http://www.annualreviews.org/doi/abs/10.1146/annurev.fl.23.010191.001401.

P. S. Agutter and J. A. Tuszynski. Analytic theories of allometric scaling. *The Journal of Experimental Biology*, 214(7):1055–1062, Apr. 2011. ISSN 0022-0949, 1477-9145. doi: 10.1242/jeb.054502. URL http://jeb.biologists.org/content/214/7/1055.

P. W. Alford, A. W. Feinberg, S. P. Sheehy, and K. K. Parker. Biohybrid thin films for measuring contractility in engineered cardiovascular muscle. *Biomaterials*, 31(13):3613–3621, May 2010. ISSN 0142-9612. doi: 10.1016/j.biomaterials.2010.01.079. PMID: 20149449 PMCID: 2838170.

P. A. V. Anderson and W. E. Schwab. The organization and structure of nerve and muscle in the jellyfish *Cyanea capillata* (coelenterata; scyphozoa). *Journal of Morphology*, 170(3):383–399, 1981. doi: 10.1002/jmor.1051700309. URL http://dx.doi.org/10.1002/jmor.1051700309.

E. Andrianantoandro, S. Basu, D. K. Karig, and R. Weiss. Synthetic biology: New

engineering rules for an emerging discipline. *Molecular systems biology*, 2:2006.0028, 2006. ISSN 1744-4292. doi: 10.1038/msb4100073. PMID: 16738572.

M. N. Arai. *A functional biology of Scyphozoa*. Springer, 1997. ISBN 9780412451102.

P. Ball. *The self-made tapestry: pattern formation in nature*. New York: Oxford University Press, July 2001. ISBN 9780198502432.

Y. Bar-Cohen. Eap as artificial muscles: Progress and challenges. *Proceedings of SPIE*, pages 10–16, 2004. doi: 10.1117/12.538698. URL http://spie.org/x648.html?product_id=538698.

Y. Bar-Cohen. Biomimetics–using nature to inspire human innovation. *Bioinspiration & Biomimetics*, 1(1):P1–P12, Mar. 2006. ISSN 1748-3190. doi: 10.1088/1748-3182/1/1/P01. URL http://www.ncbi.nlm.nih.gov/pubmed/17671297. PMID: 17671297.

I. K. Bartol, P. S. Krueger, J. T. Thompson, and W. J. Stewart. Swimming dynamics and propulsive efficiency of squids throughout ontogeny. *Integrative and Comparative Biology*, 48(6):720–733, Dec. 2008. ISSN 1540-7063, 1557-7023. doi: 10.1093/icb/icn043. URL http://icb.oxfordjournals.org/content/48/6/720.

P. V. Bayly, B. H. KenKnight, J. M. Rogers, R. E. Hillsley, R. E. Ideker, and W. M. Smith. Estimation of conduction velocity vector fields from epicardial mapping data. *IEEE Transactions on Bio-Medical Engineering*, 45(5):563–571, May 1998. ISSN 0018-9294. doi: 10.1109/10.641337. URL http://www.ncbi.nlm.nih.gov/pubmed/9581054. PMID: 9581054.

R. M. Bell, M. M. Mocanu, and D. M. Yellon. Retrograde heart perfusion: The Langendorff technique of isolated heart perfusion. *Journal of Molecular and Cellular Cardiology*, 50(6):940–950, June 2011. ISSN 0022-2828. doi: 10.1016/j.yjmcc.2011.02.018. URL http://www.sciencedirect.com/science/article/pii/S0022282811000952.

P. Bella and R. V. Kohn. Wrinkles as a relaxation of compressive stresses in an annular thin film. *arXiv preprint arXiv:1202.3160*, 2012. URL http://arxiv.org/abs/1202.3160.

J. Bilic and J. C. Izpisua Belmonte. Concise review: Induced pluripotent stem cells versus embryonic stem cells: Close enough or yet too far apart? *Stem cells (Dayton, Ohio)*, 30(1):33–41, Jan. 2012. ISSN 1549-4918. doi: 10.1002/stem.700. PMID: 22213481.

R. S. Blanquet and G. P. Riordan. An ultrastructural study of the subumbrellar musculature and desmosomal complexes of *Cassiopea xamachana* (Cnidaria: scyphozoa). *Transactions of the American Microscopical Society*, 100(2):109–119, Apr. 1981. ISSN 0003-0023. doi: 10.2307/3225794. URL http://www.jstor.org/stable/3225794.

M. Böl, S. Reese, K. K. Parker, and E. Kuhl. Computational modeling of muscular thin films for cardiac repair. *Computational Mechanics*, 43(4):535–544, Sept. 2008. ISSN 0178-7675. doi: 10.1007/s00466-008-0328-5. URL http://www.springerlink.com/content/q83035412861087q/.

M.-A. Bray, S. P. Sheehy, and K. K. Parker. Sarcomere alignment is regulated by myocyte shape. *Cell Motility and the Cytoskeleton*, 65(8):641–651, Aug. 2008. ISSN 1097-0169. doi: 10.1002/cm.20290. URL http://www.ncbi.nlm.nih.gov/pubmed/18561184. PMID: 18561184.

D. M. Bryant and K. E. Mostov. From cells to organs: Building polarized tissue. *Nature Reviews Molecular Cell Biology*, 9(11):887–901, Nov. 2008. ISSN 1471-0072, 1471-0080. doi: 10.1038/nrm2523. URL http://www.nature.com/scitable/content/from-cells-to-organs-building-polarized-tissue-14019080.

N. Bursac, K. K. Parker, S. Iravanian, and L. Tung. Cardiomyocyte cultures with controlled macroscopic anisotropy: A model for functional electrophysiological studies

of cardiac muscle. *Circulation Research*, 91(12):e45–54, Dec. 2002. ISSN 1524-4571. URL http://www.ncbi.nlm.nih.gov/pubmed/12480825. PMID: 12480825.

E. Cerda and L. Mahadevan. Confined developable elastic surfaces: Cylinders, cones and the elastica. *Proc. R. Soc. A*, 461:671–700, 2005.

D. M. Chapman. Microanatomy of the bell rim of *Aurelia aurita* (Cnidaria: scyphozoa). *Canadian Journal of Zoology*, 77(1):34–46, July 1999. ISSN 0008-4301. doi: 10.1139/z98-193. URL http://www.nrcresearchpress.com/doi/abs/10.1139/z98-193.

T.-H. Chen, C. Guo, X. Zhao, Y. Yao, K. I. Bostrom, M. N. Wong, Y. Tintut, L. L. Demer, C.-M. Ho, and A. Garfinkel. Patterns of periodic holes created by increased cell motility. *Interface Focus*, 2(4):457–464, Mar. 2012. ISSN 2042-8898, 2042-8901. doi: 10.1098/rsfs.2012.0001. URL http://rsfs.royalsocietypublishing.org/cgi/doi/10.1098/rsfs.2012.0001.

I. M. Conboy, M. J. Conboy, A. J. Wagers, E. R. Girma, I. L. Weissman, and T. A. Rando. Rejuvenation of aged progenitor cells by exposure to a young systemic environment. *Nature*, 433(7027):760–764, 2005. URL http://www.nature.com/nature/journal/v433/n7027/abs/nature03260.html.

P. A. Corning. The re-emergence of "emergence": A venerable concept in search of a theory. *Complexity*, 7(6):2002, 2002.

J. H. Costello and S. P. Colin. Flow and feeding by swimming scyphomedusae. *Marine Biology*, 124(3):399–406, Dec. 1995. ISSN 0025-3162. doi: 10.1007/BF00363913. URL http://www.springerlink.com/content/m7738777606596wu/.

J. O. Dabiri. Optimal vortex formation as a unifying principle in biological propulsion. *Annual Review of Fluid Mechanics*, 41(1):17–33, Jan. 2009. ISSN 0066-4189, 1545-4479. doi: 10.1146/annurev.fluid.010908.165232. URL http://www.annualreviews.org/doi/abs/10.1146/annurev.fluid.010908.165232.

J. O. Dabiri, S. P. Colin, J. H. Costello, and M. Gharib. Flow patterns generated by oblate medusan jellyfish: Field measurements and laboratory analyses. *The Journal of Experimental Biology*, 208(Pt 7):1257–65, Apr. 2005. ISSN 0022-0949. doi: 10.1242/jeb.01519. URL http://www.ncbi.nlm.nih.gov/pubmed/15781886. PMID: 15781886.

J. O. Dabiri, S. P. Colin, and J. H. Costello. Morphological diversity of medusan lineages constrained by animal-fluid interactions. *The Journal of Experimental Biology*, 210 (Pt 11):1868–73, June 2007. ISSN 0022-0949. doi: 10.1242/jeb.003772. URL http://www.ncbi.nlm.nih.gov/pubmed/17515413. PMID: 17515413.

T. L. Daniel. Mechanics and energetics of medusan jet propulsion. *Canadian Journal of Zoology*, 61(6):1406–1420, 1983.

T. L. Daniel. Cost of locomotion: Unsteady medusan swimming. *Journal of Experimental Biology*, 119(1):149–164, 1985. URL http://jeb.biologists.org/content/119/1/149.short.

L. P. Dasi, H. A. Simon, P. Sucosky, and A. P. Yoganathan. Fluid mechanics of artificial heart valves. *Clinical and Experimental Pharmacology & Physiology*, 36(2):225–237, Feb. 2009. ISSN 1440-1681. doi: 10.1111/j.1440-1681.2008.05099.x. URL http://www.ncbi.nlm.nih.gov/pubmed/19220329. PMID: 19220329.

M. E. Demont and J. M. Gosline. Mechanics of jet propulsion in the hydromedusan jellyfish, polyorchis pexicillatus: I. mechanical properties of the locomotor structure. *Journal of Experimental Biology*, 134(1):313–332, Jan. 1988. ISSN 0022-0949, 1477-9145. URL http://jeb.biologists.org/content/134/1/313.

T. DeWitt and S. Scheiner. *Plasticity. Functional and Conceptual Approaches.* Oxford University Press, USA, 2004.

T. Dvir, B. P. Timko, M. D. Brigham, S. R. Naik, S. S. Karajanagi, O. Levy, H. Jin, K. K. Parker, R. Langer, and D. S. Kohane. Nanowired three-dimensional cardiac patches.

Nature Nanotechnology, 6(11):720–725, 2011. ISSN 1748-3387. doi: 10.1038/nnano.2011.160. URL http://www.nature.com/nnano/journal/v6/n11/full/nnano.2011.160.html.

M. B. Elowitz, A. J. Levine, E. D. Siggia, and P. S. Swain. Stochastic gene expression in a single cell. *Science*, 297(5584):1183–1186, Aug. 2002. ISSN 0036-8075, 1095-9203. doi: 10.1126/science.1070919. URL http://www.sciencemag.org/content/297/5584/1183.

A. J. Engler, S. Sen, H. L. Sweeney, and D. E. Discher. Matrix elasticity directs stem cell lineage specification. *Cell*, 126(4):677–689, Aug. 2006. ISSN 0092-8674. doi: 10.1016/j.cell.2006.06.044. URL http://www.ncbi.nlm.nih.gov/pubmed/16923388. PMID: 16923388.

K. M. Esvelt, J. C. Carlson, and D. R. Liu. A system for the continuous directed evolution of biomolecules. *Nature*, 472(7344):499–503, Apr. 2011. ISSN 0028-0836. doi: 10.1038/nature09929. URL http://www.nature.com/nature/journal/v472/n7344/full/nature09929.html.

V. V. Fedorov, I. T. Lozinsky, E. A. Sosunov, E. P. Anyukhovsky, M. R. Rosen, C. W. Balke, and I. R. Efimov. Application of blebbistatin as an excitation-contraction uncoupler for electrophysiologic study of rat and rabbit hearts. *Heart Rhythm*, 4 (5):619–626, May 2007. ISSN 1547-5271. doi: 16/j.hrthm.2006.12.047. URL http://www.sciencedirect.com/science/article/pii/S1547527106023629.

A. Feinberg, P. Alford, H. Jin, C. Ripplinger, A. Werdich, S. Sheehy, A. Grosberg, and K. Parker. Controlling the contractile strength of engineered cardiac muscle by hierarchal tissue architecture. *Biomaterials*, 33(23):5732–41, 2012.

A. W. Feinberg, A. Feigel, S. S. Shevkoplyas, S. Sheehy, G. M. Whitesides, and K. K. Parker. Muscular thin films for building actuators and powering devices. *Science (New*

York, N.Y.), 317(5843):1366–1370, Sept. 2007. ISSN 1095-9203. doi: 10.1126/science.1146885. URL http://www.ncbi.nlm.nih.gov/pubmed/17823347. PMID: 17823347.

K. E. Feitl, A. F. Millett, S. P. Colin, J. O. Dabiri, and J. H. Costello. Functional morphology and fluid interactions during early development of the scyphomedusa aurelia aurita. *The Biological Bulletin*, 217(3):283–291, Dec. 2009. ISSN 1939-8697. URL http://www.ncbi.nlm.nih.gov/pubmed/20040752. PMID: 20040752.

P. Fu. A perspective of synthetic biology: Assembling building blocks for novel functions. *Biotechnology Journal*, 1(6):690–699, June 2006. ISSN 1860-7314. doi: 10.1002/biot.200600019. URL http://www.ncbi.nlm.nih.gov/pubmed/16892318. PMID: 16892318.

C. Gambini, B. Abou, A. Ponton, and A. Cornelissen. Micro- and macrorheology of jellyfish extracellular matrix. *Biophys J.*, 102(1):1–9, 2012.

R. Gauvin, R. Parenteau-Bareil, M. R. Dokmeci, W. D. Merryman, and A. Khademhosseini. Hydrogels and microtechnologies for engineering the cellular microenvironment. *Wiley interdisciplinary reviews. Nanomedicine and nanobiotechnology*, 4(3):235–246, June 2012. ISSN 1939-0041. doi: 10.1002/wnan.171. URL http://www.ncbi.nlm.nih.gov/pubmed/22144036. PMID: 22144036.

M. Gharib, E. Rambod, A. Kheradvar, D. J. Sahn, and J. O. Dabiri. Optimal vortex formation as an index of cardiac health. *Proceedings of the National Academy of Sciences*, 103(16):6305–6308, 2006. URL http://www.pnas.org/content/103/16/6305.short.

W. B. Gladfelter. Structure and function of the locomotory system of the scyphomedusa cyanea capillata. *Marine Biology*, 14(2):150–160, May 1972. ISSN 0025-3162. doi: 10.1007/BF00373214. URL http://www.springerlink.com/content/n42204j872044514/.

W. G. Gladfelter. A comparative analysis of the locomotory systems of medusoid cnidaria. *Helgoländer Wissenschaftliche Meeresuntersuchungen*, 25(2-3):228–

272, Sept. 1973. ISSN 0017-9957. doi: 10.1007/BF01611199. URL http://www.springerlink.com/content/r7q364k887397tr1/.

A. M. Gordon, A. F. Huxley, and F. J. Julian. The variation in isometric tension with sarcomere length in vertebrate muscle fibres. *The Journal of Physiology*, 184(1):170–192, May 1966. ISSN 0022-3751. URL http://www.ncbi.nlm.nih.gov/pmc/articles/PMC1357553/. PMID: 5921536 PMCID: PMC1357553.

J. Gosline and M. E. DeMont. Jet-propelled swimming in squids. *Scientific American*, 252(1)::96–103, 1985.

A. Grosberg, P.-L. Kuo, C.-L. Guo, N. A. Geisse, M.-A. Bray, W. J. Adams, S. P. Sheehy, and K. K. Parker. Self-organization of muscle cell structure and function. *PLoS computational biology*, 7(2):e1001088, Feb. 2011. ISSN 1553-7358. doi: 10.1371/journal.pcbi.1001088. PMID: 21390276.

D. Halliday, R. Resnick, and J. Walker. *Fundamentals of Physics*. New York: John Wiley and Sons, Mar. 2010. ISBN 9780470469118.

I. W. Hamley. Liquid crystals. In *Introduction to Soft Matter: Synthetic and Biological Self-Assembling Materials*, pages 221–273. John Wiley & Sons, Chichester, England, 7 edition, 2007. URL http://onlinelibrary.wiley.com/doi/10.1002/9780470517338.ch5/summary.

I. Haruto and O. Chiharu. Survivorship of *Aurelia aurita* throughout their life cycle in tokyo bay. *Bulletin of Plankton Society of Japan*, 52(2):77–81, 2005. ISSN 0387-8961. URL http://sciencelinks.jp/j-east/article/200601/000020060105A0829127.php.

W. Harvey and C. D. Leake. *Exercitatio anatomica de motu cordis et sanguinis in animalibus*. Springfield, Ill. : Thomas, 1928. URL http://archive.org/details/exercitatioanato00harv. Reprinted from first edition, 1628, Frankfurt, Germany.

R. T. Hayward. *Modeling experiments on pacemaker interactions in scyphomedusae*. PhD thesis, The University of North Carolina Wilmington (UNCW), 2007. URL http://libres.uncg.edu/ir/uncw/listing.aspx?id=1787.

S. A. H. Hoffmeister-Ullerich. Hydra – ancient model with modern outfit. *Cellular and Molecular Life Sciences: CMLS*, 64(23):3012–3016, Dec. 2007. ISSN 1420-682X. doi: 10.1007/s00018-007-7204-x. URL http://www.ncbi.nlm.nih.gov/pubmed/17891334. PMID: 17891334.

S. J. Hollister. Porous scaffold design for tissue engineering. *Nature Materials*, 4(7): 518–524, July 2005. ISSN 1476-1122. doi: 10.1038/nmat1421. URL http://www.ncbi.nlm.nih.gov/pubmed/16003400. PMID: 16003400.

D. Holmes, M. Ursiny, and A. Crosby. Crumpled surface structures. *Soft Matter*, 4: 82–85, 2008.

C. Holubarsch, J. Lüdemann, S. Wiessner, T. Ruf, H. Schulte-Baukloh, S. Schmidt-Schweda, B. Pieske, H. Posival, and H. Just. Shortening versus isometric contractions in isolated human failing and non-failing left ventricular myocardium: Dependency of external work and force on muscle length, heart rate and inotropic stimulation. *Cardiovascular Research*, 37(1):46–57, Jan. 1998. ISSN 0008-6363,. doi: 10.1016/S0008-6363(97)00215-0. URL http://cardiovascres.oxfordjournals.org/content/37/1/46.

G. A. Horridge. The nerves and muscles of medusae. *Journal of Experimental Biology*, 33(2):366–383, 1956. URL http://jeb.biologists.org/content/33/2/366.short.

A. H. Huang, M. J. Farrell, and R. L. Mauck. Mechanics and mechanobiology of mesenchymal stem cell-based engineered cartilage. *Journal of biomechanics*, 43(1):128, Jan. 2010. ISSN 0021-9290. doi: 10.1016/j.jbiomech.2009.09.018. PMID: 19828149 PMCID: 2813425.

J. Hure, B. Roman, and J. Bico. Stamping and wrinkling of elastic plates. *Physical Review Letters*, 109(5):54302, 2012. URL http://link.aps.org/doi/10.1103/PhysRevLett.109.054302.

D. W. Hutmacher. Biomaterials offer cancer research the third dimension. *Nature Materials*, 9(2):90–93, 2010. ISSN 1476-1122. doi: 10.1038/nmat2619. URL http://www.nature.com/nmat/journal/v9/n2/abs/nmat2619.html.

B. Jewell and R. Porter. Introduction: The changing face of the length-tension relation. In D. Fitzsimons, editor, *Ciba Foundation Symposium 24 - Physiological Basis of Starling's Law of the Heart*, pages 6–12. John Wiley & Sons, Ltd, 2008.

C. Jopling, S. Boue, and J. C. I. Belmonte. Dedifferentiation, transdifferentiation and reprogramming: Three routes to regeneration. *Nature Reviews Molecular Cell Biology*, 12(2):79–89, Feb. 2011. ISSN 1471-0072. doi: 10.1038/nrm3043. URL http://www.nature.com.clsproxy.library.caltech.edu/nrm/journal/v12/n2/abs/nrm3043.html.

R. S. Kane, S. Takayama, E. Ostuni, D. E. Ingber, and G. M. Whitesides. Patterning proteins and cells using soft lithography. *Biomaterials*, 20(23-24):2363–2376, Dec. 1999. ISSN 0142-9612. PMID: 10614942.

Y. N. Kaznessis. Models for synthetic biology. *BMC Systems Biology*, 1:47, 2007. ISSN 1752-0509. doi: 10.1186/1752-0509-1-47. URL http://www.ncbi.nlm.nih.gov/pubmed/17986347. PMID: 17986347.

A. J. Keung, K. E. Healy, S. Kumar, and D. V. Schaffer. Biophysics and dynamics of natural and engineered stem cell microenvironments. *Wiley Interdisciplinary Reviews: Systems Biology and Medicine*, 2(1):49–64, 2010. ISSN 1939-005X. doi: 10.1002/wsbm.46. URL http://onlinelibrary.wiley.com/doi/10.1002/wsbm.46/abstract.

H. King, R. D. Schroll, B. Davidovitch, and N. Menon. Elastic sheet on a liquid drop reveals wrinkling and crumpling as distinct symmetry-breaking instabilities.

Proceedings of the National Academy of Sciences, 109(25):9716–"9720, 2012. URL http://www.pnas.org/content/109/25/9716.short.

M. Kleiber. Body size and metabolism. *Hilgardia*, 6:315–351, 1932.

M. A. R. Koehl. Biomechanics of microscopic appendages: Functional shifts caused by changes in speed. *Journal of Biomechanics*, 37(6):789–95, June 2004. ISSN 0021-9290. doi: 10.1016/j.jbiomech.2003.06.001. URL http://www.ncbi.nlm.nih.gov/pubmed/15111066. PMID: 15111066.

M. A. R. Koehl, J. R. Koseff, J. P. Crimaldi, M. G. McCay, T. Cooper, M. B. Wiley, and P. A. Moore. Lobster sniffing: Antennule design and hydrodynamic filtering of information in an odor plume. *Science (New York, N.Y.)*, 294(5548):1948–1951, Nov. 2001. ISSN 0036-8075. doi: 10.1126/science.1063724. URL http://www.ncbi.nlm.nih.gov/pubmed/11729325. PMID: 11729325.

M. LaBarbera. Feeding currents and particle capture mechanisms in suspension feeding animals. *American Zoologist*, 24(1):71–84, Jan. 1984. ISSN 1540-7063, 1557-7023. doi: 10.1093/icb/24.1.71. URL http://icb.oxfordjournals.org/content/24/1/71.

M. LaBarbera. Principles of design of fluid transport systems in zoology. *Science (New York, N.Y.)*, 249(4972):992–1000, Aug. 1990. ISSN 0036-8075. PMID: 2396104.

R. Langer and J. P. Vacanti. Tissue engineering. *Science (New York, N.Y.)*, 260(5110):920–926, May 1993. ISSN 0036-8075. PMID: 8493529.

T. M. Lavertu, L. Mydlarski, and S. J. Gaskin. Differential diffusion of high-Schmidt-number passive scalars in a turbulent jet. *Journal of Fluid Mechanics*, 612(-1):439–475, 2008. doi: 10.1017/S0022112008003224. URL http://journals.cambridge.org/action/displayAbstract?fromPage=online&aid=2242924.

M. Li, G.-H. Liu, and J. C. Izpisua Belmonte. Navigating the epigenetic landscape of pluripotent stem cells. *Nature reviews. Molecular cell biology*, 13(8):524–535, Aug. 2012. ISSN 1471-0080. doi: 10.1038/nrm3393. PMID: 22820889.

C. H. Lucas. Reproduction and life history strategies of the common jellyfish, *Aurelia aurita*, in relation to its ambient environment. *Hydrobiologia*, 451(1):229–246, May 2001. doi: 10.1023/A:1011836326717. URL http://dx.doi.org/10.1023/A:1011836326717.

A. J. Lusis and J. N. Weiss. Cardiovascular networks systems-based approaches to cardiovascular disease. *Circulation*, 121(1):157–170, Jan. 2010. ISSN 0009-7322, 1524-4539. doi: 10.1161/CIRCULATIONAHA.108.847699. URL http://circ.ahajournals.org/content/121/1/157.

M. P. Lutolf and J. A. Hubbell. Synthetic biomaterials as instructive extracellular microenvironments for morphogenesis in tissue engineering. *Nature Biotechnology*, 23 (1):47–55, Jan. 2005. ISSN 1087-0156. doi: 10.1038/nbt1055. URL http://www.nature.com/doifinder/10.1038/nbt1055.

G. O. Mackie and L. M. Passano. Epithelial conduction in hydromedusae. *The Journal of General Physiology*, 52(3):600–621, Sept. 1968. ISSN 0022-1295. PMID: 19873635 PMCID: 2225826.

M. Marder, R. Deegan, and E. Sharon. Crumpling, buckling, and cracking: Elasticity of thin sheets. *Physics Today*, 60(2):33–38, 2007. URL http://apx.lib.nthu.edu.tw:8611/login.aspx?direct=true&db=aph&AN=23954832&site=ehost-live.

J. H. Masliyah and N. Epstein. Steady symmetric flow past elliptical cylinders. *Industrial & Engineering Chemistry Fundamentals*, 10(2):293–299, May 1971. doi: 10.1021/i160038a017. URL http://dx.doi.org/10.1021/i160038a017.

M. L. McCain, H. Lee, Y. Aratyn-Schaus, A. G. Kleber, and K. K. Parker. Cooperative coupling of cell-matrix and cell-cell adhesions in cardiac muscle. *Proceedings of the*

National Academy of Sciences, 109(25):9881–9886, June 2012. ISSN 1091-6490. doi: 10.1073/pnas.1203007109. PMID: 22675119.

W. M. Megill. *The biomechanics of jellyfish swimming*. PhD thesis, The University of British Columbia, 2002. URL http://cerf.bc.ca/megill/jfish/thesis/thesis.pdf.

W. M. Megill, J. M. Gosline, and R. W. Blake. The modulus of elasticity of fibrillin-containing elastic fibres in the mesoglea of the hydromedusa *Polyorchis penicillatus*. *Journal of Experimental Biology*, 208(20):3819–3834, Oct. 2005. ISSN 0022-0949, 1477-9145. doi: 10.1242/jeb.01765. URL http://jeb.biologists.org/content/208/20/3819.

S. Mitragotri and J. Lahann. Physical approaches to biomaterial design. *Nature Materials*, 8(1):15–23, Jan. 2009. ISSN 1476-1122. doi: 10.1038/nmat2344. URL http://dx.doi.org/10.1038/nmat2344.

C. D. Murray. The physiological principle of minimum work: I. the vascular system and the cost of blood volume. *Proceedings of the National Academy of Sciences of the United States of America*, 12(3):207–214, Mar. 1926. ISSN 0027-8424. PMID: 16576980.

T. Nakagaki, H. Yamada, A. Toth, et al. Maze-solving by an amoeboid organism. *Nature*, 407(6803):470, 2000.

J. C. Nawroth, K. E. Feitl, S. P. Colin, J. H. Costello, and J. O. Dabiri. Phenotypic plasticity in juvenile jellyfish medusae facilitates effective animal-fluid interaction. *Biology Letters*, 6(3):389–393, Mar. 2010. ISSN 1744-9561, 1744-957X. doi: 10.1098/rsbl.2010.0068. URL http://rsbl.royalsocietypublishing.org/cgi/doi/10.1098/rsbl.2010.0068.

J. C. Nawroth, H. Lee, A. W. Feinberg, C. M. Ripplinger, M. L. McCain, A. Grosberg, J. O. Dabiri, and K. K. Parker. A tissue-engineered jellyfish with biomimetic propul-

sion. *Nature Biotechnology*, 30(8):792–797, July 2012. ISSN 1087-0156, 1546-1696. doi: 10.1038/nbt.2269. URL http://www.nature.com/doifinder/10.1038/nbt.2269.

J. S. Olshansky, B. A. Carnes, and R. N. Butler. If humans were built to last. *Scientific American*, 284(3):50–55, Mar. 2001. ISSN 0036-8733. URL http://www.ncbi.nlm.nih.gov/pubmed/11234506. PMID: 11234506.

K. K. Parker and D. E. Ingber. Extracellular matrix, mechanotransduction and structural hierarchies in heart tissue engineering. *Philosophical Transactions of the Royal Society B: Biological Sciences*, 362(1484):1267–1279, Aug. 2007. ISSN 0962-8436, 1471-2970. doi: 10.1098/rstb.2007.2114. URL http://rstb.royalsocietypublishing.org/cgi/doi/10.1098/rstb.2007.2114.

L. M. Passano. Pacemakers and activity patterns the medusae: Homage to Romanes. *American Zoologist*, 5(3):465 –481, 1965. doi: 10.1093/icb/5.3.465. URL http://icb.oxfordjournals.org/content/5/3/465.abstract.

M. R. Patterson. A mass transfer explanation of metabolic scaling relations in some aquatic invertebrates and algae. *Science*, 255(5050):1421–1423, Mar. 1992. ISSN 0036-8075. doi: 10.1126/science.255.5050.1421. URL http://www.ncbi.nlm.nih.gov/pubmed/17801232. PMID: 17801232.

J. E. Phillips, K. L. Burns, J. M. L. Doux, R. E. Guldberg, and A. J. Garcia. Engineering graded tissue interfaces. *Proceedings of the National Academy of Sciences*, 105(34):12170–12175, Aug. 2008. ISSN 0027-8424, 1091-6490. doi: 10.1073/pnas.0801988105. URL http://www.pnas.org/content/105/34/12170.

E. S. Place, N. D. Evans, and M. M. Stevens. Complexity in biomaterials for tissue engineering. *Nature Materials*, 8(6):457–470, June 2009. ISSN 1476-1122. doi: 10.1038/nmat2441. URL http://dx.doi.org/10.1038/nmat2441.

H. P. Riessen and J. B. Trevett-Smith. Turning inducible defenses on and off: Adaptive responses of *Daphnia* to a gape-limited predator. *Ecology*, 90(12):3455–3469, Dec. 2009. ISSN 0012-9658. PMID: 20120813.

G. J. Romanes. *Jelly-fish, star-fish and sea-urchins; being a research on primitive nervous systems*. New York: D. Appleton and company, 1898. URL http://books.google.com/books?id=UkvWZttD3zQC&oe=UTF-8.

S. A. Ruiz and C. S. Chen. Emergence of patterned stem cell differentiation within multicellular structures. *Stem Cells*, 26(11):2921–2927, Nov. 2008. ISSN 10665099, 15494918. doi: 10.1634/stemcells.2008-0432. URL http://doi.wiley.com/10.1634/stemcells.2008-0432.

M. S. Sacks and A. P. Yoganathan. Heart valve function: A biomechanical perspective. *Philosophical Transactions of the Royal Society of London. Series B, Biological Sciences*, 362(1484):1369–1391, Aug. 2007. ISSN 0962-8436. doi: 10.1098/rstb.2007.2122. URL http://www.ncbi.nlm.nih.gov/pubmed/17588873. PMID: 17588873.

V. K. Satheesh, R. P. Chhabra, and V. Eswaran. Steady incompressible fluid flow over a bundle of cylinders at moderate Reynolds numbers. *The Canadian Journal of Chemical Engineering*, 77(5):978–987, Oct. 1999. ISSN 1939-019X. doi: 10.1002/cjce.5450770527. URL http://onlinelibrary.wiley.com/doi/10.1002/cjce.5450770527/abstract.

R. A. Satterlie. Neuronal control of swimming in jellyfish: A comparative story. *Canadian Journal of Zoology*, 80(10):1654–1669, 2002.

R. A. Satterlie. Control of swimming in the hydrozoan jellyfish *Aequorea victoria*: Subumbrellar organization and local inhibition. *J Exp Biol*, 211(21):3467–3477, Nov. 2008. doi: 10.1242/jeb.018952. URL http://jeb.biologists.org/cgi/content/abstract/211/21/3467.

C. Schlichting and M. Pigliucci. *Phenotypic evolution: a reaction norm perspective*. Sinauer Associates, 1998.

H. Schlichting and K. Gersten. *Boundary-layer theory*. New York: Springer, 8th edition, 2000.

A. Seidi, M. Ramalingam, I. Elloumi-Hannachi, S. Ostrovidov, and A. Khademhosseini. Gradient biomaterials for soft-to-hard interface tissue engineering. *Acta biomaterialia*, 7(4):1441–1451, Apr. 2011. ISSN 1878-7568. doi: 10.1016/j.actbio.2011.01.011. URL http://www.ncbi.nlm.nih.gov/pubmed/21232635. PMID: 21232635.

J. Shim, A. Grosberg, J. Nawroth, K. K. Parker, and K. Bertoldi. Modeling of cardiac muscular thin films: Pre-stretch, passive and active behavior. *Journal of Biomechanics*, 45:832–841, 2012.

M. Skrzypiec-Spring, B. Grotthus, A. Szelag, and R. Schulz. Isolated heart perfusion according to Langendorff viable in the new millennium. *Journal of Pharmacological and Toxicological Methods*, 55(2):113–126, Mar. 2007. ISSN 1056-8719. doi: 10.1016/j.vascn.2006.05.006. URL http://www.sciencedirect.com/science/article/pii/S1056871906000669.

P. R. H. Steinmetz, J. E. M. Kraus, C. Larroux, J. U. Hammel, A. Amon-Hassenzahl, E. Houliston, G. Woerheide, M. Nickel, B. M. Degnan, and U. Technau. Independent evolution of striated muscles in cnidarians and bilaterians. *Nature*, 487(7406):231–234, July 2012. ISSN 1476-4687. doi: 10.1038/nature11180. PMID: 22763458.

B. Suki and J. H. T. Bates. Lung tissue mechanics as an emergent phenomenon. *Journal of Applied Physiology*, 110(4):1111–1118, Apr. 2011. ISSN 8750-7587, 1522-1601. doi: 10.1152/japplphysiol.01244.2010. URL http://jap.physiology.org/content/110/4/1111.

K. Y. Tsang, M. C. H. Cheung, D. Chan, and K. S. E. Cheah. The developmental roles of the extracellular matrix: Beyond structure to regulation. *Cell and Tissue Research*, 339(1):93–110, Nov. 2009. ISSN 0302-766X, 1432-0878. doi: 10.1007/s00441-009-0893-8. URL http://www.springerlink.com/index/10.1007/s00441-009-0893-8.

A. Umeno and S. Ueno. Quantitative analysis of adherent cell orientation influenced by strong magnetic fields. *IEEE Transactions on Nanobioscience*, 2(1):26–28, Mar. 2003. ISSN 1536-1241. URL http://www.ncbi.nlm.nih.gov/pubmed/15382419. PMID: 15382419.

S. A. Villeda, J. Luo, K. I. Mosher, B. Zou, M. Britschgi, G. Bieri, T. M. Stan, N. Fainberg, Z. Ding, A. Eggel, K. M. Lucin, E. Czirr, J.-S. Park, S. Couillard-Després, L. Aigner, G. Li, E. R. Peskind, J. A. Kaye, J. F. Quinn, D. R. Galasko, X. S. Xie, T. A. Rando, and T. Wyss-Coray. The ageing systemic milieu negatively regulates neurogenesis and cognitive function. *Nature*, 477(7362):90–94, Aug. 2011. ISSN 0028-0836, 1476-4687. doi: 10.1038/nature10357. URL http://www.nature.com/doifinder/10.1038/nature10357.

S. Vogel. *Life in moving fluids: The physical biology of flow.* Princeton, New York: Princeton University Press, Apr. 1996. ISBN 9780691026169.

K. von der Mark, J. Park, S. Bauer, and P. Schmuki. Nanoscale engineering of biomimetic surfaces: Cues from the extracellular matrix. *Cell and Tissue Research*, 339(1):131–153, Jan. 2010. ISSN 1432-0878. doi: 10.1007/s00441-009-0896-5. URL http://www.ncbi.nlm.nih.gov/pubmed/19898872. PMID: 19898872.

J. C. Weaver, G. W. Milliron, A. Miserez, K. Evans-Lutterodt, S. Herrera, I. Gallana, W. J. Mershon, B. Swanson, P. Zavattieri, E. DiMasi, and D. Kisailus. The stomatopod dactyl club: A formidable damage-tolerant biological hammer. *Science*,

336(6086):1275–1280, June 2012. ISSN 0036-8075, 1095-9203. doi: 10.1126/science.1218764. URL http://www.sciencemag.org/content/336/6086/1275.

E. R. Weibel, C. R. Taylor, and L. Bolis. *Principles of Animal Design: The Optimization and Symmorphosis Debate*. Cambridge University Press, Feb. 1998. ISBN 9780521586672.

C. L. Widmer. *How to Keep Jellyfish in Aquariums: An Introductory Guide for Maintaining Healthy Jellies*. Wheatmark, Aug. 2008. ISBN 160494126X.

S. Wiechert, A. El-Armouche, T. Rau, W.-H. Zimmermann, and T. Eschenhagen. 24-h Langendorff-perfused neonatal rat heart used to study the impact of adenoviral gene transfer. *American Journal of Physiology - Heart and Circulatory Physiology*, 285(2): H907–H914, Aug. 2003. ISSN 0363-6135, 1522-1539. doi: 10.1152/ajpheart.00856.2002. URL http://ajpheart.physiology.org/content/285/2/H907.

C. Willert and M. Gharib. Digital particle image velocimetry. *Experiments in Fluids*, 10(4), Jan. 1991. ISSN 0723-4864. doi: 10.1007/BF00190388. URL http://www.springerlink.com/content/k26hx2p53nr16411/.

T. Wyka, P. Robakowski, and R. Zytkowiak. Acclimation of leaves to contrasting irradiance in juvenile trees differing in shade tolerance. *Tree physiology*, 27(9):1293–1306, Sept. 2007. ISSN 0829-318X. PMID: 17545129.

S. Yamanaka. Induced pluripotent stem cells: Past, present, and future. *Cell Stem Cell*, 10(6):678–684, June 2012. ISSN 1934-5909. doi: 10.1016/j.stem.2012.05.005. URL http://www.cell.com/cell-stem-cell/abstract/S1934-5909(12)00237-8.

J. Yen. Life in transition: Balancing inertial and viscous forces by planktonic copepods. *The Biological Bulletin*, 198(2):213–224, Apr. 2000. ISSN 0006-3185. URL http://www.ncbi.nlm.nih.gov/pubmed/10786942. PMID: 10786942.

Z. Zhang, A. Tendulkar, K. Sun, D. A. Saloner, A. W. Wallace, L. Ge, J. M. Guccione, and M. B. Ratcliffe. Comparison of the Young-Laplace law and finite element based calculation of ventricular wall stress: Implications for postinfarct and surgical ventricular remodeling. *The Annals of Thoracic Surgery*, 91(1):150–156, Jan. 2011. ISSN 00034975. doi: 10.1016/j.athoracsur.2010.06.132. URL http://ukpmc.ac.uk/articles/PMC3058250.

Y. Zhu, S. Wan, and R.-y. Zhan. Inducible pluripotent stem cells for the treatment of ischemic stroke: Current status and problems. *Reviews in the neurosciences*, 23(4): 393–402, 2012. ISSN 0334-1763. doi: 10.1515/revneuro-2012-0042. PMID: 23089605.